Dissertation
submitted to the
Combined Faculty of Mathematics, Engineering and Natural Sciences
of Heidelberg University, Germany
for the degree of
Doctor of Natural Sciences

Put forward by
Mai Phuong Tran

Born in: Hanoi, Vietnam
Oral examination: 14.10.2025

Genetic Encoding of Function: From DNA Segregation to Synthetic Cytoskeletons

Thesis supervisor:	Prof. Dr. Kerstin Göpfrich
Referees:	Prof. Dr. Kerstin Göpfrich
	Asst. Prof. Dr. Ebbe Sloth Andersen

Abstract

Synthetic cells provide a powerful platform to explore the origins and principles of life, and hold promise for transformative applications in biotechnology. Among life's features, evolvability is the central landmark to be engineered for life to emerge from non-living matter. However, there is currently no general strategy for the programmable segregation of genetic material, and structural components like cytoskeletons are rarely expressed *in situ*, limiting their evolvability.

In the first part, I develop a DNA-based module for programmable spatial segregation of information. Using DNA motifs that undergo liquid-liquid phase separation, DNA droplets can be induced to split via enzymatic or light triggers. When confined in synthetic compartments, their segregation kinetics and spatial behavior become sequence- and environment-dependent. A lattice-based theoretical model reproduces key features of the dynamics and helps explain how confinement influences segregation.

In the second part, I demonstrate the *in situ* expression of RNA origami cytoskeletons inside lipid vesicles. These co-transcriptionally folded structures self-assemble into nanotubes that bind and deform membranes. Sequence mutations modulate stiffness and morphology of the nanotubes, as shown experimentally and supported by coarse-grained molecular dynamics simulations that link sequence-level changes to mechanical responses.

By implementing nucleic acid nanostructures which give rise to microscale phenotypes, these systems create minimal genotype–phenotype couplings. This enables genetically encoded behaviors that are more readily selectable and thus more compatible with evolution.

Zusammenfassung

Synthetische Zellen können zur Erforschung der Ursprünge und Prinzipien des Lebens beitragen. Gleichzeitig bergen sie großes Potenzial für transformative Anwendungen in der Biotechnologie. Unter den Eigenschaften des Lebens ist Evolution das zentrale Merkmal, das realisiert werden muss, damit Leben aus unbelebter Materie entstehen kann. Derzeit gibt es jedoch keine allgemeine Strategie für die Teilung des genetischen Materials. Strukturelle Komponenten wie das Zytoskelett werden nur selten *in situ* exprimiert, was die Fähigkeit von synthetischen Zellen zur Evolution einschränkt.

Im ersten Teil dieser Doktorarbeit entwickle ich ein DNA-basiertes Modul zur programmierbaren Segregation von genetischer Information. Mithilfe von DNA-Motiven, die einer Flüssig-Flüssig-Phasentrennung unterliegen, können DNA-Tröpfchen durch enzymatische oder licht-induzierte Auslöser zur Teilung gebracht werden. In synthetischen Kompartimenten werden die Segregationskinetik und das räumliches Verhalten der DNA-Tröpfchen sequenz- und umweltabhängig beschrieben. Ein gitterbasiertes theoretisches Modell reproduziert die wichtigsten Merkmale der Dynamik und hilft zu erklären, wie die Begrenzung die Segregation beeinflusst.

Im zweiten Teil zeige ich die *in situ* Expression von RNA-Origami-Zytoskeletten in Lipidvesikeln. Diese co-transkriptionell gefalteten Strukturen formen Nanoröhren durch Selbstorganisation, welche Membranen binden und verformen können. Sequenzmutationen modulieren die Steifigkeit und Morphologie der Nanoröhren, wie experimentell gezeigt wird. Grobkörnige molekulardynamische Simulationen, die Sequenzänderungen mit mechanischen Reaktionen verknüpfen, unterstützen die experimentellen Daten.

Durch die Implementierung von Nukleinsäure-Nanostrukturen, die mikroskalige Phänotypen hervorbringen, schaffen diese Systeme minimale Genotyp-Phänotyp-Kopplungen. Dies ermöglicht genetisch kodierte Verhaltensweisen, die leichter selektierbar und somit besser mit der Evolution vereinbar sind.

Dedication

To all the giants whose shoulders I stand on,
and to those whose kindness, generosity and support,
in every form, made this possible.

All jenen Giganten, auf deren Schultern ich stehe,
und denen, deren Freundlichkeit, Großzügigkeit und Unterstützung -
in jeder Form – dies möglich gemacht haben.

“It’s hell writing and it’s hell not writing. The only tolerable state is having just written.”

Robert Hass

Contents

Thesis Outline 1

1 Introduction 3
- 1.1 Bottom-up construction of life . . . 3
  - 1.1.1 Why synthesize life? . . . 3
  - 1.1.2 Building evolvability into synthetic systems . . . 5
- 1.2 Genetic encoding of functions in bottom-up synthetic cells . . . 7
  - 1.2.1 Molecular substrates for evolution . . . 7
  - 1.2.2 Towards a minimal system for evolvability . . . 9
- 1.3 Bottom-up functional nucleic acid nanostructures . . . 10
  - 1.3.1 DNA and RNA folding . . . 10
  - 1.3.2 Nucleic acids in bottom-up synthetic biology . . . 14
  - 1.3.3 DNA and RNA hardware for synthetic cells . . . 15
- 1.4 Compartments for synthetic cells . . . 21
- 1.5 Research gaps and thesis roadmap . . . 26

2 Background 29
- 2.1 Confocal fluorescence microscopy . . . 29
- 2.2 Atomic force microscopy of nucleic acid origami . . . 32
- 2.3 Persistence length analysis . . . 33

3 Materials and Methods 35
- 3.1 Materials . . . 35
- 3.2 Sequences . . . 36
  - 3.2.1 DNA droplet sequences . . . 36
  - 3.2.2 DNA templates for RNA origami . . . 37
  - 3.2.3 RNA origami blueprints . . . 38
- 3.3 Methods . . . 39
  - 3.3.1 DNA and RNA design and preparation . . . 39
  - 3.3.2 Confocal microscopy . . . 41
  - 3.3.3 Atomic force microscopy . . . 42
  - 3.3.4 Encapsulation methods . . . 43
  - 3.3.5 Segregation of DNA droplet . . . 45
  - 3.3.6 Expression of RNA origami in GUVs . . . 45
  - 3.3.7 Simulation methods . . . 46
  - 3.3.8 Analysis . . . 48

3.3.9 Code availability 51
3.3.10 Statistics and Reproducibility 51

4 DNA Segregation Modules 53
4.1 DNA segregation strategy 54
4.2 DNA segregation in cell-sized confinement 59
4.3 Control of DNA segregation kinetics 63
4.4 Towards a DNA segregation module for a bottom-up assembled synthetic cell 68
4.5 Discussion 74

5 Genetic encoding and expression of RNA origami cytoskeletons in synthetic cells 75
5.1 Expression of RNA origami within GUVs 77
5.2 Co-transcriptional folding of RNA origami nanotubes 83
5.3 Persistence length analysis of RNA origami nanotubes 94
5.4 Formation of RNA origami rings 97
5.5 Expression of RNA origami cytoskeletons in synthetic cells 100
5.6 Discussion 109
5.7 Integration of nucleic acid droplets to a synthetic cytoskeleton 109

6 Conclusion and Outlook 112

Appendices 115

Abbreviations 116

A List of Publications 117

B Permissions 120

Bibliography 121

Acknowledgment 138

Thesis Outline

This PhD thesis is structured to guide the reader through the conceptual motivation, experimental realization, and the development of genetically encoded nucleic acid nanostructures with functions for the synthetic cells. The central goal is to explore how DNA and RNA nanostructures—reconstituted inside of lipid vesicles—can ultimately lead to evolvable systems. The thesis is organized into six chapters: an introduction, a background chapter, a materials and methods section, two experimental chapters, and a final conclusion and outlook. The experimental chapters present results together with an integrated discussion.

Chapter 1: Introduction.
This chapter outlines the motivations for constructing life from the bottom up, emphasizing evolution as the hallmark to recreate in order for other hallmarks of life to emerge spontaneously. It presents the concept of genetic encoding as a minimal and generalizable strategy for evolvability in synthetic cells. After reviewing the role of DNA and RNA nanotechnology in this context, the chapter identifies two key research gaps: (i) the absence of a controlled and heritable DNA segregation mechanism, and (ii) the lack of genetically expressed structural components, such as cytoskeletons, within synthetic compartments. These gaps define the two main research aims of the thesis.

Chapter 2: Background.
This chapter provides the foundational concepts underlying the experimental techniques used in this thesis.

Chapter 3: Materials and Methods.
This chapter provides detailed experimental protocols, design strategies, and computational models used throughout the thesis.

Chapter 4: A DNA Segregation Module for Synthetic Cells.
The first experimental chapter addresses the challenge of information partitioning during cell division. It presents a genetically encodable DNA droplet system capable of undergoing segregation via enzymatic and photo-triggered cleavage. The system is characterized in both bulk and confinement, and the effects of environmental parameters such as ionic strength and temperature are characterized. The work concludes with successful reconstitution in giant unilamellar lipid vesicles (GUVs), demonstrating a compartmentalized DNA segregation module as a step toward reliable inheritance.

Chapter 5: Genetic Encoding and Expression of RNA Origami Cytoskeletons.
This chapter focuses on genetically encoded architectural structures within synthetic cells. RNA origami tiles are designed to co-transcriptionally fold into cytoskeletal nanotubes inside GUVs, using only DNA templates and RNA polymerase. The system is chemically fuelled by rNTPs. The nanotubes are functionalized for cortex formation and membrane deformation. Sequence mutations are shown to produce discrete structural phenotypes—rings versus nanotubes—demonstrating a direct genotype-phenotype link. Large-scale coarse-grained molecular dynamics simulations capture the structural behavior and persistence lengths of different designs. This chapter presents genetic encoding of a minimal, evolvable cytoskeleton.

Chapter 6: Conclusion and Outlook.
The final chapter synthesizes the findings of the thesis, emphasizing the role of genetic encoding in enabling evolvable behavior in synthetic systems. It highlights how RNA cytoskeletons and DNA segregation can be coupled to achieve coordinated cell division. I envision a nucleic acid-based cytoskeleton that not only shapes compartments but also drives their division, paving the way for inheritance. Under this framework, the chapter outlines future directions toward implementing catalytic activity, autonomous replication, and exploring evolutionary processes.

Life is an $n = 1$ experiment. What if we could make it an $n > 1$?

1

Introduction

1.1 Bottom-up construction of life

The challenge of constructing life from non-living matter is one of the most ambitious goals of modern science [1]. Yet any such effort confronts a fundamental question: What is life? Rather than seeking a fixed, universal definition—a pursuit that has long eluded consensus—it may be more productive to adopt operational definitions that evolve alongside our understanding and objectives [2]. Life should not be something to be definitively defined, but as something to be recreated. Can we build systems that exhibit the features of life, and in doing so, reveal how those features arise?

This construction-oriented perspective aligns naturally with the bottom-up approach in synthetic biology, which assembles life-like systems from first principles using well-characterized molecular components. The following section outlines the motivation for this approach, compare it with alternative strategies, and argues that evolvability should be the first feature designed into synthetic life.

1.1.1 Why synthesize life?

The drive to synthesize life reflects a shift in modern biology—from observing life as it is, to actively recreating it. This synthetic approach establishes a powerful learning feedback loop: by studying living systems, we can reverse-engineer their components to better understand the principles that enable life [3]. This endeavor not only offers a mirror to our own biological complexity, but also a sense of agency over it. Yet this pursuit is far from merely introspective. The origin of life remains one of the greatest unsolved mysteries in science [4], and even the simplest cells continue to challenge our understanding. Synthesizing life provides a concrete framework for probing its fundamental principles—revealing how life emerges, and how it might be re-imagined.

Experimental advances in the synthesis of life have shed light on philosophical questions of life, unlocked new biological insights and powered technological innovation. The synthesis of life in the laboratory offers an empirical model for addressing fundamental questions about the nature of life and death, the distinction and transition between life and non-life, and the possibility and practicality of alternative forms of life [5–9]. This research helps reveal the minimal criteria for life to exist, either at its origin on Earth or elsewhere [10–12]. Efforts to engineer and assemble these minimal modules have yielded models and techniques for probing and testing existing biological systems and processes [7, 13–15]. At its core, this quest drives us to engineer, control and customize living systems, enabling us to explore biological systems beyond the constraints set by natural selection [16–18]. The modularity and designability inherent in these engineered systems has, in turn, catalyzed technological breakthroughs, particularly in the fields of biomedicine and materials science [18–23].

Yet constructing life is not solely a biological challenge; it is also a systems engineering problem. Strategies for synthetic life design reflect this compromise between biological complexity and engineering tractability. Current efforts to create life *de novo* generally fall into three categories: top-down, middle-out, and bottom-up approaches.

The top-down, or decomposition approach—historically central in classical systems engineering and one of the earliest productive strategies in synthetic biology—involves systematically stripping down the genome of a living organism to its minimal components, removing non-essential genes to identify a “minimal cell” [24–26]. This strategy leans heavily on natural evolution’s designs, which are optimized for specific environmental niches.

The middle-out approach constructs higher-order systems by composing defined subsystems and then decomposes them for characterization. This bypasses the need to build everything from scratch while offering insights into relationships between modules. In synthetic biology, this involves taking functional modules, such as organelles, membrane mixtures, or cell extracts, from natural cells to reconstruct complex behaviors or repurpose their functions. These components are often treated as black boxes with defined inputs and outputs, without requiring details of their internal mechanisms. While both top-down and middle-out strategies have led to major breakthroughs in recreating life-like behaviors and elucidating the transition from non-living to living matter, they share a core limitation: their dependence on natural biological modules. These strategies assume that such modules remain interoperable even when stripped from their native context, an assumption that rarely holds in the complex, dynamic physicochemical environment of cells.

In contrast, the bottom-up approach builds life from first principles by assembling well-characterized synthetic molecular components into increasingly complex systems. While this demands greater time, effort, and foresight to prevent integration issues, the strategy provides fine-grained control over each component and its internal dependencies [27], avoiding the legacy opacity of natural modules. Unbound by evolutionarily optimized systems, bottom-up design can generate entirely new, orthogonal architectures—realizing *de novo* life. It allows for the construction of deterministic, machine-like systems that are easier to engineer and adapt than the inherently fluid and stochastic nature of living cells. Its tractability allows for clearer causality, facilitates the discovery of generalizable biophysical principles. However, the vast design freedom inherent in bottom-up approaches also demands a clearer and more practical definition of the systems we are aiming to construct.

1.1.2 Building evolvability into synthetic systems

What kind of system should we aim to create in the laboratory when attempting to synthesize life? Traditionally, life has been characterized by a set of hallmarks, including compartmentalization, growth, metabolism, reproduction, response to stimuli, and adaptation through evolution [6, 11]. Most synthetic biology efforts have focused on reconstructing these pillars, aiming to understand their inter-dependencies and ultimately integrate them into a unified living system [8, 28–30]. However, the features associated with life often emerge from complex physico-chemical interactions [31]. Simply assembling functional modules according to an information-processing blueprint is insufficient to synthesize life. Emergent properties must be considered from the outset; otherwise, much like the parable of "the blind men and the elephant" [32]—where each man fails to understand the whole elephant after studying just a part of it— attempts to synthesize life may fail to achieve biological integration [33, 34].

A growing consensus in the field suggests that the ultimate goal of synthesizing life is to build ***"a self-sustaining chemical system from non-living matter capable of open-ended evolution"*** [6], using evolution itself as the guiding design principle (Fig. 1.1a). Evolution acts as a highly parallel optimization algorithm that enables natural systems to adapt, innovate, and maintain robustness in the face of ever-changing environmental perturbations [35, 36].

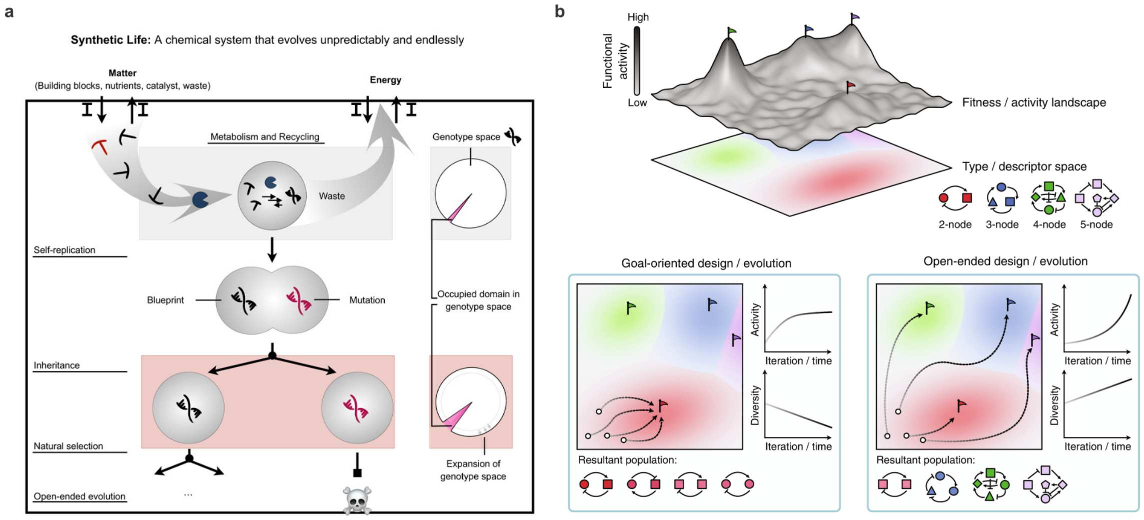

Figure 1.1: Evolvability as a hallmark for the construction of life. **a)** Life is understood as a self-sustaining system that consumes external energy and nutrients to replicate and maintain itself. During replication, genetic mutations introduce variation in both genotype and phenotype, which are then subject to natural selection. When the phenotypic landscape is vast but sparsely occupied, natural selection can drive open-ended evolution, continuously exploring new traits and functions. Image used under a CC BY license from [6]. **b)** Directed evolution versus open-ended evolution. Each entity can be visualized as a point on a fitness landscape, where height reflects functional performance and distance indicates structural difference. Entities may be grouped by type, for example, based on complexity, with flags denoting optimal designs within each category. Directed evolution focuses on goal-oriented improvement, often narrowing diversity and converging on local optima. In contrast, open-ended evolution prioritizes continuous novelty, broadening the search space and allowing for the emergence of unexpected or innovative solutions. Image used under a CC BY 4.0 license from [35].

In synthetic biology, directed evolution has transformed the field [37–42], enhancing biological functions such as enzymatic activity through iterative cycles of mutation (genetic diversity) and selection [43–45]. However, because it is typically goal-driven and constrained by predefined fitness landscapes, directed evolution can trap systems in local optima, preventing the discovery of novel or unexpected solutions (Fig. 1.1b). This limitation is often referred to as the "stepping stone problem", where intermediate innovations that are evolutionarily important may only be recognized in hindsight [35].

Open-ended evolution, even though cannot erase the stepping stone problem, emphasizes exploration over immediate utility, which can help mitigate this challenge. This continuous search for novelty can give rise to entirely new functions, and even evolvability itself (Fig. 1.1b). Building evolvability into synthetic cells from the ground up represents a paradigm shift. Rather than engineering individual functions one by one, we aim to create systems that can autonomously innovate those functions. Once evolvability is in place, other life-like traits, such as metabolism, responsiveness, and division, can emerge or evolve within the system.

Crucially, the key to enabling evolution as a design principle is the genetic encoding of functions. Genetic systems provide a mutable, heritable substrate upon which evolution can act, allowing variation to be generated, selected, and sustained. The next section explores how this genotype–phenotype relationship can be implemented using minimal, bottom-up substrates.

1.2 Genetic encoding of functions in bottom-up synthetic cells

1.2.1 Molecular substrates for evolution

Evolution, defined by Darwin as "descent with modification" [46], is a process that requires both heritability and mutability. This framework depends on genotype-phenotype relationship: functional traits (phenotype) must be encoded in transmissible substrates (genotype). In biological systems, nucleic acids are the primary molecular substrates of evolution, but evolution is not chemically constrained to them. In principle, any molecules that supports heritable replication and generates functional variations could undergo evolution. Prion proteins, for example, undergo protein-based inheritance, where conformational states of misfolded proteins serve as heritable elements and propagate via self-templating [47]. Such system illustrate that evolution is chemically agnostic, provided the requirements for inheritance and diversification are met. This view has motivated investigations into non-canonical substrates for evolution.

Synthetic replicators constructed from peptide-based hexameric macrocycles, for example, have been shown to self-sort and undergo Darwinian evolution [48]. Researchers have also developed xeno-nucleic acids (XNAs)—synthetic analogs of DNA and RNA with alternative backbones or bases—that support sequence variation and selective amplification [49]. Peptide-based replicators have also been shown to exhibit genotype–phenotype coupling in fuel-driven droplets [50]. These studies broaden the conceptual landscape of what counts as a genetic system.

Despite these advances, many synthetic replicators remain limited in their capacity to support open-ended evolution. Most are confined to homo-oligomers or simple sequences, which limits their structural diversity and functional novelty [51]. Additionally, their synthesis and replication can be chemically demanding and challenging to be realized *in situ*, limiting their practical utility in the construction of synthetic cells.

As a result, most bottom-up synthetic biology efforts continue to rely on nucleic acids—specifically DNA and RNA—as the primary substrate for genetic encoding. These polymers possess a unique combination of chemical and structural features that make them well-suited to support heredity.

Their linearity and directionality (defined by 5' phosphate and a 3' hydroxyl ends) allow them to be read and replicated in a precise and sequential manner. This is crucial for faithful templated replication, where the double-helical structure of nucleic acid, stabilized by complementary base pairing (A–T/U and G–C), allows each strand to serve as an exact template for the other (Fig. 1.2, 1.3). This complementarity not only underpins replication but also enables robust proofreading and repair mechanisms.

Although nucleic acids store information in a sequence of four nucleotides with high specificity, their chemical nature also permits controlled deviations. Non-canonical pairs —such as G–T or A–C mismatches in DNA, or G–U wobble pairing in RNA— can form transiently due to chemical tautomerism or structural flexibility. The balance between these occasional errors and the efficiency of repair enzymes helps maintain mutation rates within an evolutionarily useful window.

The chemical stability of DNA, especially its resistance to hydrolysis under physiological conditions, makes it ideal for long-term information storage. RNA, by contrast, is more chemically labile than DNA due to the presence of a 2'-hydroxyl group on its ribose sugar, which makes its backbone more susceptible to hydrolysis—especially under alkaline conditions (Fig. 1.2). However, this structural feature also imparts greater conformational flexibility, enabling RNA to adopt diverse three-dimensional shapes that support catalytic (ribozymes), regulatory (e.g., riboswitches), and structural roles, while still allowing it to function as a genetic template.

In addition to their intrinsic properties, DNA and RNA benefit from a vast and well-characterized toolkit of enzymes and molecular biology techniques—including polymerases, ligases, nucleases, reverse transcriptases and ribozymes —that facilitate their replication, repair, transcription, and manipulation both *in vitro* and *in vivo*. Most importantly, nucleic acids support the genetic encoding of complex cellular functions through the central dogma of molecular biology: DNA is transcribed into RNA, which is then translated into proteins that determine cellular phenotype through their structures and functions.

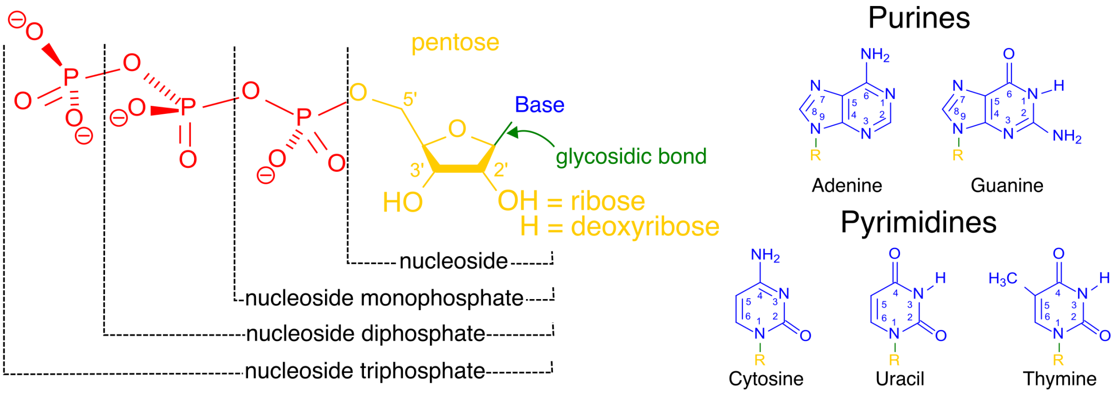

Figure 1.2: Chemical structure of nucleoside triphosphates, the building blocks of nucleic acids. The nucleotide bases: Adenine (A), Guanine (G), Cytosine (C), Uracil (U), and Thymine (T), are shown on the right. Image used from [52].

1.2.2 Towards a minimal system for evolvability

The central dogma architecture underlies most natural evolvability. In theory, this framework could be replicated in synthetic cells to enable the same kind of adaptive potential. Indeed, *in vitro* transcription–translation systems (IVTT) such as the PURE system have been successfully encapsulated in liposomes and GUVs to produce functional proteins from genetic templates [53–55]. These include membrane channels, enzymes, regulatory circuits, and even partially self-regenerating system [56], along with self-replicating DNA system demonstrating Darwian evolution [57].

However, we still lack a complete framework for reconstituting the entire IVTT in a self-replicating form. One major barrier is its sheer biochemical complexity. First, the transcription–translation machinery itself is complex, requiring over 150 gene products and extensive metabolic support [56, 58, 59]. Second, expression in confined compartments is technically demanding: encapsulation efficiency is low, resource pools are finite, and protein folding or degradation often fail under non-native conditions [34, 60]. Third, functional proteins typically require precise spatiotemporal regulation, post-translational modifications, and interactions with co-factors—layers of complexity that are difficult to engineer from scratch[34].

These challenges have motivated alternative approaches. Since early life likely operated via simpler, non-protein-based chemical systems [61], synthetic cell design may benefit from strategies that bypass transcription and translation altogether. Notably, certain biological systems already demonstrate this principle. Viroids—small, circular RNAs that replicate autonomously within plant cells—lack both protein-coding capacity and protective capsids, yet they undergo evolution [62]. Viruses, though more complex, similarly rely on host-derived proteins for genome replication and expression. In this context, constructing a synthetic cell has conceptual parallels with designing a virus-like entity: the genome and compartment can be engineered, while catalytic or structural components are supplied externally. These examples illustrate that evolvability does not require full cellular complexity—only a mechanism for heritable variation and selection.

One promising approach to this challenge is to encode both genotype and phenotype within a single molecular layer—eliminating the need for a dedicated expression system.Nucleic acid nanotechnology provides a promising foundation for this paradigm. Since its inception [63] and the development of DNA origami [64], it has enabled the construction of structural and increasingly functional nucleic acid devices. DNA- and RNA-based architectures—mimicking roles often performed by proteins—have been reconstituted in synthetic compartments such as giant unilamellar vesicles (GUVs) [65–70]. These systems mark early steps toward protein-free functional architectures for bottom-up synthetic cells, where nucleic acids can act simultaneously as genetic material and active machinery.

1.3 Bottom-up functional nucleic acid nanostructures

Nucleic acid nanotechnology harnesses the molecular properties of DNA and RNA—not merely as carriers of genetic information, but as programmable materials for constructing functional architectures. Nucleic acids offer a uniquely tractable design space. Their properties—predictable base pairing, modular motifs, and precise sequence-level control—enable the rational and reproducible construction of molecular systems [71–73]. This programmability has led to the development of sophisticated self-assembling systems, from two-dimensional origami [64] to dynamic molecular machines[74–79].

In the context of synthetic cells, nucleic acid-based assemblies unify information storage and molecular function within a single molecule. This dual role provides both a conceptual and practical shortcut to the central dogma, serving as a substrate for the implementation of evolution in synthetic systems.

1.3.1 DNA and RNA folding

The programmable assembly of DNA and RNA nanostructures derives from their hierarchical folding and assembly logic (Fig. 1.3):

- **Primary structure (1°)**: At the primary level, the linear sequence of nucleotides defines the base-pairing landscape, providing the basis for predictable secondary structures.
- **Secondary structure (2°) and tertiary structure (3°)**: 2° and 3° structures are not rigorously defined and there is disagreement in the community on the categorization of various motifs. Here, we define 2° structures as stable helical regions formed through non-knotted Watson-Crick-Franklin complementary base pairing.
  A key motif in DNA nanotechnology is the 2° four-way Holliday junction, an unstable intermediate in natural genetic recombination. By minimizing sequence symmetry, such that each arm is uniquely sequenced to prevent branch migration, the junction can be stabilized into an immobile form [63]. This immobile junction acts as a programmable node, enabling the construc-

tion of branched architectures and crossovers between helices (Fig. 1.3). The next iteration of geometric rigidity and structural control is achieved through the use of double-crossover (DX) motifs, which connect two helices via two Holliday junctions, allowing precise control over the overall geometry and topology of the assembly.

Paranemic crossover (PX) motifs enable knotting of helices [80, 81] and facilitate the construction of complex RNA architectures like tensegrity triangles [82]. Additionally, high-order assemblies can be folded and stabilized through internal loop interactions [83, 84].

Although these motifs were originally designed for DNA, RNA assemblies operate on the same principles. Other commonly used structural elements include bulges, internal loops, and non-canonical interactions such as G-quadruplexes, i-motifs, and triplexes. While both DNA and RNA can form these motifs, RNA's 2'-hydroxyl group enables a broader repertoire of non-canonical interactions, resulting in more diverse and dynamic architectures.

- **Quarternary structure (4°)**: Oligomerization occurs through a variety of interactions [85], including base-pairing mechanisms such as sticky-end cohesion [86], crossover motifs (DX and PX)[87, 88], and, predominantly in RNA, kissing loops (KLs)[83, 89], loop-receptor interactions [90]. Additionally, non-base-pairing interactions contribute to assembly, involving blunt-end stacking[91–95], ionic bridging [96, 97], or mediation by small molecules [98], polymers [99] and proteins [100–102].

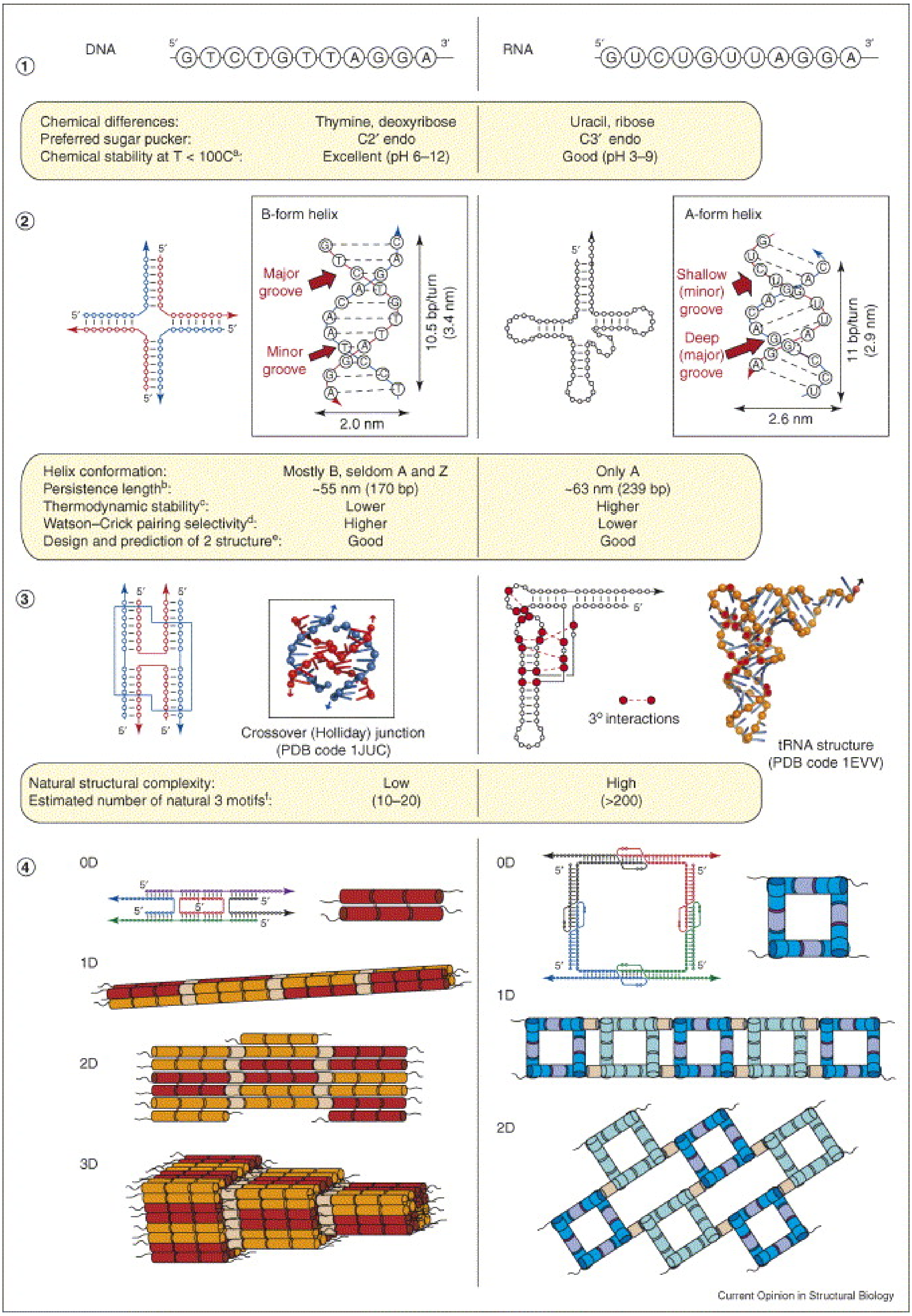

Figure 1.3: Hierarchical folding and assembly logic of DNA and RNA nanostructures. DNA and RNA exhibit modularity across multiple structural levels. (continued on the following page)

Figure 1.3: (continued) At the primary level (1°), the nucleotide sequence defines base-pairing rules and secondary structures (2°) such as helices, junctions, and loops. A Holliday junction is represented in the 2° structure of DNA. These form the foundation for tertiary (3°) motifs, and for quaternary (4°) architectures assembled through interfaces like sticky ends and kissing loops. Differences between RNA and DNA in stability, mechanical rigidity (e.g., persistence length), and degradation pathways further shape their nanostructural behavior. Image reused with permission from [73].

1.3.2 Nucleic acids in bottom-up synthetic biology

Two core factors that make DNA and RNA nanotechnology uniquely powerful for bottom-up synthetic biology are: (i) cheap and reliable synthesis of DNA and (ii) its programmable and efficient self-assembly.

Streamlined DNA synthesis

The success of DNA/RNA nanotechnology depends on the cost-effective, high-fidelity synthesis of arbitrary DNA sequences, particularly short oligonucleotides below 200 nucleotides and DNA gene fragments (200-3000 nucleotides). Automated DNA synthesis enables rapid prototyping, while scalable production methods—e.g., biotechnological fabrication of DNA origami produced in *E. coli* using DNAzyme —facilitate larger-scale fabrication of DNA nanostructures [103].

RNA, by contrast, is harder to synthesize chemically due to its chemical instability and the complexity of protecting groups required during synthesis. However, RNA sequences can be efficiently produced using gene fragments and cloning techniques. The T7 transcription system, in particular, offers a simple and robust platform for *in vitro* RNA synthesis: it requires only a DNA template containing a T7 promoter, ribonucleotide triphosphates (rNTPs), and T7 RNA polymerase to produce high yields of RNA with defined sequence and length. *In vivo*, gene fragments can be cloned into plasmids under the control of promoters and transcribed within bacterial or eukaryotic cells, enabling the expression of structured RNA nanostructures directly inside living systems [104–106].

Programmable and efficient self-assembly

In certain systems, such as hydrogels or networked lattices, simple motifs like branched junctions or nanostars serve as functional building blocks for larger assemblies [107]. In more architecturally complex designs—such as DNA and RNA origami—higher-order structures are formed through the controlled folding of strands into interconnected helical domains. These structures typically feature stem regions in the 7-10 nm range, a scale at which the intrinsic rigidity of double-stranded nucleic acids (with a persistence length of 50-60 nm) enables precise and predictable spatial organization.

Efficient assembly of nucleic acid nanostructures relies on the careful choice of sequence and folding environment to minimize errors and avoid kinetic traps. Folding is often conceptualized as a journey through an energy landscape shaped like a funnel [108], where the system transitions from a high-entropy, high-energy disordered state toward a low-energy, well-folded native structure. However, ruggedness in this landscape—due to kinetic traps or misaligned interactions—can lead to local minima that correspond to misfolded or partially folded intermediates. Strategies such as cooperativity and hierarchical assembly are employed to guide the system toward the correct structure.

Cooperativity is showcased in the case of single-step assemblies [73] such as scaffolded DNA origami [64], DNA tile systems including DNA arrays [109] and DNA nanotubes [110]. This cooperativity comes from the presence of multiple connection points between scaffold and staple strands or among the tiles. Such multivalent binding enhances the overall stability of the assembly and promotes self-proofreading, whereby partially formed or misfolded intermediates are less stable and therefore less likely to persist. In higher-order assemblies, blunt-end stacking interactions ($\pi - \pi$ stacking), which are weaker than sticky-end cohesion, stabilize assemblies when reinforced by multiple contacts [86, 95, 111]. Moreover, cooperativity of 4° interactions can further enhance self-proofreading and structural fidelity.

Hierarchical self-assembly is another strategy used to guide the assembly pathway from 1° to 4° structures. This approach takes advantage of the fact that 2° structures typically form rapidly, while 3° and 4° structures form more slowly [73]. Controlled annealing ramps can be used to enforce this hierarchy, allowing early-forming elements to stabilize before higher-order interactions emerge. This hierarchy can also be introduced experimentally by first forming subunits separately, which are then mixed to assemble supramolecular structures [86, 112]. The melting temperatures of the subunits and the final supramolecular assembly are deliberately kept distinct to enforce sequential folding. Alternatively, algorithmic self-assembly can impose hierarchy by requiring that specific local patterns or substructures form correctly before subsequent assembly steps proceed [113, 114]. Examples of such algorithmic assemblies include criss-cross [115] and tile-based systems [113]. Sequentially decreasing melting temperatures can also be exploited to guide the folding pathway and improve yield [81].

This hierarchical folding strategy is widely employed in nature, particularly in co-transcriptional RNA folding, which makes use of the time lag between the relatively slow nucleotide addition during transcription and the much faster base-pairing (secondary structure formation) of the nascent RNA [116]. This temporal separation allows RNA to fold into hierarchical structures progressively as the chain elongates[83]. We can use these principles to create genetically encoded RNA nanostructures, which can fold autonomously inside cells or synthetic compartments [83, 97, 104–106, 117].

1.3.3 DNA and RNA hardware for synthetic cells

Author contributions and reuse statement

The section below is adapted from my contribution to the textbook The Art of Molecular Programming [118].

The design principles described above have enabled the development of functional DNA and RNA nanostructures that act as programmable hardware in synthetic cells [117, 119, 120] (Fig. 1.4). These structures can be engineered to perform distinct roles across spatial domains: at the membrane interface and within the cell-like interior. In this section, we explore how nucleic acid nanotechnology has been applied to each of these contexts—enabling membrane binding and fusion, mimicking intracellular scaffolds and organelles, and integrating with different types of compartments to build increasingly life-like systems.

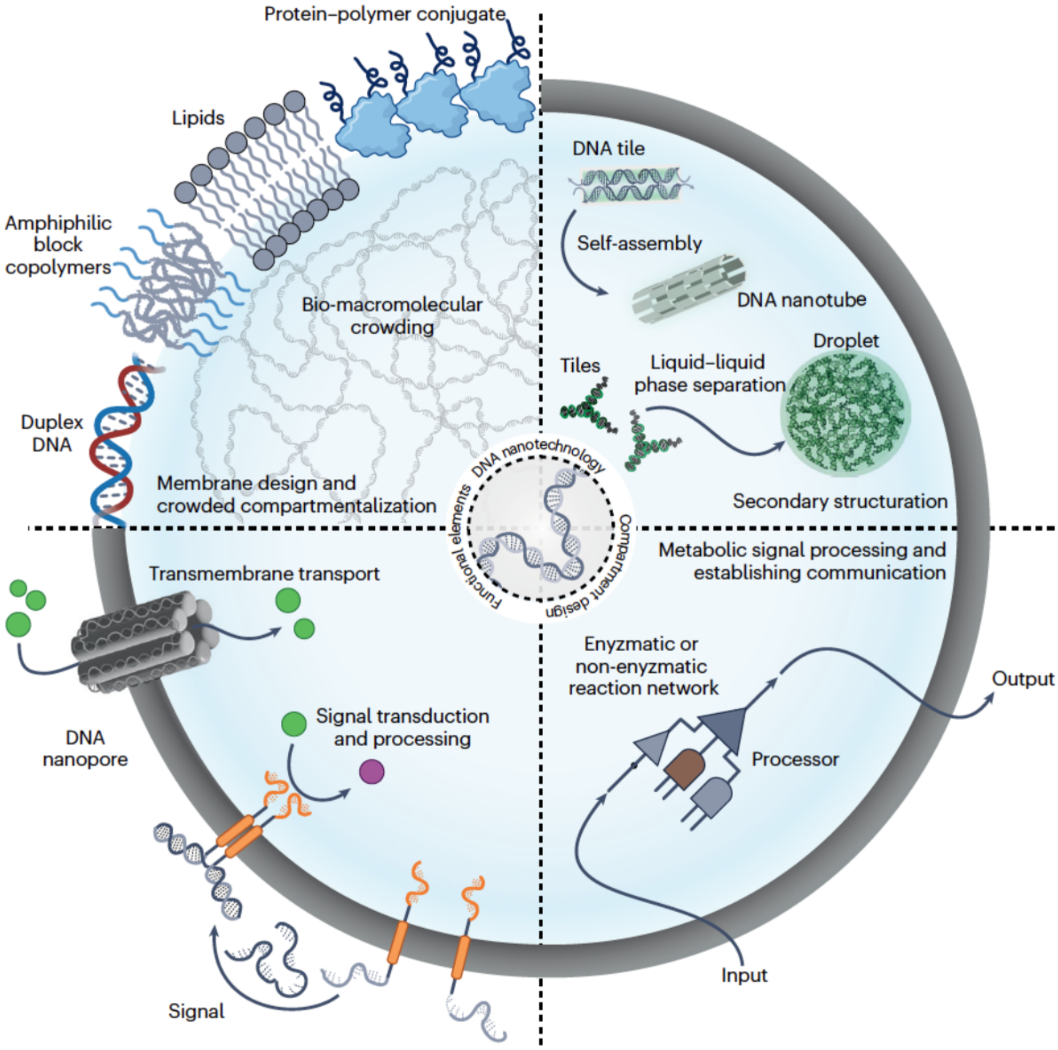

Figure 1.4: DNA as a multifunctional building block for synthetic cells. DNA nanostructures support synthetic cell construction by enabling programmable membrane components, such as nanopores and signaling modules, and internal features like artificial organelles and cytoskeletal scaffolds. DNA can also form compartments or functionalize those composed of other materials. In addition, dynamic DNA reaction networks and computing elements enable information processing, regulation, and adaptive behaviors within synthetic systems. Image used with permission from [119].

Membrane-associated functions

The interaction between nucleic acids and lipid membranes has been explored since the 20th century, particularly for applications such as gene delivery [121, 122]. With the advent of *de novo* DNA and RNA nanostructure design, it has become a logical extension to functionalize these architectures for **membrane binding**—mimicking the role of peripheral membrane proteins in cells.

DNA nanostructures are supramolecular assemblies with highly negatively charged surfaces. Their association with lipid bilayers can be mediated through electrostatic interactions, or covalent attachment of hydrophobic anchors such as cholesterol, porphyrin, or other hydrophobic groups [123, 124]. These strategies have enabled the programmable linking of vesicles [14, 124–126], allowing for controlled membrane interactions and the formation of higher-order vesicle networks [96, 127–129].

Mimicking membrane fusion, a fundamental cellular process involved in endocytosis, exocytosis, and organelle biogenesis, has also been realized with DNA nanotechnology. Inspired by SNARE (SNAp REceptor) proteins—membrane-associated complexes that mediate fusion by bringing bilayers into close contact—synthetic systems use complementary DNA strands anchored to opposing membranes. Upon hybridization, these strands act as molecular zippers, driving membranes together and inducing fusion [130, 131].

Beyond connectivity and fusion, membrane-bound DNA and RNA nanostructures have been used to induce vesicle deformation and remodeling. Morphological changes can result from attachment of nucleic acid structures to the membrane, leading to phase separation [132], budding [133, 134], tubulation [135–137], induced curvature [137, 138] or other deformations [68, 96, 139–141].

Generally, attaching DNA to only one leaflet of the bilayer (i.e., peripheral binding) is technically more accessible than spanning the membrane. However, such peripheral interactions often do not permit molecular communication between the interior and exterior of the vesicle, limiting their use for transmembrane signaling or transport. Overcoming this limitation has led to the development of nucleic acid-based transmembrane devices.

In membrane-bound synthetic cells, DNA nanopore structures [142] enable the selective transport of molecules across lipid bilayers. These pores play a critical role in maintaining out-of-equilibrium conditions by enabling the import of nutrients and the export of waste—both of which are essential before the realization of autonomous metabolism and replication cycles.

To facilitate stable membrane insertion, several strategies have been employed to overcome the energetic barrier associated with embedding highly hydrophilic DNA structures into lipid bilayers [123]. The most common approach involves the functionalization of DNA nanopores with cholesterol tags, which help orient the nanostructure so that insertion occurs only when the hydrophilic region spans the membrane. Alternatives to cholesterol include porphyrin [143], tocopherol, and biotin-modified DNA that binds to biotinylated lipids via streptavidin [144]. The size of these pores can vary significantly, ranging from single duplex channels [145] to structures as large as 30 nm in internal diameter [146].

RNA-based nanopores have also been demonstrated, employing similar cholesterol-mediated insertion strategies to integrate into lipid membranes [147]. Transport through these pores can be purely size-dependent, as cavity dimensions can be tuned to allow or restrict diffusion of specific molecules. However, more advanced selectivity can be achieved through the integration of gating mechanisms. These include strand displacement reactions for reversible opening [148], blocker strands for pore occlusion [149, 150], or aptamer-controlled opening in response to specific molecular signals [150, 151]. Beyond molecular exchange, nanopores can also be engineered to act as signal transduction elements. Some designs employ conformational changes [152] or clustering behavior upon external stimulation [66], enabling synthetic cells to respond to environmental inputs.

Due to their large hydrophilic surfaces, DNA-based pores typically insert into membranes via toroidal pore formation, where the lipid bilayer bends continuously to form a curved, hydrophilic, torus-shaped passage lined by lipid headgroups [145]. This insertion geometry has been shown to induce membrane homogenization across leaflets—mimicking the activity of natural flipase—and to generate localized curvature at the point of integration [153]. However, such membrane perturbations can be limiting in certain applications. To address this, hybrid transmembrane constructs have been developed that incorporate a hydrophobic segment functionalized with DNA on both sides. These constructs can span the bilayer without forming a continuous hydrophilic channel and have been used for signal transduction via dimerization, enabling communication across the membrane without direct material transport [154–156].

While DNA-based membrane technologies are relatively well-developed, the application of RNA nanostructures to membrane interaction has been less extensively explored. A single RNA nanopore design has been reported to date [147], employing cholesterol-mediated insertion similar to strategies used in DNA systems. Additionally, RNA structures capable of membrane binding via aptamer domains have been demonstrated [97, 157], though such examples remain limited.

Intracellular functions

In the development of functional intracellular environments, nucleic acid nanotechnology provides a highly programmable framework for the construction of intracellular architectures. Research in this domain has predominantly concentrated on two principal classes of nucleic acid-based assemblies: cytoskeletal-mimetic filaments that confer mechanical organization, and membrane-less organelles formed via phase separation, which facilitate spatial biochemical compartmentalization.

Nucleic acid nanotubes and other filamentous assemblies have been extensively explored as mimics of the cytoskeleton. First introduced in 2004 [110], these structures—made from DNA [110] (Fig. 1.5a) or RNA [97, 157, 158]—resemble actin filaments or microtubules in both geometry and behavior. Their mechanical properties, including persistence length and bundling, can be tuned through sequence design [110, 158], ionic conditions [96, 97], or molecular crowding [68]. Additionally, their contractile behavior can be modulated by varying the concentration of peptide-based linkers [159]. These nanotubes have been reconstituted inside water-in-oil droplets [160, 161] and giant unilamellar vesicles (GUVs) [68], where they form ring-like structures along the periphery [68] or act as internal scaffolds that alter vesicle morphology during osmotic deflation [68, 97].

Beyond providing structural support, DNA-based cytoskeletal systems can perform dynamic and stimulus-responsive functions (Fig. 1.5b). A variety of designs have demonstrated reversible polymerization in response to diverse molecular cues, including RNA production and degradation [160, 162], molecules binding to DNA aptamers [161], changes in pH [163], reducing agents [164] or external light stimuli [68, 165]. In one approach, DNA origami nanopores were used to localize nanotube nucleation at defined membrane sites, enabling symmetry breaking and spatially controlled cytoskeletal [66]. Furthermore, molecular cargo transport along DNA nanotubes has been achieved using an RNase-mediated burnt-bridge mechanism, mimicking directional intracellular transport observed in natural cytoskeletal systems [161]. [166, 167].

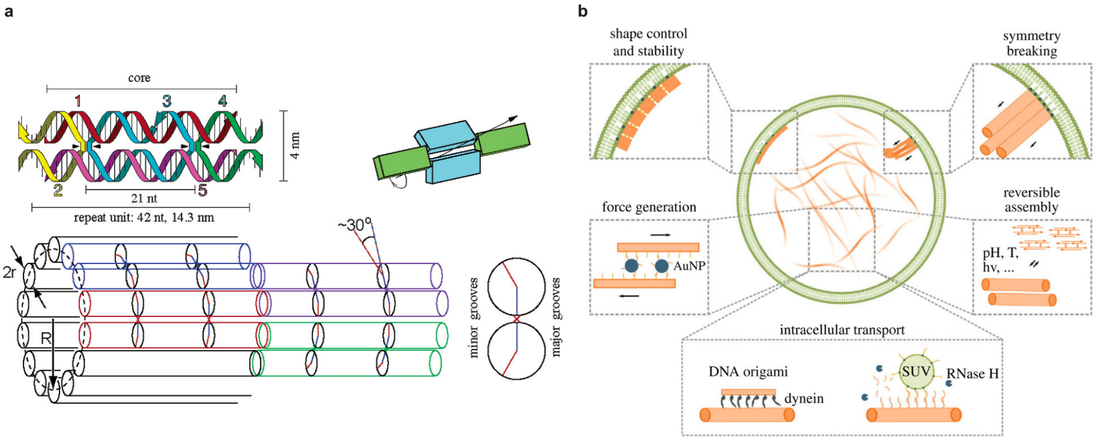

Figure 1.5: Design and function of DNA nanotubes in synthetic cells. **a)** The tile consists of five strands forming a double-crossover (DX) motif with two crossover points spaced two full helical turns apart (21 bases). Sticky ends on strands 2 and 4 mediate inter-tile binding, with two interactions required for stable assembly. The tile's rotational symmetry supports curvature, enabling the formation of nanotubes, illustrated here as a heptagonal arrangement of tiles. A cross-section highlights how crossover geometry and minor groove alignment guide the overall curvature and stability of the tubular structure. Image used with permission from [110] **b)** DNA-based cytoskeletal systems can be tailored to perform various functions, including tuning mechanical properties and shaping compartment morphology, enabling reversible self-assembly, inducing asymmetry, facilitating intracellular transport, and generating mechanical forces. Image used under a CC BY 4.0 license from [168]

Membrane-less organelles, formed via the condensation of DNA or RNA nanostructures through strand hybridization, offer a complementary strategy for intracellular organization. These condensates resemble natural biomolecular organelles such as nucleoli or stress granules, which form through phase separation and allow cells to spatially regulate reactions without membrane boundaries. In nucleic acid systems, sequence-programmed condensation allows for precise control over droplet material properties [169–171], such as stiffness, melting point, and fusion dynamics [172]. DNA nanostars, for instance, can assemble into droplets that grow, fuse, and divide, and can be engineered to phase-segregate [67, 173] (Fig. 1.6). More complex behaviors have also been demonstrated, including layered architectures [166, 174], molecular communication between DNA-based organelles [175], and cortex-like patterning on the inner leaflet of lipid membranes [176].

Moreover, these DNA-based droplets are not merely structural; they can also perform encoded functions. For example, they can sequester genetic material for transcription [177], or compartmentalize enzymatic reactions [166, 167].

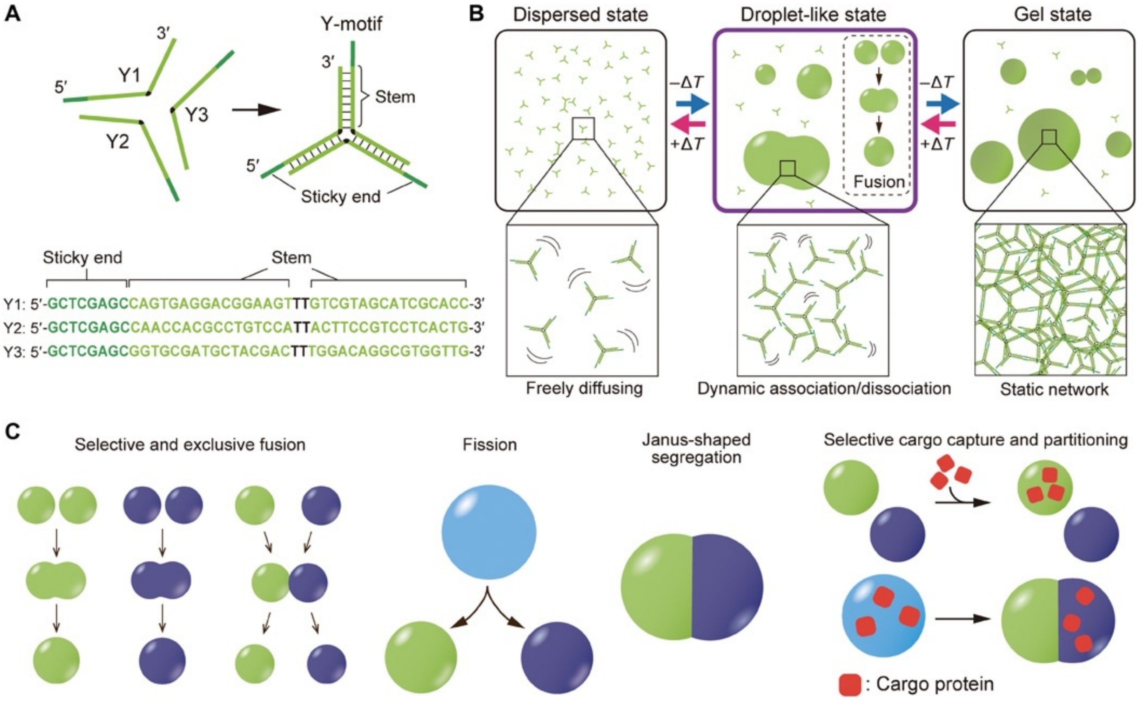

Figure 1.6: DNA droplet formation and sequence-programmable functions. **a)** Schematic of a three-armed DNA nanostar (Y-motif) and its component strands. **b)** The behavior of Y-motifs is temperature-sensitive: at high temperatures, they remain dispersed in solution. As the temperature decreases, liquid–liquid phase separation (LLPS) occurs, leading to the formation of droplet-like assemblies that exhibit liquid-like properties. Further cooling transitions these droplets into a gel-like state. The specific DNA sequences largely determine the temperature at which phase separation occurs. **c)** Sequence design enables programmable control over DNA droplet behaviors and functions. Image used under a CC BY-NC 4.0 from [173].

A particularly powerful advance has been the co-transcriptional formation of RNA-based droplets, in which kissing-loop (KL) motifs drive assembly directly from genetically encoded templates [178–180]. These RNA droplets represent a direct coupling between genotype (DNA) and phenotype (RNA compartment), supporting the evolution of synthetic organelles with distinct material properties [180]. As such, these programmable condensates function both as compartmentalized reaction spaces and as minimal protocell models. These condensates can also be embedded within larger compartments—such as water-in-oil droplets, or lipid vesicles—forming more hierarchical synthetic systems.

1.4 Compartments for synthetic cells

While compartmentalization is not strictly essential for defining life, it plays a central role in biology, biotechnology, and synthetic cell engineering [181]. Among the many compartment models explored in bottom-up synthetic biology, lipid vesicles—particularly giant unilamellar vesicles (GUVs)—have become widely adopted due to their biomimetic structure and compatibility with biochemical tools. Water-in-oil droplets (WODs), on the other hand, offer unparalleled simplicity, low cost, and high-throughput accessibility, making them ideal for screening, directed evolution, and rapid prototyping.

When selecting a compartment, key considerations include size, internal environment, permeability, stability, and formation method (See Table 1.1). Condensates and other emerging systems (e.g., proteinosomes, polymersomes) continue to expand the design space for synthetic compartments [181, 182]. Nevertheless, GUVs and WODs remain the most robust and widely used platforms, and are therefore the focus of this thesis.

Importantly, although many nucleic acid nanostructures have been functionally validated in bulk, relatively few have been characterized under confinement. Yet confinement can significantly alter biophysical behavior and reaction rates [183]. For nanostructures that interact with membranes—such as cytoskeletal mimics—the compartment is not just passive but part of the phenotype, which can be visually screened or selected. This highlights the need for strategies enabling the reconstitution and *in situ* production of functional nanostructures within compartments, allowing bottom-up systems to better model and evolve cell-like behavior.

Table 1.1: Comparison of cell-sized compartment types in bottom-up synthetic biology

Properties	**Water-in-Oil Droplets**	**Giant Unilamellar Vesicles (GUVs)**	**Condensates**
Size	Highly monodisperse via microfluidics Tunable through emulsification parameters	Controlled via emulsion-based methods or microfluidics Asymmetric membrane design	Adjustable via constituting polymer properties
Reaction medium	Aqueous interior surrounded by oil Fast mixing High-throughput screening	Aqueous interior and exterior	Aqueous phase Molecularly crowded environment Favors enzyme activity & phase separation
Permeability	Tunable by surfactant composition & concentration	Semi-permeable membrane Supports cell-like protein insertion and transmembrane transport	Highly permeable Molecular exchange adjustable by composition
Stability	Stable over a wide temperature range Stability depends on surfactant system & evaporation control	Stable under physiological conditions Sensitive to osmotic imbalance without membrane pores	Stable in gelled or condensed phase Prone to dissolution from environmental shifts or degradation
Ease of formation	High-throughput Formed by simple emulsification or microfluidics Low reaction volume	Moderate complexity Careful lipid handling Moderate reaction volume	Easy & scalable Formed by demixing Handling depends on polymer chemistry Moderate reaction volume

Water-in-oil droplets

Water and oil are immiscible liquids, allowing them to form emulsion droplets when mixed. Depending on the water-to-oil ratio, these emulsions can be classified as either water-in-oil (W/O) or oil-in-water (O/W). Typically, water-in-oil droplets are generated with a water content of approximately 20–40%. However, these droplets tend to fuse upon contact, so surfactants are commonly employed to stabilize the droplet interfaces (Figure 1.7). Perfluorinated oils such as Novec HFE-7500, combined with PFPE-based fluorosurfactants, form a widely used system for creating water-in-oil emulsions. These oils exhibit excellent chemical inertness toward biological molecules, owing to their lipophobic and hydrophobic properties, as well as robust thermal and environmental stability. In addition, their gas permeability supports oxygen and carbon dioxide transport within droplets, which is crucial for sustaining living cells in biological assays [184]. Fluorosurfactants, typically used at concentrations of 1–3%, play a critical role in preserving droplet integrity by stabilizing the interface and preventing coalescence. This system enables the scalable and reliable production of uniform water-in-oil droplets, making it particularly well-suited for high-throughput microfluidic applications in biological research.

While WODs are powerful tools for encapsulation and high-throughput experimentation, they lack one critical feature of biological cells: a lipid bilayer membrane. To more closely mimic this natural architecture, several methods have been developed to convert water-in-oil droplets into free-standing lipid compartments [185]. One such approach involves the fusion of small unilamellar vesicles (SUVs) at the droplet interface to form a continuous bilayer, followed by the release of droplet-stabilized GUVs (dsGUVs) into an aqueous environment [186]. This technique enables the transition from oil-based to membrane-bound compartments and will be introduced in the following section.

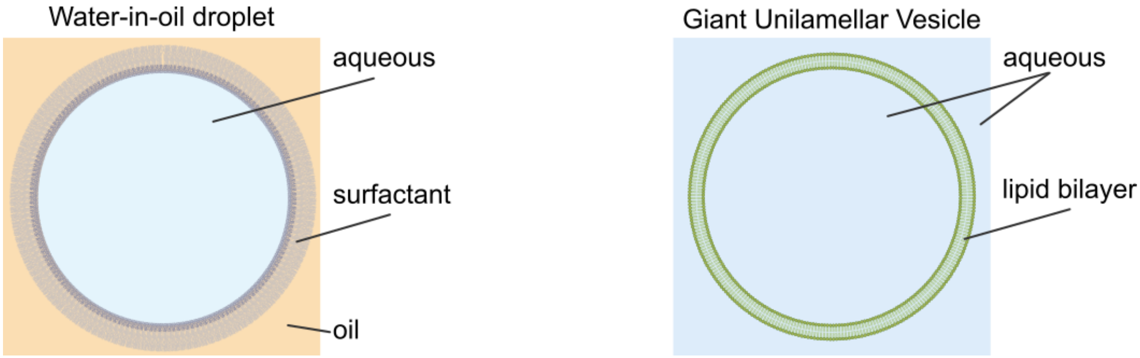

Figure 1.7: Schematics of surfactant stabilized water-in-oil droplet (left) and giant unilamellar vesicle (right).

Giant unilamellar vesicles

Giant Unilamellar Vesicles (GUVs) are microscale vesicles bounded by a lipid bilayer. While their size is comparable to that of natural cells, their membrane composition is far simpler, typically consisting of one or only a few lipid species without embedded proteins or complex structures. This simplicity makes GUVs highly versatile and controllable model systems for studying membrane biophysics, synthetic biology, and cell-like behavior (Figure 1.8) [187]. Several techniques exist for GUV formation, each with its own advantages and limitations [185].

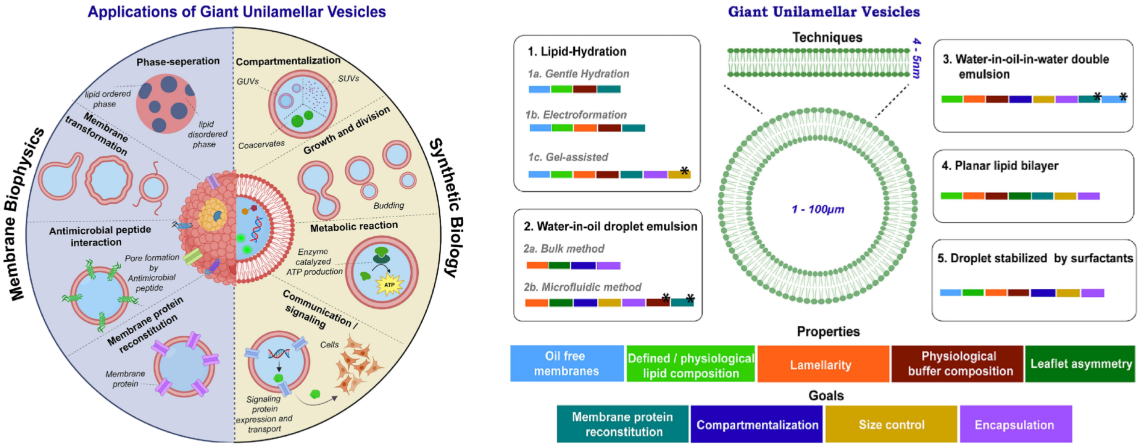

Figure 1.8: Applications of GUVs as a cell model (left) and different methods of GUV production (right). Image used with permission from [187].

In this PhD thesis, I utilized two distinct methods for generating GUVs (Figure 1.9), both of which facilitate the encapsulation of charged molecules within the vesicles.

One of the methods is the droplet-stabilized approach, which relies on lipid bilayer formation at the water–oil interface (Figure 1.9a). First, an aqueous mixture containing small unilamellar vesicles (SUVs), and encapsulated components is deposited on a fluorinated oil phase that contains PEG-based fluorosurfactants. Second, mechanical agitation (such as vortexing) induces the formation of water-in-oil droplets stabilized by the surfactant. Within these droplets, SUVs merge to create a continuous lipid bilayer at the droplet interface, forming structures known as droplet-stabilized GUVs (dsGUVs). This fusion can be done via the use of negatively charged SUVs and ion bridges (the droplet interface is negatively charged due to the presence of Krytox). Finally, the introduction of an aqueous buffer along with a destabilizing agent triggers the removal of the surfactant and oil, resulting in the release of free-standing GUVs into the aqueous environment.

The second approach is based on gel-assisted lipid film hydration, which offers a complementary strategy for generating free-standing GUVs (Figure 1.9b). In this approach, a lipid film is applied onto a porous polymer gel layer. Upon hydration, the gel enhances the influx of buffer solution beneath the lipid layer. This buffer flow enables the swelling of lipid bilayers into GUVs more quickly and efficiently than traditional natural swelling methods.

a. Droplet-stabilized GUVs

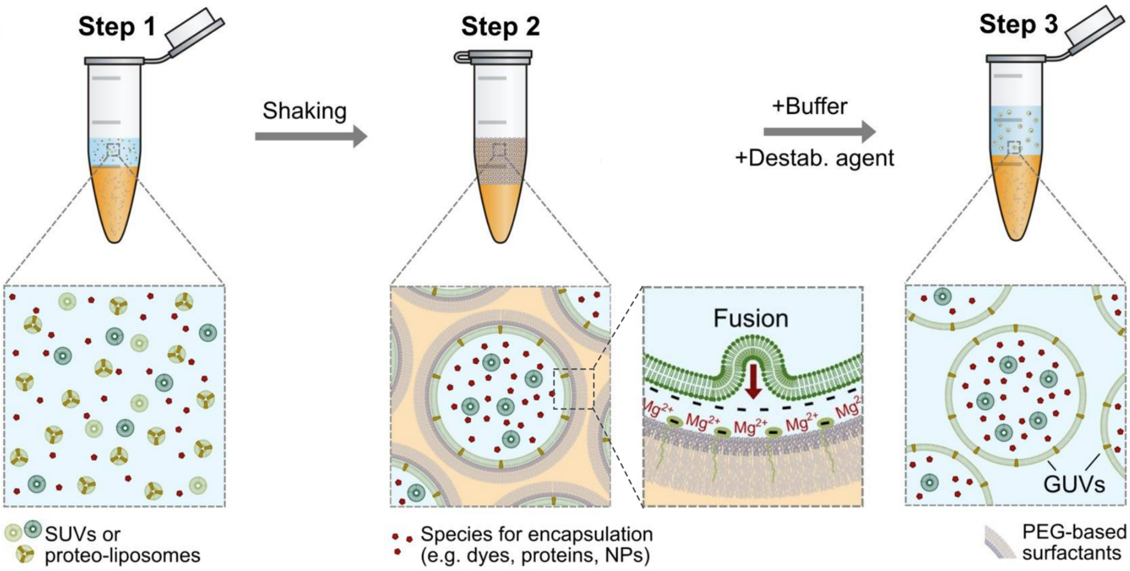

b. Gel-assisted lipid-film hydration

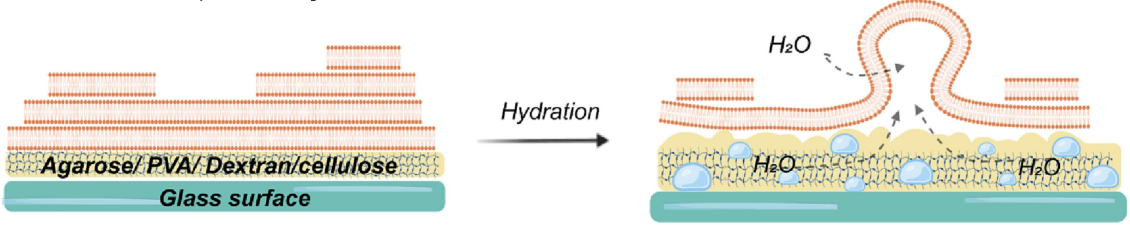

Figure 1.9: GUV formation methods employed in this thesis. **a)** A schematic overview of the three-step "shaking" approach used to generate GUV-based synthetic cells [186]. Image used under a CC BY license from [186]. **b)** Schematic representation of the gel-assisted swelling method for GUV formation. Image used with permission from [187].

1.5 Research gaps and thesis roadmap

An evolvable system requires more than modular and functional nanostructures; it demands that both the spatial organization of genotype and the physical behaviors of phenotype be genetically encoded and subject to selection. Two fundamental gaps currently limit this vision. First, there is no generalizable strategy for the programmable segregation of genetic material, a basic requirement for inheritance and selection. Second, structural components such as cytoskeletal mimics are often introduced externally—particularly with functional chemical modifications like membrane anchors—rather than being expressed *in situ* from encoded templates, making it difficult to incorporate selection or evolutionary processes into the system.

This thesis addresses these two limitations through complementary studies. The first investigates genetically encoded DNA condensates as a programmable module for spatial segregation of DNA. The second explores the *in situ* transcription and self-assembly of RNA origami-based nanotubes as a minimal, genetically encoded cytoskeleton. By integrating these systems within cell-sized compartments, this thesis examines how genetically encoded spatial organization can couple genotype and phenotype, laying the foundation for evolvable behavior in synthetic cells.

DNA segregation module for synthetic cells (Chapter 4)

A foundational requirement for an evolvable synthetic cell is the ability to replicate and partition genetic information in a way that supports inheritance and selection. While a range of strategies have been developed to reconstitute growth and division in synthetic cells [188–191]—particularly in lipid vesicles [192–197]—genetic material is typically distributed through random partitioning during division [192, 198, 199].

Although stochastic partitioning of genetic material during division can support basic replication cycles—and may be buffered by group selection mechanisms such as the stochastic corrector model [200]—this inherent randomness imposes significant constraints on long-term, open-ended evolution. Beneficial genetic variants that arise in one lineage may be lost purely by chance, particularly in divisions where uneven gene distribution leads to nonviable progeny. Such drift-driven loss restricts the accumulation of genetic complexity and novelty, thereby limiting the system's evolutionary potential.

There is therefore a clear need for a programmable DNA segregation module in artificial cells [188]. However, natural segregation systems—such as the eukaryotic mitotic spindle or the bacterial ParABS machinery—remain too complex to be reconstituted within bottom-up synthetic systems [188, 201]. A promising alternative lies in exploiting physical phenomena relevant to confined polymers, such as entropic segregation, which has been shown to drive spontaneous partitioning of dense macromolecules in confined geometries [202, 203].

Among candidate mechanisms, liquid–liquid phase separation (LLPS) provides a compelling route to DNA compartmentalization through the formation of DNA droplets (see Section 1.3). Despite their promise, studies of DNA droplet fission have primarily focused on bulk-phase behavior and have largely neglected the role of confinement or cell-sized encapsulation. Yet it is within confinement that the spatial phenotype of DNA condensates—as segregating or dividing bodies—becomes directly relevant to inheritance and evolution in synthetic cells. However, their spatial dynamics under confinement have not yet been fully explored or theoretically modeled.

This work addresses that gap by engineering a genetically encodable DNA droplet system capable of undergoing enzymatic and light-triggered spatial segregation within cell-sized compartments. By tuning the DNA sequences of the constituent strands, genotype is directly coupled to droplet fission behavior. In parallel, a mathematical model is developed to describe the segregation dynamics of DNA condensates under confinement.

Genetic encoding and expression of RNA origami cytoskeletons in synthetic cells (Chapter 5)

While Chapter 4 addressed the inheritance of genetic material through DNA droplet segregation, evolvability also requires that structural phenotypes be both genetically encoded and selectable. However, current implementations of DNA and RNA nanostructures in synthetic cells are constrained by several key limitations:

- Using DNA as both genetic carrier and structural material imposes design conflicts and limits evolvability. Decoupling these roles—retaining double-stranded DNA for information storage and using single-stranded RNA for functional structures—restores modularity and expands the design space.
- Most functional DNA nanostructures require chemical modifications (e.g., cholesterol for membrane anchoring), complicating their genetic encoding and autonomous expression inside vesicles. In contrast, RNA benefits from extensive biotechnological tools for *in vitro* and *in vivo* evolution, and natural RNA motifs (such as aptamers and ribozymes) provide a rich source of functional modules. Its chemical and structural diversity makes RNA an ideal candidate for constructing evolvable nanostructures.
- Many nucleic acid systems operate near thermodynamic equilibrium, both in their formation and in their functional activity. This limits their ability to support the out-of-equilibrium, energy-consuming dynamics characteristic of living systems.
- Even when DNA nanostructures are genetically encoded, they often require post-processing—such as purification and thermal annealing—to become functional [204]. Self-replicating DNA nanostructures avoid this to some extent, but remain limited in structural complexity due to design constraints [205].

This chapter explores an alternative: using RNA origami as a genetically encoded functional nanostructures. RNA origami structures can be transcribed directly from DNA templates by RNA polymerase. This strategy enables the out-of-equilibrium production of complex RNA architectures with minimal biochemical machinery.

RNA origami folds co-transcriptionally through a hierarchical pathway (see Section 1.3), allowing for the rational design of diverse structures, wherein multiple sequences can yield similar structures. Furthermore, the rich variety of non-canonical interactions in RNA broadens the range of possible sequences that can fold into functional structures, making it easier for structural traits to evolve through simple mutations in the DNA template.

As a proof of concept, this work demonstrates the *in situ* transcription and assembly of RNA origami nanotubes within giant unilamellar vesicles (GUVs). Transcription is externally triggered using either α-hemolysin nanopores or small-molecule ionophores, which enable selective transport and dynamic control over gene expression. The synthesis of these nanotubes consumes rNTPs as chemical fuel, highlighting their nature as out-of-equilibrium systems. Structural parameters—such as length and rigidity—can be tuned via sequence design. Functionalization with membrane-binding motifs enables cortex-like formation, and in some cases, cytoskeleton-induced vesicle deformation. Notably, even minor sequence variations can lead to distinct structural outcomes, including the formation of closed-loop nanorings, revealing a rich and evolvable sequence–structure-function landscape. In parallel, this work also establishes a coarse-grained molecular dynamics framework capable of simulating micrometer-scale assemblies, enabling predictive modeling of the physical behavior of RNA origami-based cytoskeletal structures.

In contrast to previous work on the encapsulated transcription of RNA aptamers or ribozymes, this study establishes a direct link between genotype and cellular phenotype—specifically, cytoskeletal architecture and membrane morphology. By embedding RNA-based structures within a transcriptionally active environment, we are a step closer to a minimal and potentially evolvable pathway for constructing intracellular organization—marking a key step toward the development of evolvable synthetic cells. The evolution of a cytoskeleton capable of dividing compartments, coupled with genetically encoded DNA segregation, would connect the two core results of this thesis into a coherent framework for synthetic cell evolution.

2

Background

2.1 Confocal fluorescence microscopy

Fluorescent DNA droplets and RNA cytoskeletons in this thesis were visualized using a confocal laser scanning microscope (CLSM). This technique is based on the fundamental principles of fluorescence [206] combined with the CLSM's ability to generate a focused excitation point and selectively detect fluorescence only from the focal plane by rejecting out-of-focus light [207].

In confocal laser scanning microscopy (CLSM), fluorescence is produced by shining a focused laser onto a sample containing fluorophores, molecules that can absorb and then re-emit light. When a fluorophore absorbs a photon from the laser, one of its electrons may be excited to a higher energy state. According to the Franck-Condon principle, this electronic transition occurs much faster than nuclear motion, meaning that the nuclei remain essentially stationary during excitation—resulting in a vertical transition on an energy diagram (Fig. 2.1a).

However, not all absorbed photons result in fluorescence emission. The efficiency of this process is described by the quantum yield, defined as the ratio of emitted photons to absorbed photons [208]. Some of the absorbed energy can be dissipated through non-radiative pathways such as internal conversion or intersystem crossing. In this work, fluorescence from RNA origami structures is achieved using light-up RNA aptamers, which are intrinsically non-fluorescent but become fluorescent upon binding to specific small-molecule dyes [209]. Binding to the aptamer restricts the dye's structural flexibility, such as limiting rotational or vibrational motions that would otherwise enable non-radiative decay. This restriction reduces non-radiative energy loss and thereby increases the quantum yield, leading to enhanced fluorescence [210].

After excitation, the electron rapidly relaxes to the lowest vibrational level of the excited state, releasing some energy as heat. Then, within nanoseconds, the electron returns to the ground state by emitting a photon. The emitted light has lower energy (longer wavelength) than the absorbed light due to previous energy loss, which is known as the Stokes shift (Fig. 2.1b) [206].

The sequence of energy levels and transitions involved can be illustrated by a Jablonski diagram, which shows how molecules absorb energy, undergo vibrational relaxation, and then emit fluorescence (Fig. 2.1c) [206]. All these physical processes: the rapid, vertical electronic transitions (Franck-Condon principle), the red shift in emission (Stokes shift), and the stepwise transitions (Jablonski diagram), together explain how fluorescence arises in CLSM and why the emitted light is always at a longer wavelength than the excitation light.

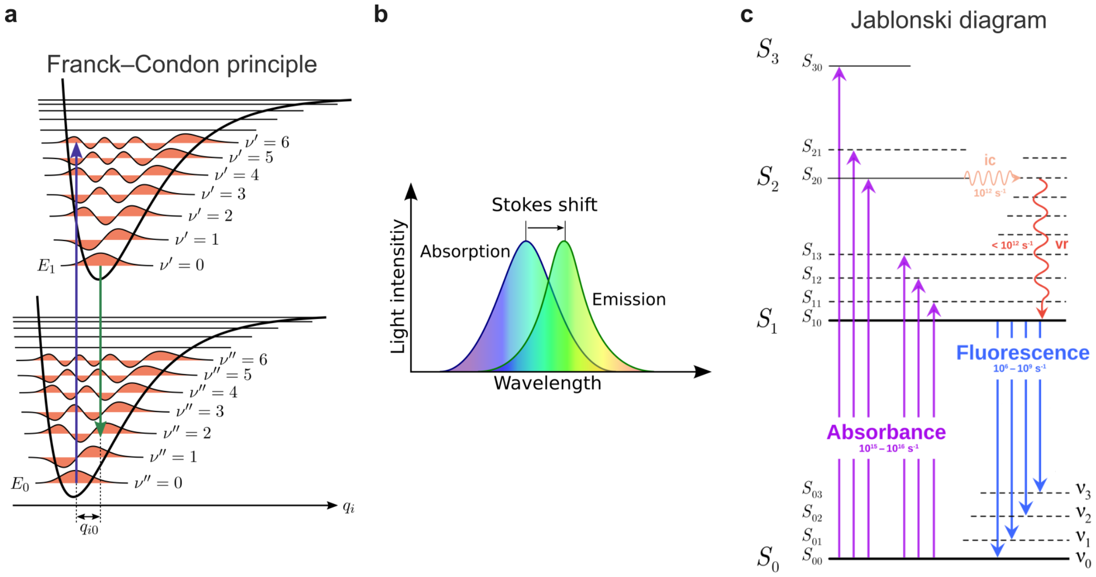

Figure 2.1: Schematic diagram of the physical processes in fluorescence. **a)** The energy diagram showcasing the Franck-Condon principle. Image used under a CC BY-SA 3.0 license from [211]. **b)** Spectra diagram indicating the Stokes shift between absorption and emission light. Image used under a CC BY 4.0 license from [212]. **c)** The Jablonski diagram. Vibrational levels of absorbance, non-radiative decay (internal conversion: ic and vibrational relaxation: vr), and fluorescence are shown with their rate constants. Image used under a CC BY 4.0 license from [213].

In CLSM, a highly focused laser beam excites fluorophores within the sample at a diffraction-limited spot. Although the laser illuminates only a very small region at any instant, scanning mirrors rapidly move this spot across the sample, sequentially illuminating the entire field of view over time. The emitted fluorescence from the excited spot passes back through the same objective lens and reaches a dichroic mirror, which reflect the shorter-wavelength excitation light toward the sample while allowing the longer-wavelength emitted fluorescence to pass through to the detector (Fig. 2.2). A pinhole aperture placed in a conjugate image plane on the detection path blocks most out-of-focus light coming from regions above or below the focal plane (Fig. 2.2) [207]. This selective detection improves image contrast and sharpness by rejecting haze which is common in wide-field microscopy, resulting in optical sectioning of thick or scattering samples [214]. The size of the pinhole can be adjusted to balance signal intensity and section thickness. By combining focused excitation, scanning, and pinhole-based detection, CLSM builds high-resolution images point-by-point, capturing fluorescence only from the illuminated focal spot at each instant.

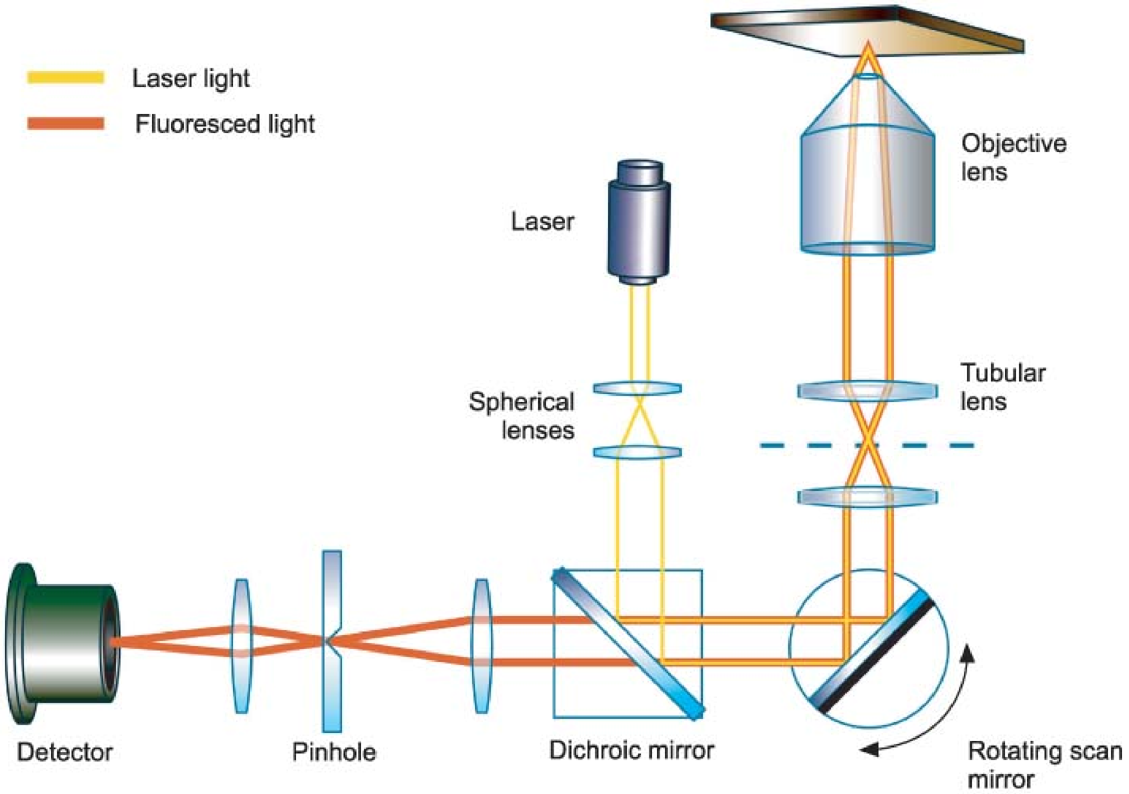

Figure 2.2: Schematic diagram of the beam path of a confocal laser scanning microscope. A focused laser beam excites a single point within the sample, while scanning mirrors rapidly move this excitation spot across the specimen to build an image. The dichroic mirror reflects the excitation light toward the sample and allows the longer-wavelength emitted fluorescence to pass through to the detector. A pinhole aperture positioned in a conjugate image plane blocks out-of-focus light, enabling optical sectioning and enhancing image resolution. Image used under a CC BY-NC 3.0 license from [215].

2.2 Atomic force microscopy of nucleic acid origami

To accurately characterize the correct formation and persistence length of the RNA nanotubes discussed in Chapter 5, atomic force microscopy (AFM) was employed. AFM allows visualization of nanoscale structures such as RNA nanotubes with a diameter of approximately 11 nm, which are beyond the resolution limits of conventional CLSM.

Beyond its nanoscale resolution, AFM is particularly well suited for screening large numbers of samples and experimental conditions. It enables rapid, label-free imaging of RNA nanotubes for comparing structure and mechanics across conditions [216]. Compared to other high-resolution techniques such as electron microscopy or super-resolution fluorescence microscopy, AFM offers a simpler and faster workflow, avoiding the need for fluorescent labeling or lengthy sample preparation [217]. This makes it an efficient and accessible method for both structural confirmation and mechanical analysis of RNA-based assemblies.

The fundamental principle of AFM involves mechanical magnification through the deflection of a micro-cantilever fitted with a sharp nanoscale tip [216]. During scanning, the AFM tip interacts with the sample surface, causing cantilever deflections that are detected by reflecting a laser beam from the back of the cantilever onto a photodetector (Fig. 2.3a). Nanoscale deflections of the cantilever result in changes in the laser spot position on the detector, which are converted into electrical signals. These signals feed a feedback system that precisely adjusts the cantilever position via a piezoelectric scanner, providing sub-nanometer accuracy and rapid response to maintain constant tip-sample interaction (Fig. 2.3b). This enables real-time, high-resolution topographical mapping of the surface [216].

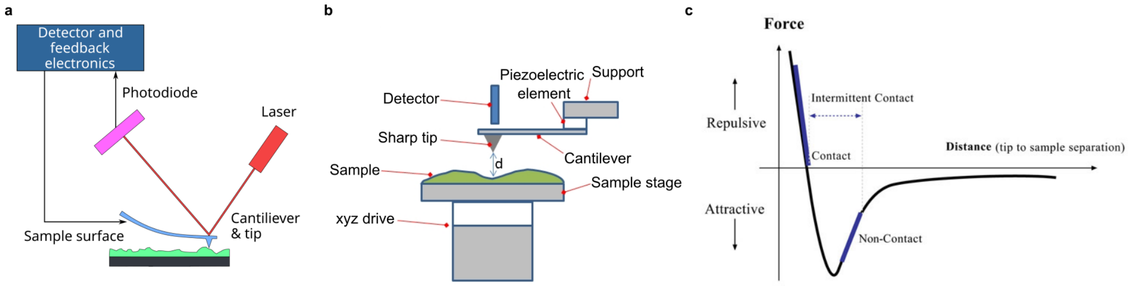

Figure 2.3: **a-b)** Schematic of the setup of an AFM. Image adapted under a CC BY-SA 4.0 license from [218]. **c)** Lennard-Jones potential and the regimes where different imaging modes operate. Image used under a CC BY 4.0 license from [219].

The interaction between the AFM tip and the sample surface is modeled as a Lennard-Jones potential, which describes both attractive and repulsive forces at the nanoscale (Fig. 2.3c) [220]. In contact mode AFM, the tip remains in continuous contact with the surface, operating primarily in the repulsive regime. However, for delicate biological samples such as RNA nanotubes, tapping mode (also known as AC mode or intermittent contact mode) is preferred. In tapping mode, the cantilever oscillates near its resonance frequency, periodically contacting the surface, which reduces lateral forces and minimizes damage or pushing to the soft biomolecules. This mode also enhances image contrast by sensing both topography and material properties.

AFM imaging of nucleic acid structures is commonly performed on mica mineral surfaces. Although both nucleic acids and mica carry strong negative charges, the binding of nucleic acids to the mica surface is facilitated by divalent magnesium ions (Mg^{2+}), which act as ionic bridges between the two. This interaction enables stable adsorption of nucleic acid structures onto the mica substrate, allowing for high-resolution imaging. Note that this adsorption can distort the structures, resulting in the opening of nanotubes [110] or flattening of structures [221].

2.3 Persistence length analysis

In this thesis, RNA origami nanotubes are used as genetically encoded cytoskeletal elements in synthetic cells. To understand their mechanical behavior and potential to support cellular functions such as compartment shaping or division, it is essential to quantify their stiffness. One key parameter for describing the flexibility of such filamentous structures is the persistence length.

The worm-like-chain (WLC) model depicts a continuously flexible isotropic rod. Experimental data of stretching double-stranded DNA display a clear signature of WLC elasticity, with a persistence length of ~50 nm [222]. WLC models have been widely used for characterization of biological polymers such as dsRNA [223], intermediate filaments [224], actin filaments, and microtubules [225] (persistence length of ~60 nm, 1 µm, 17 µm, and 5 mm, respectively).

Theoretically, persistence length is a mechanical property quantifying the bending stiffness of a flexible isotropic rod and can be calculated as:

$$P = \frac{EI}{k_B T} \tag{2.1}$$

Where P is the persistence length, E is the Young's modulus, I is the second moment of area, k_B is the Boltzmann constant, and T is the temperature. In a rigid and uniform rod, I can be expressed as:

$$I = \frac{\pi a^4}{4} \tag{2.2}$$

where a is the radius of the circular cross-section.

In experimental polymer physics, the persistence length can be calculated from the end-to-end distance of the polymer using the relation:

$$\langle R^2 \rangle_{3D} = 2sPL\left(1 - \frac{sP}{L}(1 - e^{-L/sP)}\right) \tag{2.3}$$

Where $\langle R^2 \rangle$ is the mean squared end-to-end distance, P is the persistence length, and L is the contour length. s is a surface parameter which is equal to 2 for a 2D surface, and 1 for 3D measurements. Fitting image data from liquid AFM-imaging to the 3D WLC model yields persistence length estimates in agreement with those obtained in stretching experiments [226]. Therefore in this thesis, the persistence length of RNA nanotubes is calculated using $s = 1$.

“The problem is to see reality as it is.”

Thich Nhat Hanh

3

Materials and Methods

Author Contributions and Reuse Statement

This chapter is the combined Material and Methods from:

1. **Mai P Tran**, Rakesh Chatterjee, Yannik Dreher, Julius Fichtler, Kevin Jahnke, Lennart Hilbert, Vasily Zaburdaev, Kerstin Göpfrich; ‘A DNA segregation module for synthetic cells’, *Small* (2022) `https://doi.org/10.1002/smll.202202711`
2. **Mai P Tran***, Taniya Chakraborty*, Erik Poppleton, Luca Monari, Maja Illig, Franziska Giessler, Kerstin Göpfrich; ‘Genetic encoding and expression of RNA origami cytoskeletons in synthetic cells’, *Nat. Nanotechnol.* (2025), `https://doi.org/10.1038/s41565-025-01879-3`

3.1 Materials

DOPC (1,2-dioleoyl-*sn*-glycero-3-phosphocholine, cat #850375), DOPG (1,2-dioleoyl-*sn*-glycero-3-phospho-(1’-*rac*-glycerol) (sodium salt), cat #840475) in chloroform were purchased from Avanti Polar Lipids. The membrane dye DiD (1,1’-Dioctadecyl-3,3,3’,3’-Tetramethylindodicarbocyanine, 4-Chlorobenzenesulfonate salt, cat #D7757) and T7 RNA polymerase (cat #EP0112) were purchased from Thermo-Fisher Scientific. Sodium chloride (cat #S9888), Magnesium chloride (cat #M8266), Sodium acetate (cat #S2889), Potassium chloride (cat #P3911), Sodium hydroxide (cat #S5881), Polyvinyl alcohol (cat #S8062894), DL-Dithiothreitol (cat #DO632), Sucrose (cat #S0389), Tris-acetate (cat #T1258), Glucose (cat #G6152), Magnesium-Ionophor I (N,N’-Diheptyl-N,N’-dimethyl-1,4-butandiamid)(cat #63082) and α-hemolysin from Staphylococcus aureus (cat

#H9395) were purchased from Sigma-Aldrich. Magnesium acetate tetrahydrate (cat #A322119) was purchased from Merck. Phusion® High-Fidelity PCR Kit (cat #E0553S) and RNase Inhibitor, Murine (cat #M0314) were purchased from New England Biolabs. Nuclease free water was purchased from Integrated DNA Technologies. Microscopy experiments were performed in 18-well μ-slide glass bottom chambers (cat #81817) from Ibidi. If not explicitly mentioned above, further details regarding the materials can be found in the Methods section below.

3.2 Sequences

3.2.1 DNA droplet sequences

Name	Sequence(5'-3')
G-1	GCTCGAGCCAGTGAGGACGGAAGTTTGTCGTAGCATCGCACC
G-2	GCTCGAGCCAACCACGCCTGTCCATTACTTCCGTCCTCACTG
G-3	GCTCGAGCGGTGCGATGCTACGACTTTGGACAGGCGTGGTTG
B-1	CTCGCGAGAAAGGAACTCTCCGCGTTGACAAAGCCGACACGT
B-2	CTCGCGAGGCCTCTGTGTCGCATCTTCGCGGAGAGTTCCTTT
B-3	CTCGCGAGACGTGTCGGCTTTGTCTTGATGCGACACAGAGGC
L-2	CTCGCGAGCTCAGAGAGGTGACAGCATTCCGTTCCGTTAGTCCAGC
L-3	CTCGCGAGCCATGGTCCCAAGTGATGTTTGCTGTCACCTCTCTGAG
L-5	GCTCGAGCCAGACGTCACTCTCCAACTTCGCAAATTTACAGCGCCG
L-6	GCTCGAGCGTGCTGGCATACCTGACTTTGTTGGAGAGTGACGTCTG
L-1-RNA	CTCGCGAGGCTGGACTAACGGArArCrGrGrUrUrArGrUrCAGGTATGCCAGCAC
L-4-RNA	GCTCGAGCCGGCGCTGTAAATTrUrGrCrGrUrUrCrArUrCACTTGGGACCATGG
L-1-Photo	CTCGCGAGGCTGGACTAACGGA*ACGGT*TAGTC*AGGTATGCCAGCAC
L-4-Photo	GCTCGAGCCGGCGCTGTAAATT*TGCGT*TCATC*ACTTGGGACCATGG
G-free-1	GCTCGAGC**A**CAGTGAGGACGGAAGTTTGTCGTAGCATCGCACC
G-free-2	GCTCGAGC**A**CAACCACGCCTGTCCATTACTTCCGTCCTCACTG
G-free-3	GCTCGAGC**A**GGTGCGATGCTACGACTTTGGACAGGCGTGGTTG
B-free-1	CTCGCGAG**A**AAAGGAACTCTCCGCGTTGACAAAGCCGACACGT
B-free-2	CTCGCGAG**A**GCCTCTGTGTCGCATCTTCGCGGAGAGTTCCTTT
B-free-3	CTCGCGAG**A**ACGTGTCGGCTTTGTCTTGATGCGACACAGAGGC
L-2-Cy3	[Cy3]-CTCAGAGAGGTGACAGCATTCCGTTCCGTTAGTCCAGC
L-5-Cy5	[Cy5]-CAGACGTCACTCTCCAACTTCGCAAATTTACAGCGCCG
L-2-ATTO647N	[ATTO647N]-CTCAGAGAGGTGACAGCATTCCGTTCCGTTAGTCCAGC
L-5-ATTO488	[ATTO488]-CAGACGTCACTCTCCAACTTCGCAAATTTACAGCGCCG
L-2-ATTO488	[ATTO488]-CTCAGAGAGGTGACAGCATTCCGTTCCGTTAGTCCAGC
L-5-ATTO647N	[ATTO647N]-CAGACGTCACTCTCCAACTTCGCAAATTTACAGCGCCG
G-2-FAM	[6-FAM]-CAACCACGCCTGTCCATTACTTCCGTCCTCACTG
B-2-DY405	[DY405]-GCCTCTGTGTCGCATCTTCGCGGAGAGTTCCTTT

Table 3.1: Oligonucleotide sequences for DNA droplets.
The sequences are adapted from [173]. "G", "B" and "L" in the "Name" column are abbreviations for green, blue, and linking motifs respectively. All the sticky-end sequences and the fluorescent modifications are indicated in the color of the population to which the sequence belongs. The two spacer bases (TT, rUrU) are colored in gray. RNA and photolabile sequences are highlighted in orange and magenta, respectively. Ribonucleotides are preceded with a letter "r". Positions of nitrobenzyle linkers are marked with an asterisk. The free adenine base is highlighted in bold.

3.2.2 DNA templates for RNA origami

DNA template name	Sequence	Forward Primer	Reverse Primer
3H-4DT-iSpi	GGGCATTCTAATACGACTCACTATAGGAACCGTCATCAGAGCGGCCACGTGTTGATCCGCTGTAGGGGTCAACATGTGCGGTGCGCCGTTCGCGGTGCAGGAGTACCAGGCGAGT GGGCGGTCGGTACGTCCACTTGCCTGGTGCTCCCTCTTTGAGTGAAGGACATACACTCAGAGAGCCGCTCTGGAACCTAAAATGCACATAGGTTTCAGAGGCCGTTCTGGTGATG GTTCCCTGTCATGGACCGTGGTCGCGACGTAAGTGCATAACGTTGCGATCGTGGCAGGGGAAAATGTCCATCCCTTGCCGCGACATCGGGGCCATCATCCTACCGACGGATGGTG GCCCTGATGCCACGTGTTGTTTCGACAGCACACATACTACAGCTATGTGGTTCATGGCAGTTCCGCTGTTGAGTAGAGTGTGGGCTCCAGTTCGCTGGTGAGGGTCGGGTCCAGCG	**T7 primer**	**iSpi primer**
S2T	GGGCATTCTAATACGACTCACTATAGGAACTACTTCCCGGGAGGTTCGCCTCCCGAGTAGTTAATCGGTGAAGCTACTATTTACCTGACTCGTTAATCTGCCAGTGAACACCGAAC ACTGGACCGGTTGAGTAGAGTGTGGGCTCCGCGTTTAGCTTCGGCTAGACGTGGTGAGGGTCGGGTCCCGGTGGGGCGAAGGGACGGTGCGGAGAGGAGAGCCCCTAGGTTGGT GGGTCGGGTAGATGGAGGTGG	**short T7 primer**	**S2T primer**
WT	GGGCATTCTAATACGACTCACTATAGGAAGGAGCATTGATTGAAGCAAGCACGATCAGCGAACATTTCGATGTTGATGTGAACAACCTACGCATCCCTCATGCAACTGCTTAGCG TGAGGCGCGAATGCAACGAGATAGCGTTCATGCTTCTTCCGTACCGCGATGGCGGGGTGAAATCTCGACGCCCTACGTGAAAAGCAGACGCGTACCTACCTGAAGCTTGCACGG GTAGGCGCTCGCTTCGGCGACGTAATGAAAGGTTGACGTTACGCATCGTGGTAC	**T7 primer**	**WT primer**
iSpi	GGGCATTCTAATACGACTCACTATAGGAAGGAGCATTGATTGAAGCAAGCACGATCAGCGAACATTTCGATGTTGATGTGAACAACCTACGCATCCCTCATGCAACTGCTTAGCG TGAGGCGCGAATGCAACGAGATAGCGTTCATGCTTCTTCCGTACCGCGATGGCGGGGTGAAATCTCGACGCCCTACGTGAAAAGCAGACGCGTACCTACCTGAAGCTTGCACGG GTAGGCGCTCGCTTCGGCGACGTAATGAAAGGTTGACGTTACGCATCGTGGTACTTTCCGCTGTTGAGTAGAGTGTGGGCTCCCATTCGTGGGTGAGGGTCGGGTCCAGCGG	**T7 primer**	**iSpi primer**
dsOV	GGGCATTCTAATACGACTCACTATAGGAAATTGATTGAAGCAAGCACGATCAGCGAACATTTCGATGTTGATGTGAACAACCTACGCATCCCTCATGCAACTGCTTAGCGTGAGG CGCGAATGCAACGAGATAGCGTTCATTTCCGCCGTAGGTTGCGATGGCGGGGTGAAATCTCGACGCCCTACGTGAAAAGCAGACGCGTACCTACCTGAAGCTTGCACGGGTAGG CGCTCGCTTCGGCGACGTAATGAAAGGTTGACGTTACGCATCGCGACCCTGATGAGCCTGGATACCAGCCGAAAGGCCCTTGGCAGTTAGACGAAACGGT	**T7 primer**	**dsOV primer**
WT-mut-polyU	GGGCATTCTAATACGACTCACTATAGGAATTTTTTTTTTTCGCATGAGGAGCACGTGAAGCGAGAACGCGTGGGGTTCCCTTCGGGGAAGCGCTGAATTGCCAACGGCGCGAACC TGCAAATGAGGAGCGGGTTCCCCGCCTGAAAGCTATCATCGGGCCTCCTTATGCGCGACCGAGAAAGCCGTATGAAGATAGCACGTACGCGGTGAACCTCATACGCCGCTTTTCT TGAATCTCGCACGAGAAAAGGCGCATTTCGATGCCCCACTGAATGGCAAACGGTGGGTTTCTTGGTCG	**T7 primer**	**WT-mut primer**
WT-mut	GGGCATTCTAATACGACTCACTATAGGAATGAGGAGCACGTGAAGCGAGAACGCGTGGGGTTCCCTTCGGGGAAGCGCTGAATTGCCAACGGCGCGAACCTGCAAATGAGGAGC GGGTTCCCCGCCTGAAAGCTATCATCGGGCCTCCTTATTCCCGACCGAGAAAGCCGTATGAAGATAGCACGTACGCGGTGAACCTCATACGCCGCTTTTCTTGAATCTCGCACGA GAAAAGGCGCATTTCGATGCCCCACTGAATGGCAAACGGTGGGTTTCTTGGTCG	**T7 primer**	**WT-mut primer**
WT-biotin-iSpi	GGGCATTCTAATACGACTCACTATAGGAAGGAGCATTGATTGAAGCAAGCACGATCAGCGAACATTTCGATGTTGATGTGAACAACCTACGCATCCCTCATGCAACTGCTTAGCG TGAGGCGCGAATGCAACGAGATAGCGTTCATGCTTCTTCCGTACCGCGATGGCGGGGTGAAATCTCGACGCCCTACGTGAAAAGCAGACGCGTACCTACCTGAAGCTTGCACGG GTAGGCGCTCGCTTCGGCGACGTAATGAAAGGTTGACGTTACGCATCGTGGTACAAAGGACCGTCAGAGGACACGGTTAAAAAGTCCTCTAAAACCGCTGTTGAGTAGAGTGTGG GCTCCCATTCGTGGGTGAGGGTCGGGTCCAGCGG	**T7 primer**	**iSpi primer**

Table 3.2: DNA template sequences and primers used for transcription of RNA origami

Primers (name)	Sequences
T7 primer	GGG CAT TCT AAT ACG ACT CAC TAT A
short T7 primer	GGGCATTCTAATACGACTCA
S2T primer	CCACCTCCATCTACCCGACC
iSpi primer	CCGCTGGACCCGACCCTCAC
WT primer	GTACCACGATGCGTAACG
dsOV primer	ACC GTT TCG TCT AAC TGC
WT-mut primer	CGA CCA AGA AAC CCA CCG

Table 3.3: Primers used for Polymerase Chain Reaction (PCR) amplification of the DNA templates

3.2.3 RNA origami blueprints

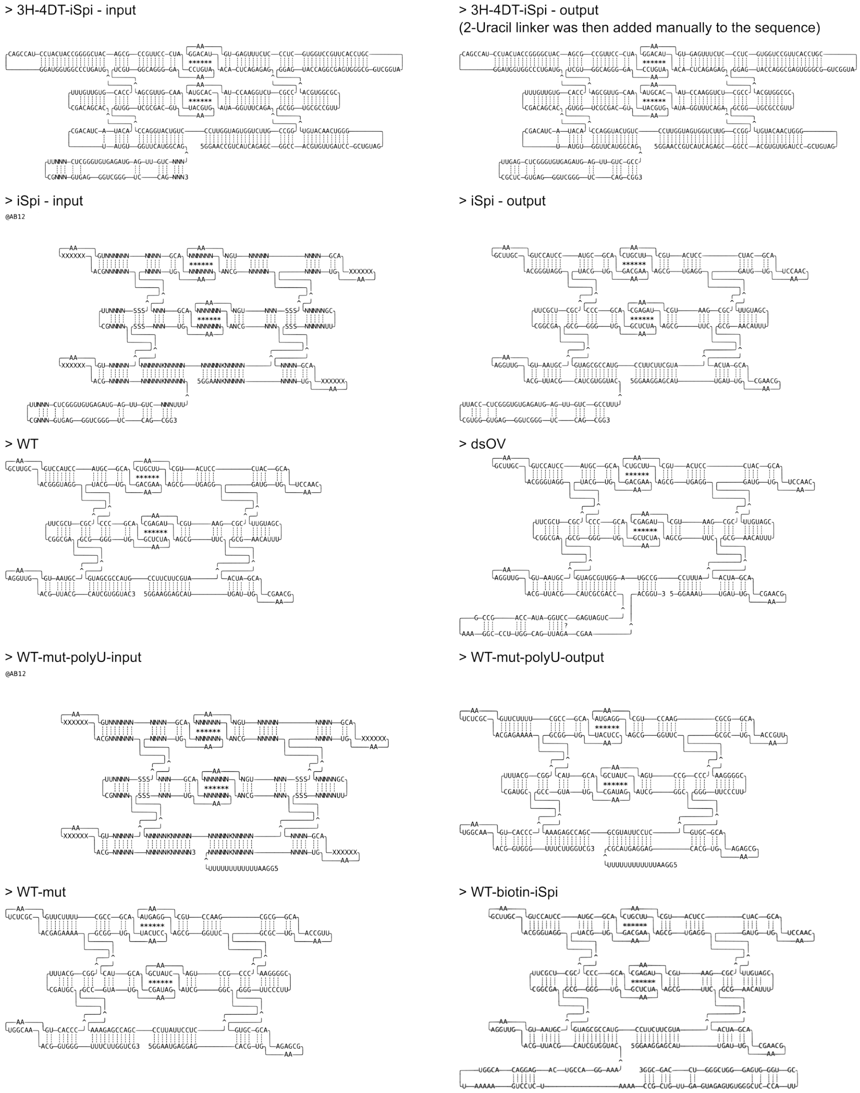

Figure 3.1: The blueprints of all RNA origami designs used as input for the RNA origami design software ROAD. For the designs where the blueprint was used as an input for Revolvr [89], the input and output blueprints were specified. All blueprint text files are uploaded on GitHub (see Code Availability).

3.3 Methods

3.3.1 DNA and RNA design and preparation

Annealing of DNA droplets

The oligonucleotides were purchased from Integrated DNA Technologies (IA, USA, purification: cartridge (OPC)–grade purification); modified oligonucleotides were purchased from biomers.net (Ulm, Germany, purification: high-performance liquid chromatography (HPLC)). The oligonucleotides were dissolved at 100 µM in 10 mM Tris-HCl buffer (pH 8.0) containing 1 mM EDTA purchased (Merck Millipore, MA, USA) and stored at −20 °C for further use.

The DNA strands were mixed in an Eppendorf PCR tube at different concentrations as described in Table 3.4 in 10 mM Tris-HCl buffer (pH 8.0) containing 1 mM EDTA and 350 mM NaCl. The DNA strands were then annealed on a C1000 Touch^{TM} Thermal Cycler from Bio-Rad (CA, USA). The sample was heated at 85 °C for 1 min and then cooled down to 25 °C at a rate of $-1\,°C\,min^{-1}$. The annealed DNA droplets were then pelleted using a Centrifuge 5804 from Eppendorf (Hamburg, Germany) at 10 000 g at 4 °C for 15 min. The supernatant was then discarded and the DNA droplets were re-suspended in the buffer of choice depending on the experiment (see Chapter 4). The volume added for resuspension is 0.25× the initial volume. The concentrated DNA droplets were then stored for up to three days at room temperature in a dark box to prevent photocleavage or used immediately for further experiments.

Strand name	Final concentration [µM]
G-1	5
G-2	5
G-3	5
B-1	5
B-2	5
B-3	5
L-1	1.65
L-2	1.15
L-3	1.65
L-4	1.65
L-5	1.15
L-6	1.65
L-2-ATTO647N	0.5
L-5-ATTO488	0.5

Table 3.4: DNA mixing ratios.
The standard mix for our DNA droplets is shown below. Depending on the DNA droplet type, the mixture can be adjusted. For example: photocleavable droplets consist of L-1-Photo and L-4-Photo while enzyme-labile droplets contain L-1-RNA and L-4-RNA. For different combinations shown in Fig. 4.13, all three strands of G- or B- will be replaced with G-free- and B-free- strands. For labelling, 30% of the non-fluorescent strands will be replaced with the mentioned fluorescent strands.

Annealing of DNA droplets without linking motifs

The DNA strands were mixed in an Eppendorf PCR tube at 5 µM per strand in 10 mM Tris-HCl buffer (pH 8.0) containing 1 mM EDTA and 350 mM NaCl. For the original droplets, G and B strands were used (see DNA sequences, Table below). For the modified droplets, G-free and B-free strands were used. For labeling, 30% of G-2 and G-free-2 strands were replaced with G-2-FAM and 30% of B-2 and B-free-2 were replaced with B-2-DY405. The DNA strands were then annealed as described above.

Design of RNA origami

The design of the RNA tiles was guided by the principles established by Geary et al. for ssRNA origami [227].

The 3H-4DT-iSpinach blueprint was generated by adding the iSpinach module to the 3' end of the 3H-4DT design from Geary et al. [89]. The iSpinach aptamer was connected to the core design by a 2 Uracil linker.

The blueprints for the nanotube-forming tiles were designed based on the 3H-3DT tile from Geary et al. [89]. The first and third helices were extended so that the helical turn of the external 180° kissing loops would align upon assembly. This extension process was done manually via cycles of extension and visualization using the RNAbuild script from ROAD [89] and ChimeraX [228] to minimize the distance between kissing loops upon closure of the tube. During this process, the length of the helices were also adjusted so that the internal kissing loops would correspond to 8 base pair duplexes instead of the original 9 in the 3H-3DT design, reflecting the updated understanding of internal kissing loop geometry based on cryoEM structures [229].

The blueprint of the iSpi design was then put into Revolvr [89]. The final sequence was chosen using two criteria: both external kissing loop pairs should have binding energy below $-8\,\mathrm{kcal\,mol^{-1}}$; and the difference in binding energy between the two pairs should be minimal. The WT design was created by removing the iSpi overhang. The dsOV was introduced into the tile blueprint without further sequence optimization. All blueprints were used as input for the trace_analysis script from ROAD [89] to check for folding irregularities and then used for oxRNA simulations.

The blueprints of the mutated ring-forming tiles were generated as described in Chapter 5 and the sequence optimization was performed in the same manner described for the other tiles.

The RNA origami containing biotin aptamer was designed by concatenating the WT, biotin aptamer and iSpinach aptamer in the following sequence: WT tile-AAA-biotin aptamer-AAAA-iSpinach aptamer. The sequence was then checked using RNAfold Web Server [230] to ensure correct folding of each aptamer in the concatenated sequence.

Synthesis of RNA origami in bulk

DNA templates were synthesized as double-stranded gBlocks from Integrated DNA Technologies (IDT). DNA gBlocks (0.5 ng µL^{-1}) were PCR-amplified using 14–25-nt primers (Table 3.3), using Phusion© High-Fidelity PCR Kit (NEB) with annealing temperature at 62 °C. The PCR product was then purified using a Qiagen PCR purification kit. RNA was transcribed and co-transcriptionally folded in a one-pot reaction containing PCR purified DNA template (4 ng µL^{-1}), $Mg(OAc)_2$ (6 mM), NaOAc (40 mM), KCl 40 mM, Tris-OAc (50 mM, pH 7.8), rNTPs (1 mM each), dithiothreitol (DTT) (1 mM), and DFHBI-1T dye (62.5 µM) and RNase inhibitor (1 U µL^{-1}), if not described otherwise. Reactions were initiated by adding T7 RNA polymerase (0.2 U µL^{-1}). Transcription reactions were carried out in 100 µL volumes at 37 °C for 2 h to 12 h, depending on the sequence length. Nanotube designs required longer transcription times (4-12 h). All the experiments were performed using nuclease-free water.

RNA origami bundling

RNA was transcribed *in vitro* for 2 h. Subsequently the samples were heated to 75 °C for 1 min and then cooled down to 25 °C with a temperature gradient of $-0.5\,°C\,min^{-1}$ in a thermocycler (BioRad). For bundling, 1 µL of annealed RNA origami was mixed with 20 µL of imaging buffer (40 mM Tris-Acetate containing 1 mM EDTA and 20 mM Mg^{2+}) and deposited onto a freshly cleaved mica to adsorb for 5 min. The AFM images were processed using Gwyddion. Five width measurements, equally distributed along the measured object, were performed and the averaged widths were reported in Chapter 5.

Fluorescence assay in bulk

3H-4DT RNA origami with an iSpinach fluorophore was prepared with PCR purified DNA template (4 ng µL^{-1}), NaOAc (40 mM), KCl (40 mM), Tris-OAc (50 mM, pH 7.8), rNTPs (1 mM each), dithiothreitol (DTT)(1 mM), DFHBI-1T dye (62.5 µM) in four different conditions of $Mg(OAc)_2$ (*i*.e. 0 mM, 1 mM, 1 to 6 mM, 6 mM). In 1 to 6 mM sample, first 1 mM $Mg(OAc)_2$ was added for 2 h and then up to 5 mM of $Mg(OAc)_2$ added for the next 2 h. To measure the fluorescence intensity, 100 µL final volume was pipetted into a Greiner 96-well black bottom plate (Sigma-Aldrich) which was finally placed inside the plate reader (Spark multimode plate reader from Tecan Life Science) for 4 h at 37 °C. RNA production was quanified by measuring the emission of DFHBI-1T upon excitation with 488 nm (DFHBI-1T dye: $\lambda_{ex} = 482$ nm, $\lambda_{em} = 505$ nm) with a gain of 100 (manually set).

3.3.2 Confocal microscopy

Preparation of the heated observation chamber

Standard range smart substrates (SmS) measuring 18 mm by 18 mm with a thickness of 0.17 mm were purchased from Interherence GmbH (Erlangen, Germany). For experiments with GUVs, the SmS was coated with 1% (w/v) BSA (bovine serum albumin, SERVA Electrophoresis GmbH, Germany) for at least 5 min to prevent fusion of the GUVs with the glass surface. After the BSA coating, the SmS was washed with deionized water and dried under an airflow. A coverslip (measuring 9 mm by 6 mm with a thickness of 0.17mm) was assembled onto the heating region of the SmS using double-sided sticky tape. The sample solutions were immersed into the slit between the SmS and the coverslip, and the edges were sealed with two component dental glue.

Confocal Imaging

The samples in the custom-built observation chamber were imaged with a confocal laser scanning microscope LSM 900 (Carl Zeiss AG, Oberkochen, Germany). The pinhole aperture was set to one Airy Unit and heat required experiments were performed with the temperature control unit VAHEAT from Interherence GmbH (Erlangen, Germany). All images were acquired on a LSM 900 confocal laser scanning microscope from Carl Zeiss AG, Germany equipped with two excitation lasers (488 nm and 640 nm). The images in Chapter 4 were acquired using a 20× objective (Plan-Apochromat 20×/0.8 M27, Carl Zeiss AG). For the live observation of the RNA origami expression, the 20x air objective was used. Expression of RNA origami nanotubes was imaged using a 63x water objective. The GUV membrane was labelled with DiD ($\lambda_{ex} = 644\,\mathrm{nm}$, $\lambda_{em} = 665\,\mathrm{nm}$) (Sigma-Aldrich). The RNA origami contained an iSpinach aptamer which binds the fluorophore DFHBI-1T.

3.3.3 Atomic force microscopy

RNA origami solution was pre-diluted to avoid structure overlap on the mica, if necessary. Subsequently, 20 µL of the solution mixed with 20 µL of imaging buffer (40 mM Tris-Acetate containing 1 mM EDTA and 20 mM Mg^{2+}) were deposited onto a freshly cleaved mica surface (0.95 cm diameter, Science Services GmbH, Munich, Germany) and allowed to adsorb for a minimum of 1 min. The liquid chamber was then filled with 1 mL of imaging buffer. The sample was imaged using Nanowizard 2 high-speed atomic force microscope (Bruker) in either AC fast imaging mode or $\mathrm{QI}^{\mathrm{TM}}$ mode with a JPK Nanowizard ULTRA Speed using FASTSCAN-D cantilevers (f = 110 kHz, k = $0.25\,\mathrm{N\,m^{-1}}$, Bruker Nano Inc., Camarillo, CA, USA).

For characterization, the three RNA origami designs (WT, iSpi and dsOV) underwent IVT as described in Methods, Synthesis of RNA origami in bulk. For the conditions with dye, the IVT was carried out in presence of DFHBI-1T dye at 62.5 µM. RNA origami was then purified using centrifugal filters with a pore size of 100 kDa (Merck Millipore). The filters were pre-wetted with 1x PBS (pH 7.4) containing 20 mM Mg^{2+}. IVT solution was then added to the filter and filled up to 500 µL with the same buffer. After centrifugation for 5 min at 13 000 g, the solution was adjusted up to 50 µL with 1x PBS. The purified solution was then directly deposited on mica for AFM imaging as described above.

3.3.4 Encapsulation methods

Encapsulation of DNA droplets into water-in-oil droplets

For the formation of water-in-oil droplets, the DNA droplet-containing aqueous phase was layered on top of the oil phase in a volumetric ratio of 1:3 within a microtube (Eppendorf). For the segregation of DNA droplets using enzymatic activity, RNase A purchased from Promega (WI, USA) was added at a final concentration of $20\,\mu g\,mL^{-1}$ before putting the aqueous phase onto the oil phase. Droplet formation was induced by manual flicking for about 10 times to produce cell-sized droplets. To stabilize the water-in-oil droplets, perflouro-polyether-polyethylene glycol (PFPE-PEG) block-copolymer fluorosurfactants (008-PEG-based fluorosurfactant) purchased from Ran Biotechnologies, Inc. (MA, USA) was dissolved in HFE-7500 oil purchased from DuPont (DE, USA) at a concentration of 3 % v/v to withstand high temperature.

SUV formation

1,2-dioleoyl-sn-glycero-3-phosphoglycerol (DOPG), and 1,2-dioleoyl-sn-glycero-3 -phosphocholine (DOPC), were purchased from Sigma-Aldrich (Darmstadt, Germany), stored in $CHCl_3$ at $-20\,°C$ and used without further purification. Small unilamellar vesicles (SUVs) were formed by mixing DOPG and DOPC at a 30%:70% molar ratio in a glass vial and later dried gently under a stream of nitrogen gas. The vial was kept under vacuum in a desiccator for 30 min to remove traces of $CHCl_3$. The dried lipid film was re-suspended in 10 mM Tris-HCl buffer (pH 8.0) containing 1 mM EDTA at a lipid concentration of 8 mM. The solution was vortexed for at least 10 min to trigger liposome formation and subsequently extruded to form homogeneous SUVs with ten passages through a polycarbonate filter with a pore size of 100 nm purchased from Avanti Polar Lipids, Inc.(AL, USA). SUVs were afterwards stored at 4 °C for up to 3 days or used immediately for GUV formation.

One-pot assembly of GUVs

To prepare the aqueous solution, the DNA droplet pellet was re-suspended in the initial buffer at a 6.67× increased concentration. The re-suspended DNA droplet solution was then denatured at 95 °C for at least 5 min on a C1000 Touch™ Thermal Cycler from Bio-Rad (CA, USA). The aqueous solution consisted of 25% v/v SUV solution (containing 8 mM lipids as prepared above) and 60% v/v denatured DNA solution in 10 mM Tris-HCl buffer (pH 8.0) containing 1 mM EDTA and 350 mM NaCl. The oil–surfactant mix contained HFE-7500 fluorinated oil (3M, Germany) with 1.4 wt% 008-PEG-based fluorosurfactant (RAN Biotechnologies, MA, USA) and 10 mM PFPE–carboxylic acid (Krytox, MW, $7000\text{-}7500\,g\,M^{-1}$, DuPont, Germany). The aqueous solution was layered on top of the oil-surfactant mix in a volumetric ratio of 1:3 inside a microtube (Eppendorf). The tube was manually shaken for about 30 s until water-in-oil droplets formed. The SUVs fused to form a spherical supported lipid bilayer at the droplet periphery and created droplet-stabilized GUV (dsGUV). The dsGUVs tube was stored at 4 °C for 3 h before release. The same buffer at equal volume to the aqueous solution was pipetted on top of the droplet layer. To destabilize the droplets for release, perfluoro-1-octanol (PFO) destabilizing agent (Sigma-Aldrich, Germany) of the same volume was added slowly. Within a minute, the milky emulsion disappeared and formed a transparent aqueous layer on top of the oil–surfactant mix. The released GUVs in the transparent aqueous layer were carefully removed with a pipette and transferred into another microtube. The released GUVs were stored at room temperature in a dark box for up to three days or used immediately for further experiments.

Formation of DNA droplets in GUV

To form DNA droplets inside the GUVs, the released GUVs were incubated on a C1000 Touch^{TM} Thermal Cycler from Bio-Rad (CA, USA) at 85 °C for 1 min and then cooled down to 25 °C at a rate of $-1\,°\mathrm{C\,min^{-1}}$. The denatured DNA inside the GUVs and in the solution re-annealed into DNA droplets. The solution was then either immediately put on an observation chamber for imaging or stored at room temperature in a dark box for up to three days before imaging.

Encapsulation of pre-formed DNA droplets in fluorescently labelled GUV

SUVs were prepared using 1,2-dioleoyl-sn-glycero-3-phospho ethanolamine-N-(lissamine rhodamine B sulfonyl) (ammonium salt) (Liss Rhod PE, purchased from Sigma-Aldrich, Germany), DOPG, and DOPC mixed at 1%:30%:69% molar ratio. SUV formation was done as described in Experimental section.

The aqueous solution was then prepared and used for GUV formation using method described in Experimental section. For enzyme-induced DNA droplet segregation in GUV, DNA droplet pellet was re-suspended in the initial buffer for a concentration of 4× then mixed with RNase A at a final concentration of $20\,\mathrm{µg\,mL^{-1}}$.

Gel-assisted swelling of GUVs

GUVs were prepared by the polyvinylalcohol (PVA)-gel assisted swelling method [128, 231]. In detail, a PVA solution was prepared by mixing 5% (w/v) PVA (MW: 145 000 Da) in nuclease-free water with sucrose (100 mM) for 24 h, at 400 rpm, at 90 °C. The PVA solution (50 µL) was dried as a thin film on a glass slide (60 mm x 24 mm) at 50 °C for 30 min. Then, 5 µL of a lipid mixture in chloroform containing 10 mol% DOPG ($10\,\mathrm{µg\,µL^{-1}}$) and 1 mol% DiD dye in $10\,\mathrm{µg\,µL^{-1}}$ DOPC was spread onto the PVA layer and dried for 1 h at 37 °C. The DiD dye stock solution ($10\,\mathrm{µg\,µL^{-1}}$) was prepared in chloroform. Using a Teflon chamber (ca. 40 mm x 24 mm) as a spacer and a second glass slide, a chamber was assembled on top of the slide with the lipid-coated PVA. Then, the lipids were hydrated with 1 mL of 100 mM sucrose containing all the transcription components to be loaded into the GUV depending on the experiment for 1 h at room temperature, allowing for GUV formation. After that, the chamber was inverted for 5 min, gently taped twice using a pipette tip and the GUVs were harvested into a 1.5 mL Eppendorf tube and left to settle for 30 min. For the washing, 350 µL of GUVs was taken from the bottom and added to 1 mL of 150 mM glucose buffer. The GUVs were allowed to settle overnight at 4 °C. The next day morning, the top 1 mL of the buffer was removed without disturbing the bottom layer. The GUVs were washed second time with 0.5 mL of 150 mM glucose buffer and the GUVs were only allowed to settle for 2 to 3 h at 4 °C. For subsequent experiments, the GUV solution was sourced from the bottom, where there was a higher likelihood of obtaining GUVs with effectively encapsulated DNA templates and RNA polymerase, attributable to their greater density. All experiments were performed using nuclease-free water. For imaging, an 18-well Ibidi glass bottom chamber was pre-incubated with 3% BSA solution and washed with nuclease-free water twice before GUV addition.

3.3.5 Segregation of DNA droplet

Enzymatic degradation of DNA-RNA strands

RNase A purchased from Promega (WI, USA) was dissolved in deionized water and added to the concentrated DNA droplet solution at a final concentration of 20 µg mL^{-1}. The samples were then imaged after a minimum incubation of 15 min in bulk or in water-in-oil droplets.

Light-triggered DNA cleavage

The sample containing DNA droplets was put onto the observation chamber. The light-triggered cleavage was either achieved by incubation for 5 min under a UV lamp (Hamamatsu) equipped with a 365 nm filter or local illumination using the laser of the confocal laser scanning microscope at a wavelength of 405 nm and a power of 5 mW for at least 30 s.

3.3.6 Expression of RNA origami in GUVs

Expression triggered by Mg^{2+} in GUVs

GUVs containing a mixture of the DNA template (4 ng µL^{-1}), RNA polymerase (0.2 U µL^{-1}), each rNTP (1 mM), $Mg(OAc)_2$ (1 mM), NaOAc (40 mM), KCl (40 mM), Tris-OAc (pH 7.8, 50 mM), DTT (1 mM), DFHBI-1T dye (62.5 µM) and sucrose (150 mM) were formed as described. Subsequently, a specific washing protocol was employed, wherein 350 µL of GUVs were rinsed once with 1 mL of 570 mM glucose buffer, maintained at room temperature for 2 to 3 h. On the same day, 100 µL of the washed GUV solution was transferred to an 18-well imaging chamber and supplemented with 10 mM Magnesium-Ionophore I (Merck). Once the sample was placed on the confocal microscope with an incubation chamber held at 37 °C for 2 h. Following this incubation, an additional 5 mM of $Mg(OAc)_2$ was introduced into the GUV solution. The GUVs were continuously monitored for up to 4 h.

Expression triggered by rNTPs in GUVs

GUVs containing a mixture of the DNA template (4 ng µL^{-1}), RNA polymerase (0.2 U µL^{-1}), α-hemolysin (15 ng µL^{-1}) were formed as described. On the following day, 80 µL of purified GUVs were supplemented with a feeding solution containing

$Mg(OAc)_2$ (6 mM), NaOAc (40 mM), KCl (40 mM), Tris-OAc (pH 7.8, 50 mM), DTT (1 mM) and DFHBI-1T dye (62.5 µM). These components could enter the GUV lumen via the α-hemolysin pores. The GUVs, now containing the necessary components for co-transcriptional folding except rNTPs, were incubated for 2 h at 37 °C. They were then transferred to an 18-well imaging chamber and allowed to settle to the bottom of the slide for 20 min before imaging commenced. Once the sample was placed on the confocal microscope with an incubation chamber held at 37 °C, rNTPs were added externally to achieve a final concentration of 1 mM for each nucleotide. The rNTPs also translocate into the GUVs via α-hemolysin. GUVs were monitored over a period of up to four hours. Alternatively, to image the formation of the RNA origami cytoskeleton-like at discrete time points (0 h, 2 h, 4 h, and 6 h), GUVs were incubated with all above mentioned components including rNTPs in an Eppendorf tube within a thermal block set to 37 °C prior to imaging.

GUV deformation

For all the deformation characterization, GUVs were encapsulated with DNA template (4 -8 ng μL^{-1}) with or without biotin aptamer, RNA polymerase (0.2 - 1 U μL^{-1}), α-hemolysin (15 ng µL) and sucrose (200 mM). The GUVs were washed twice as mentioned above using a glucose solution (250 mM). On the next day, 80 µL of purified GUVs were supplemented with a feeding solution, either containing a homemade buffer consisting of $Mg(OAc)_2$ (6 mM), NaOAc (40 mM), KCl (40 mM), Tris-OAc (pH 7.8, 50 mM), DTT (1 mM) or a commercial 1x transcription buffer from Thermo Scientific (Catlog number EP0112) and DFHBI-1T dye (62.5 µM). To initiate the transcription process, GUVs were incubated for 6 - 12 h with 4 mM rNTPs in an Eppendorf tube within a thermal block set to 37 °C prior to imaging. For the control experiment, the same setup was used without the addition of rNTPs.

3.3.7 Simulation methods

Lattice-based model and numerical simulation

The DNA segregation model is revisited by numerical simulation in both bulk and confinement conditions. The bulk condition in simulation is realized by a periodic boundary, where the DNA motifs can exit from one side of the boundary and re-enter from the other side vertically and horizontally. Whereas in the confinement condition, the DNA motifs can not pass through the boundary to re-enter, rather, they get obstructed by the rigid boundary and can only get reflected back to the system. The dynamic Monte Carlo simulation is run on a lattice system of dimension 100x100. The dynamics starts from a random initial configuration with same density of 0.019 for the three types of DNA populations: blue, green (two DNA motifs) and gray (linker DNA motif). A single Monte Carlo step (MCS) is defined as: when on average each DNA motif is attempted to move to any of the four directions with equal probability as a diffusion process and attempted to rotate in either direction clockwise or anti-clockwise with equal probability as a rotational diffusion process. A single run of the simulations contains maximum of 10^9 MCS. The significant effect of rotation in terms of altering interaction energy only applies for gray linking DNA motifs before cleaving and ”L”-shaped motifs after cleaving, apparently, the green and blue DNA motifs do not rotate. Movements and rotations take place using standard Metropolis algorithm, which involves change in interaction energy ΔE and the explicit temperature T of the system. The interaction strengths (E_{intra} and E_{inter}) are defined with respect to k_BT and the Boltzmann constant (k_B) is taken as unity. As T increases, the system is more likely to be randomized by thermal moves. Before cleaving, we took $T = 0.55$, and after the cleaving, we increased it to 0.70, whereas the attractive interactions E_{inter} and E_{intra} were varied in the range of 0.2 to 3.0 to observe various regimes of the segregation process. To quantify the segregation process, we used the average number of neighboring sites (N) of the other population for a single DNA motif as a function of simulation time for fixed parameters such as interaction strengths and temperature as shown in Fig. 4.4c. Each motif in the simulations has four ends and can interact with up to four other motifs (which would contribute to system’s energy). However, to quantify segregation in the manner similar to Pearson coefficient, we wanted to evaluate the correlations of motifs of different species. Therefore, when counting the neighbors of different species, we also include the four diagonal neighbors that can be occupied by the ”L”-shaped particles in the geometrical vicinity but do not contribute to the interaction energy. Therefore, for the calculation of N, the maximum possible value of neighbors of other species is equal to 8 (and includes both cross motifs and ”L”-shaped particles). To view the dependence of N on interaction strengths, we measured N as an ensemble average over 10^3 simulations with different initial configurations with each run for 10^9 MCS as displayed in Fig. 4.7c. When E_{inter} is high, similar DNA motifs are more prone to form rigid cluster, subsequently decreases the value of N. In contrast to that when E_{inter} is low, the system appears to be in a mixed state of two DNA population, giving rise to higher number of N. For a specific value of $p(= \frac{E_{\text{intra}}}{E_{\text{inter}}})$, the simulation qualitatively recapitulates the experimental observations (Fig. 4.7c). The numerical simulations were conducted using the code provided. We used Intel C-compiler to process the code.

oxRNA simulations

Coarse-grained modeling of individual RNA tiles and the nanotubes was performed using the oxRNA2 force field [232, 233] with the CUDA-accelerated oxDNA molecular dynamics (MD) simulation engine (version 3.5.2) [234–236]. Structures were exported from ROAD schematics to PDB format using the RNAbuild script from ROAD [89]. The PDB structures were then converted to oxDNA simulation files using a local copy of TacoxDNA updated to work with Python 3.11 [237] (pipeline script in Code availability). Structures were relaxed using the protocol detailed in [238, 239]. Briefly, a short Monte-Carlo simulation was performed to remove excluded volume clashes between nucleotides, followed by a longer (at least 5e7 steps, $dt = 0.003$) MD relaxation performed using the “Langevin” thermostat and a modified backbone FENE potential to avoid numerical instabilities due to high forces. Harmonic traps (stiff = 3.1) were placed between all paired nucleotides to maintain the structure during relaxation. Successful relaxation was verified by observing per-nucleotide energy values below -1.4 and visualization of the intended structure with oxView [239, 240].

Multiple production equilibrium MD runs were performed on NVIDIA a100 GPUs using edge-based calculation parallelization [235] for 1e9 simulation steps at $dt = 0.003$. This roughly corresponds to a timestep of 9.09 fs and a total simulation time of 9.09 µs by direct unit conversion. It should be noted, however, that calculating exact time correspondence in coarse-grained simulations is not straightforward. Based on a comparison between DNA binding rates in experiments and oxDNA simulations (see the SI of [241]), the time represented by these simulations may be closer to 30 ms. The temperature was maintained at 37 °C using an Andersen-like thermostat (thermostat = "brownian" or "john" in the oxDNA parameter file) [242]. Debye-Huckel electrostatics were applied to the system mimicking 0.5 M NaCl [233]. Configurations were saved every 5e5 steps, resulting in trajectories with 2000 frames each for analysis. Since the dynamics of correctly folded structures are of interest, we ran multiple simulations and selected the first four simulations where the internal kissing loops maintained a minimum of 11 out of designed 12 bonds on average throughout the simulation for further analysis.

The mean structures, RMSFs, and bond occupancies were calculated from simulation trajectories using oxDNA Analysis Tools (OAT, version 2.3.5) [240]. The structure closest to the mean structure was extracted from one replicate for each structure using the centroid function in OAT and this structure used to build the nanotube simulations using a custom-written Python script (See Code availability), we built 100-layer (300 tiles, ~90,000 nucleotides) simulations from each single tile. The nanotubes were then relaxed with externally-applied harmonic traps to ensure that the kissing loop cohesion was successfully formed. Once over 90% of target bonds were formed, the forces were dropped and triplicate production simulations with the same parameters as the single tiles were performed.

3.3.8 Analysis

Image processing of DNA droplets

All microscope images were processed using ImageJ (NIH, brightness and contrast adjusted). For images in Fig. 4.4a, background pixels were removed using Remove Outliers function of ImageJ (radius: 2, threshold: 10). For DNA segregation in bulk, an image was split into 16 equal regions and processed individually. For DNA segregation in water-in-oil droplets, each water-in-oil droplet was processed individually. The water and oil interface was defined manually and all pixels outside water-in-oil droplet were removed. Except for experiments in water-in-oil droplets, if a z-stack of the sample was imaged, each slice was processed separately. In the case of DNA segregation in GUVs, pixels from region outside the GUV and artefacts (signal from DNA droplets in solution outside of GUV) were removed. A Gaussian blur with a sigma of 2 was then applied on each region of interest. Images were then saved in TIFF files for further analysis.

Pearson correlation coefficient analysis

The Pearson correlation coefficient R_r was calculated using the formula:

$$R_r = \frac{\sum(G_i - \overline{G})(B_i - \overline{B})}{\sqrt{\sum(G_i - \overline{G})^2 \sum(B_i - \overline{B})^2}} \in [-1, 1] \tag{3.1}$$

where G_i or B_i is the intensity of the i$^{\text{th}}$ pixel in the green or blue channel respectively; $\overline{G}$ and $\overline{B}$ are the mean values of all pixel intensities of each channel. Images were analyzed using MATLAB ver. R2018b. Plot graphing and statistical tests were performed using GraphPad Prism.

Analysis of RNA origami expression in GUV

To quantify the fluorescence intensity within GUVs where transcription was triggered with Mg^{2+} or rNTPs (as shown in Chapter 5), GUVs were selected using the DiD channel ($\lambda_{ex} = 640\,\mathrm{nm}$, $\lambda_{em} = 665\,\mathrm{nm}$). The fluorescence intensity was then analyzed in the DFHBI-1T channel ($\lambda_{ex} = 488\,\mathrm{nm}$, $\lambda_{em} = 505\,\mathrm{nm}$). A region of interest (ROI) for each GUV was delineated with a circular mask on an 8-bit grayscale image using Image J (1.53v). To analyse the transcription trigger over time, the same GUV timeline image was used at 2 min interval up to 3 h to 4 h. The mean intensity values obtained for each GUV were obtained by using Measure function and presented as fluorescence intensity across the samples.

Analysis of RNA origami nanotube growth

Images of nanotube-producing GUVs at different time points were analysed in ImageJ2 (ImageJ2 2.14.0/1.54f [243]) using custom-written ImageJ macro scripts (See Code availability). In summary, for time point t = 0 h, the GUVs were automatically detected using the Hough Circle Transform plugin. For further time points, the GUVs which produced RNA nanotubes were manually chosen. The regions of interest (ROI) in the RNA fluorescence channel were then filtered and threshold using the Gaussian Blur, Convert to Mask and Erode functions. The area fraction was then extracted for each GUV using the Measure function. For time point 0, false detections were manually removed. For other time points, only GUVs containing more than 1% area fraction were taken into account.

Persistence length analysis

All AFM images were pre-processed with the open-access software Gwyddion [244] using standardized Align Rows and Levelling tools, then exported into Tagged Image File Format (TIFF). The nanotubes were manually masked using Object Selection Tool and other Selection Tools in Adobe Photoshop 2024 version 25.12.0. The background was then removed and exported as a TIFF file. Due to branching of the nanotubes, the background-removed images were then traced using using a custom-written Python script (See Code availability) which skeletonize the preselected nanotubes and traced along the longest path in case of branching.

The extracted coordinates were then used as input for a custom-written Python script (See Code availability) to calculate the persistence length of the *in vitro* transcribed nanotubes. To reduce detection error due to low resolution in imaging, the data was filtered to exclude all detection under 200 nm. The squared end-to-end distance of each nanotube was plotted against its contour length. The data was then fit using the theoretical relation:

$$\langle R^2 \rangle_{3D} = 2sPL\left(1 - \frac{sP}{L}(1 - e^{-L/sP})\right) \tag{3.2}$$

where R^2 is the squared end-to-end distance, L is the contour length, P is the persistence length and s is a surface parameter that is set to 1. For each nanotube, the end-to-end distance and the total contour length of the nanotube was extracted for fitting. The data was masked by residuals ±1 standard deviation. For the simulated structures, due to the narrow distribution of contour length (as to the simulation is only one nanotube over time), one persistence length is calculated for each frame. The end-to-end distance of every layer pair and their contour lengths were fitted using the same equation and masking as described above. The data plotted in Fig. 5.12g is the last 10% of the simulation frames ($t \geq 9\text{e}8$).

Analysis of RNA cytoskeleton attachment to GUV membranes

Images of single GUVs that produced RNA cytoskeleton with and without biotin aptamer were analysed in ImageJ2 (ImageJ2 2.14.0/1.54f) using custom-written ImageJ macro scripts (See Code availability). The GUVs were automatically detected using the Analyze Particles method. In short, the lipid fluorescence channel was processed using the Auto Threshold, Fill Holes, Erode, Gaussian Blur then Convert to Mask functions prior to particle analysis. The detected ROIs were then manually filtered to remove false detection of non-GUV particles. The radial profile of each selected ROI was extracted using the Radial Profile function. The origin of the radial profile was the measured centroid of the ROI. The radius is the primary axis of a fitted ellipse to the ROI.

The radial profile was then analyzed and plotted using a custom-written Python script (See Code availability). The center of mass of the RNA fluorescence relative to the GUV center was calculated for each GUV using the formula:

$$x_c = \frac{\sum_{i=1}^{N} x_i y_i}{\sum_{i=1}^{N} y_i} \tag{3.3}$$

where x_c is the center of mass of the radial fluorescence, x_i are the normalized distance from the center of the GUV, y_i is the normalized RNA radial fluorescence at distance x_i, and N is the number of x, y pairs.

Analysis of deformation of GUVs due to RNA nanotubes

Membrane detection and angular RNA origami nanotube intensity measurements were carried out with a custom written ImageJ macro using ImageJ2 Version

2.14.0/1.54f and afterwards analysed and plotted using a Jupyter Notebook (Python 3.10.13) (See Code availability). For membrane detection, the membrane channel of the confocal microscopy images was processed using Gaussian blur with $\sigma = 3$ and auto-thresholded using the Li method. The Convert to mask, Fill holes, Erode, and Analyze particle functions were then applied to obtain a ROI. The binary ROI image was saved in the output folder and the centroid coordinates of the ROI calculated. The ROI images were then used to measure circularity using the ImageJ Measure function (set for Shape descriptors) where the circularity was defined as:

$$R = \frac{4 \cdot \pi \cdot A}{P^2} \tag{3.4}$$

Where A is the area of the ROI and P is the perimeter of the ROI. For the GUVs where a z-stack was acquired, only the mean circularity was reported in Fig. 5.29g.

The distance for each coordinate in the ROI after membrane detection to the centroid is calculated and saved in a result file. In order to detect the RNA origami nanotubes, a second, rectangular ROI was drawn from the centroid towards the membrane with a length equal to 80% of the distance between the centroid and the membrane. The rectangular ROI was drawn for every 10th point on the membrane and the rectangle width was set to 3 µm. The mean intensity for each rectangle was measured and saved in another file. The Jupyter notebook script was then used to load the data from the two files and extract and plot the radii and intensities.

Data visualization and analysis

Plot graphing and statistical tests were performed using GraphPad Prism (Version 5 and Version 10.2.3) and Matplotlib 3.9.0.

3.3.9 Code availability

All custom written code was deposited on GitHub at:
`https://github.com/Biophysical-Engineering-Group/RNAcytoskeleton`.

3.3.10 Statistics and Reproducibility

Unless mentioned otherwise, brightness and contrast were adjusted for all confocal microscope images. To extract the Peason R_r values, confocal images were pre-processed by introducing a Gaussian blur. If not stated otherwise, all data is presented as mean ± standard deviation. The sample sizes (n) are explicitly stated in the figure captions. All attempts to reproduce the data have been successful. For the statistical analysis in Fig. 4.16, $n = 71$ DNA droplets were manually picked for diameter measurements from ≥ 15 water-in-oil droplets with ≥ 3 DNA droplets per water-in-oil droplet (a: 17, b: 15, c: 20, d: 16 water-in-oil droplets analyzed). A parametric, unpaired t test with Welch's correction was performed to compare condition a to each of the other condition. Two-tailed P values of the comparison between condition a and b, and a and d are both ¡0.0001. Two-tailed P value of the comparison between condition a and c yields 0.1277. Statistical analysis, non-linear regression and data plotting were performed using GraphPad Prism 8.3.0. Statistical analyses were conducted using a parametric, unpaired t-test with Welch's correction. Data are presented as the mean ± s.d. from at least $6 - 78$ GUVs observed with confocal microscopy, depending on the specific experimental conditions. For visualization, data in Fig. 5.2g,h was all plotted to 174 minute. Persistence length values are presented as fitted value ± error of fit. Persistence length analysis was performed solely on co-transcribed nanotubes that were longer than 200 nm. Persistence length analysis was done on the middle 80% layer of each simulated nanotube with overhangs excluded from the analysis. Confocal and AFM experiments were each performed with more than six and two independent biological replicates, respectively. For plate reader assays, measurements were conducted in independent triplicates. Simulation data was generated from three independent runs. Only simulations of single tile where the internal kissing loops contain more than 11 out of 12 base pairings were used for further *in silico* assembly and analyses. All analyses of nanotubes inside GUVs were conducted only on GUVs containing nanotubes. Empty GUVs were excluded from the analysis. No statistical method was used to predetermine sample size. The experiments were not randomized. The Investigators were not blinded to allocation during experiments and outcome assessment.

Science is as far as we know it.

4
DNA Segregation Modules

Author Contributions and Reuse Statement

This chapter includes material adapted from:
Mai P Tran, Rakesh Chatterjee, Yannik Dreher, Julius Fichtler, Kevin Jahnke, Lennart Hilbert, Vasily Zaburdaev, Kerstin Göpfrich; 'A DNA segregation module for synthetic cells', *Small* (2022) `https://doi.org/10.1002/smll.202202711`
This chapter, including figures and text, are excerpts from the aforementioned publication. These materials are reused in accordance with Creative Commons CC-BY. No individual citations are provided within this chapter for the reused content. All reused material has been integrated into the flowing narrative of this thesis and re-contextualized where necessary.
I did all the experiments and analyses presented in this chapter, except for the lattice-based modeling and its analysis. All co-authors provided feedback on experimental results and contributed to manuscript revisions. The final texts reflect a collaborative effort.

4.1 DNA segregation strategy

To build our synthetic DNA segregation module, we first need to assemble DNA coacervate droplets that are capable of undergoing fission. We adapted a design based on two types of DNA Y-motifs (Fig. 4.1a, blue and green), whereby each Y-motif is formed from three single-strands of DNA which self-assemble into a Y-shaped motif (each arm containing 18 base pairs plus 8 base pair long sticky ends, corresponding to approximately 6 nm plus 3 nm) [173]. The Y-motifs possess two orthogonal types of palindromic eight nucleotide long sticky end sequences which allow for their polymerization among the same population (blue-blue, green-green). The two populations of Y-motifs are inter-connected by a six-arm linking motif, such that a single coacervate droplet forms (containing the blue and green Y-motifs as well as the linking motif, see Experimental Section). The cleavage of the linking motifs removes the interactions between the two DNA Y-motif populations, leading to their segregation into two separate liquid phases. Once the segregation process is completed, the daughter DNA droplets are spatially segregated due to the sequence-orthogonality of their interactions (Fig. 4.1a) [173].

For the cleavage of the linking motifs, we implemented two different strategies, namely, enzymatic cleavage and light-triggered cleavage (Fig. 4.1b,c). Light-triggered cleavage allows for full spatiotemporal control over the segregation process, in particular within compartments. For enzymatic cleavage, as demonstrated by Sato et al. [173], ten DNA bases were replaced with RNA in two opposite strands at the centre of the six-arm linking DNA motif. We can therefore make use of RNase A activity to degrade the RNA-DNA hybrid strands and hence the connection between the two halves of the six-arm motif [173]. In this way, the connection between the two populations of the Y-motifs is disrupted.

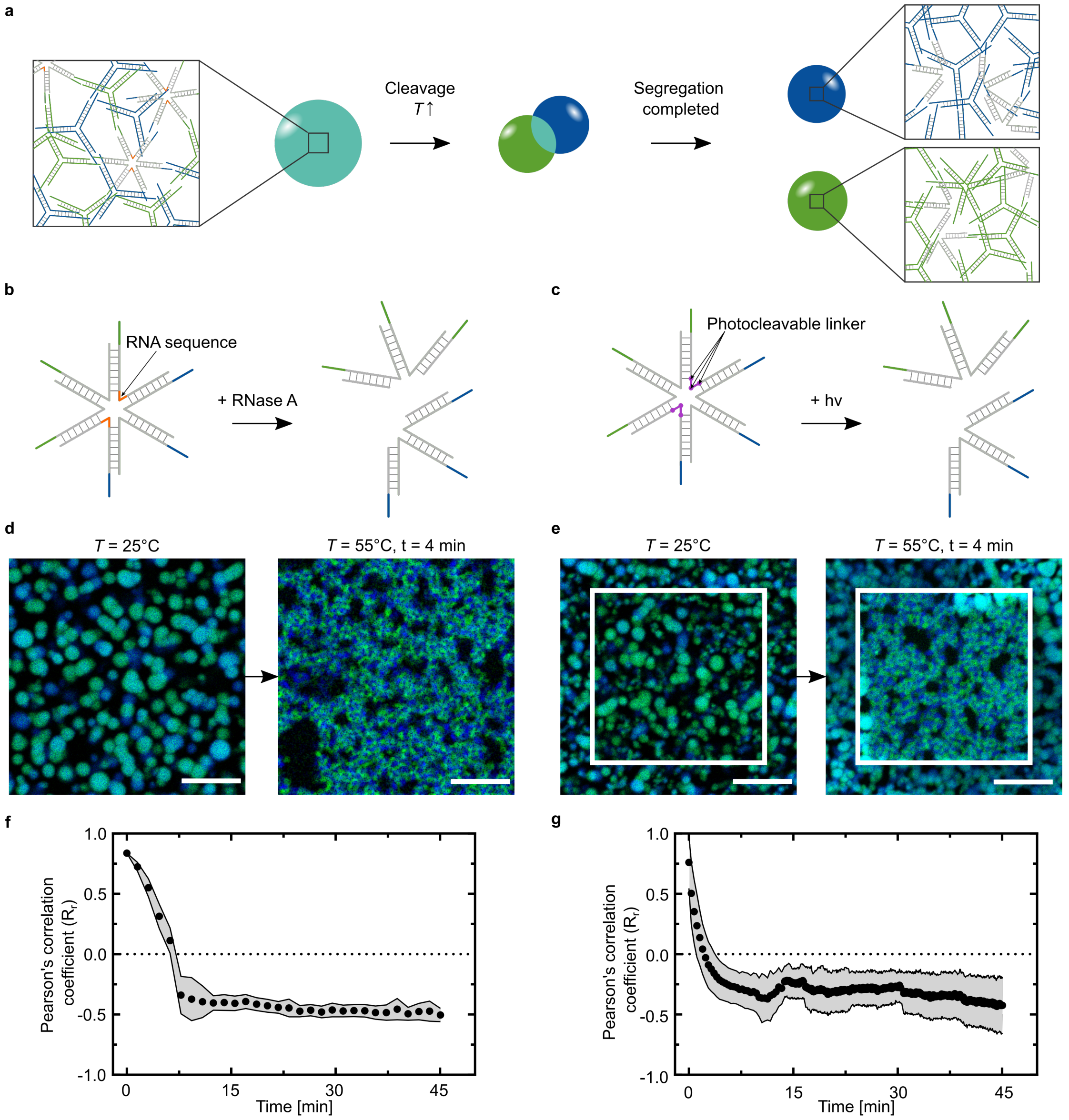

Figure 4.1: DNA segregation mechanism by enzymatic or photo-induced cleavage. a) Schematic of the DNA droplet consisting of two types of DNA Y-motifs (green and blue) with self-complementary sticky end sequences. A six-arm DNA motif interconnects the two populations to form a single droplet. Upon cleavage of the six-arm linking star and sufficient temperature increase, the initial droplet (cyan sphere) liquid-liquid phase separates into two segregated droplet populations (green and blue). b,c) Cleavage of the gray six-arm linking motif is achieved by enzymatic activity of ribonuclease A (RNase A) (b) or by light-triggered photocleavage of nitrobenzyle groups (c). d) Confocal overlay images of DNA droplets pre-treated with RNase A in bulk ($c = 20\,\mu g\,mL^{-1}$) before (left) and after heating to $T = 55\,°C$ for $t = 4\,min$ (right). (continued on the following page)

Figure 4.1: (continued) e) Confocal overlay images of DNA droplets in bulk before (left) and after heating (right). The droplets within the region of interest (highlighted with a white square) were illuminated at $\lambda = 405\,\text{nm}$ for $t = 30\,\text{s}$ to induce photocleavage. The two DNA populations were labeled with ATTO-488 ($\lambda_{ex} = 488\,\text{nm}$) and ATTO-647N ($\lambda_{ex} = 640\,\text{nm}$). Scale bars: 20 µm.
f,g) DNA segregation dynamics of the RNase A-cleaved DNA droplets (f) and the photocleaved DNA droplets (g). Colocalization analysis (Pearson's correlation) was performed and Pearson's R_r values are plotted over time (mean ± s.d, $n = 16$ regions in (f) and $n \geq 64$ regions in (g)).

To enable photoinduced segregation, three photoreactive nitrobenzyle linkers were introduced within the same two strands of the six-arm motif that were modified for enzymatic cleavage (Fig. 4.1c). The three photocleavable groups were positioned such that two five nucleotide long DNA oligos are released upon illumination and the six-arm motif splits into two.

We first tested these two DNA droplet segregation methods in bulk. After treatment with RNase A and heating to 55 °C to bring the DNA droplets to the liquid state, the DNA droplets undergo segregation in the entire observation chamber (Fig. 4.1d). Despite activity of RNase A within a broad temperature range from 15 − 70 °C,[245] enzymatic activity cannot be spatially controlled in the bulk sample. Photocleavage, instead, could be triggered locally by illumination with the 405 nm laser of the confocal microscope. DNA droplets in the illuminated area (highlighted by the white box in Fig. 4.1e) undergo segregation, while adjacent droplets only fuse due to the heating. A line profile shows the complete spatial segregation at droplet level at the 15 min time point for both systems (Fig. 4.2).

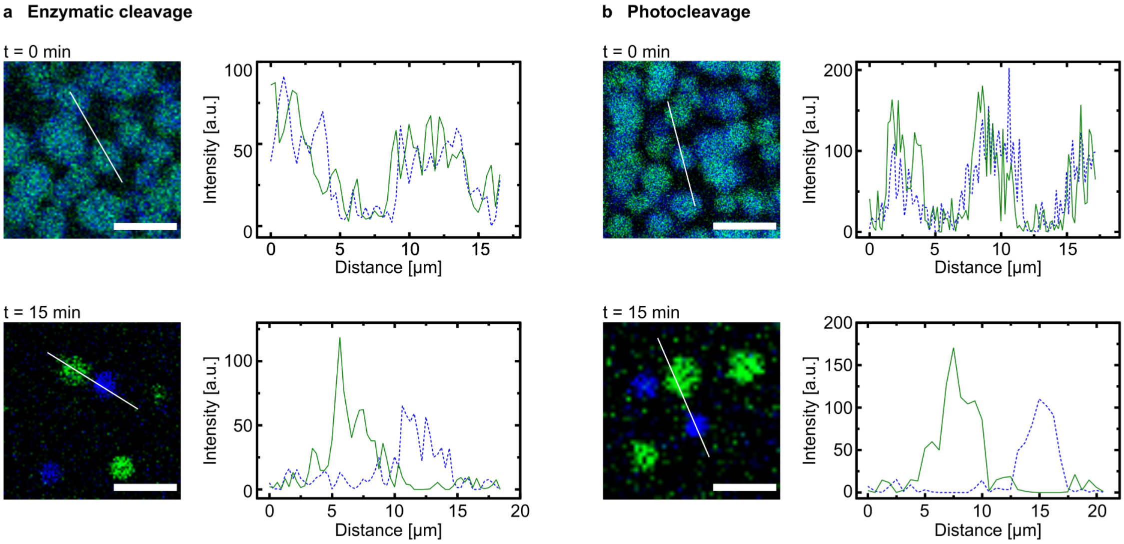

Figure 4.2: Spatial segregation of DNA droplets in bulk. Confocal microscopy overlay images of cleaved DNA droplets using (a) enzyme- or (b) light-induced cleavage at two time points of incubation at 55 °C (0 min and 15 min). The intensity profiles of the fluorescence signal of the two populations along the white line are shown next to the corresponding image (green population: green line; blue population: blue dashed line). The two DNA populations were labeled with ATTO-488 (λ_{ex} = 488 nm) and ATTO-647N (λ_{ex} = 640 nm). Scale bars: 10 μm.

To describe the segregation kinetics in a quantitative manner, we determined Pearson's R_r correlation coefficient as a measure for the colocalization of the two Y-motif populations over time. Note that a value of R_r = +1 corresponds to perfect colocalization whereas R_r = -1 is obtained for perfectly anti-correlated data. The correlation coefficient decays and reaches a plateau within less than 10 min for both the enzymatic and the light-triggered DNA droplet segregation (Fig. 4.1f,g). However, the decay kinetics differ for the two systems. Interestingly, we observed a latency for the enzymatic segregation (Fig. 4.1f), while the photoinduced segregation follows an exponential decay (Fig. 4.1g). This behaviour is consistent at different temperatures (Fig. 4.3b-iii,iv).

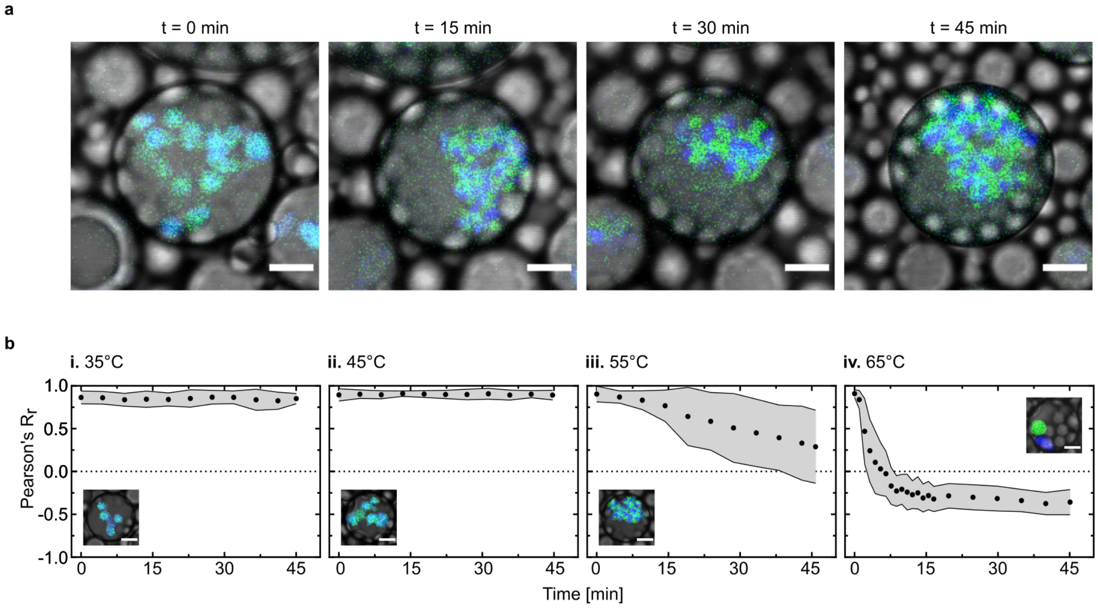

Figure 4.3: Enzyme-induced segregation of DNA droplets in water-in-oil droplets. a) Time series of DNA droplet segregation triggered by enzymatic activity of RNase A in a water-in-oil droplet (fluorescence and brightfield overlay). The two DNA populations were labeled with ATTO-488 ($\lambda_{ex} = 488\,\mathrm{nm}$) and ATTO-647N ($\lambda_{ex} = 640\,\mathrm{nm}$). b) The enzymatic segregation process is observed over time in water-in-oil droplets at different temperatures (**i-iv**) ($t = 45\,\mathrm{min}$, $T = 35-65\,°\mathrm{C}$, $10\,°\mathrm{C}$ step) and colocalization values (Pearson's R_r) are plotted (mean ± s.d, $n > 60$ water-in-oil droplets). Insets: Overlay of confocal fluorescence and brightfield images of representative water-in-oil droplets in each condition. The fluorescent pixels outside of the DNA droplets are removed for visibility. Scale bars: 10 µm.

Light can penetrate across the entire droplet and cleave all linking DNA motifs simultaneously, while enzymatic activity is initially limited to the surface of DNA droplets in a gel state due to the size exclusion [246]. Once the DNA droplet is in a liquid state, enzymes can have access to the rest of the droplet. This ongoing enzymatic reaction delays the segregation process, explaining the delayed decay of the Pearson's correlation coefficient for the enzymatic cleavage.

We have thus demonstrated enzymatic and photoinduced cleavage as two distinct mechanisms for the segregation of densely packed droplets of DNA Y-motifs, whereby photo-cleavage provides full spatiotemporal control. We will therefore use the light-triggered segregation for the following experiments.

4.2 DNA segregation in cell-sized confinement

Having demonstrated DNA segregation in bulk, we next introduced geometric confinement by encapsulating the DNA droplets into cell-sized compartments. For this purpose, we encapsulated the DNA droplets in water-in-oil droplets and carried out the experiment analogous to the bulk segregation. Importantly, we find that the confinement slows down the segregation kinetics (Fig. 4.4a). Tracing the colocalization of the two populations over time shows full segregation in bulk after 10 min while the segregation process is still not fully completed after 45 min in confinement (see graph in Fig. 4.4a). This result is consistent for both enzyme- and photo-induced segregation (Fig. 4.4a, Fig. 4.4f, Fig. 4.3a,b-iii).

To shed light on the possible mechanism and to confirm that the geometric confinement indeed can slow down segregation of DNA droplets, we considered a lattice-based model of this process. The model describes each DNA Y-motif as a cross-shaped particle diffusing on a two-dimensional (2D) square lattice in the four possible directions (up-down-left-right) with defined particle-particle interaction strengths and excluded volume effects. Systems of cross-like particles on a lattice are a well-studied model of statistical physics [247–250]. At the same time, this model contains the minimal geometry necessary to account for all inter- and intra-species interactions as happening in experiments. Therefore, whilst being simpler than a hexagonal lattice model, the square lattice still captures the experimental system. Analogous to the experiment, the model contains three types of particles, namely two populations which interact amongst themselves (blue and green) and linking particles (analogous to the six-arm DNA motif) which interconnect the two populations. When the linking particles are cleaved, they produce two ”L”-shaped particles of the respective DNA populations (Fig. 4.4b). Both the linking motifs and the cleaved ”L”-shaped motifs can rotate stochastically to maintain the orientational uniformity of the system. The overall surface coverage by the particles is kept below 0.8 to ensure that the system maintains a liquid state [251].

We reproduced the bulk and confinement conditions by using periodic and rigid boundaries, respectively. Starting from a random initial configuration with a given particle density, interaction strengths and system temperature, a mixed phase is produced to mimic the initial mixed DNA droplets as observed in the experiment (Fig. 4.4c). After cleaving the linking motifs, a higher temperature is applied to the mixed phase so that the linking motifs break apart to produce two ”L”-shaped motifs, each belonging to their respective DNA population. Similar to the experiment, we observed phase segregation resulting in two separate droplet species. For the quantitative analysis of the simulations, we introduced a parameter N, which defines, for a single blue or green DNA motif, the average number of nearest neighbor sites occupied by the motifs of the other population (including the diagonal sites that can be occupied by “L”-shaped motifs). This metric is qualitatively equivalent to the Pearson’s correlation coefficient R_r measured in the experiment, whereby higher number of different motif neighbours corresponds to a mixed state while lower number is indicative of segregated droplets. Importantly, in agreement with experimental results, the phase segregation in confinement is slower. The slower

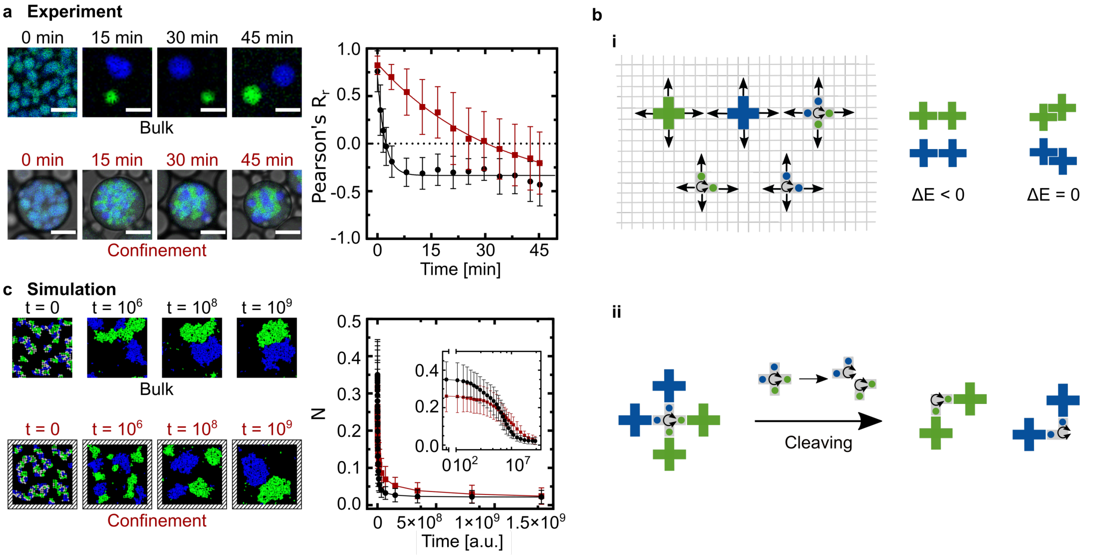

Figure 4.4: Effects of geometrical confinement on DNA segregation dynamics. a) Experimental DNA segregation dynamics in bulk compared to in confinement. Left panel: Representative confocal microscopy images of different time points showing DNA droplet segregation in bulk (upper, fluorescence overlay) and in water-in-oil droplets (lower, fluorescence and brightfield overlay). The two DNA populations were labeled with ATTO-488 ($\lambda_{ex} = 488\,\text{nm}$) and ATTO-647N ($\lambda_{ex} = 640\,\text{nm}$). Scale bars: 10 µm. Right panel: Pearson's R_r values plotted over time for DNA segregation process in bulk (mean ± s.d, $n > 64$ regions, black circles) and in confinement (mean ± s.d, $n > 70$ water-in-oil droplets, red squares). The data is fitted using one-phase decay equation (shown in lines). b) Schematic of implemented lattice-based model. i) Cross-shaped DNA-motifs can perform next nearest neighbor diffusion in four directions, linking (gray) and cleaved "L"-shaped motifs can additionally undergo stochastic rotations. The system free energy is only reduced for arm-to-arm configurations and not affected by any other contact. ii) Cleavage mechanism in the model: A mixed phase is produced from a random initial configuration, and thereafter cleaving of linking motifs give rise to two "L"-shaped motifs. c) Simulated DNA segregation dynamics in bulk compared to that in confinement. Left panel: Snapshots of DNA droplets undergoing segregation with periodic boundary conditions, mimicking experimental bulk condition (upper) and within rigid boundary, mimicking experimental confinement (lower). The simulation time step (t) is indicated above each snapshot. For visibility, the gray particles are colored in the same color as their population (see Fig. 4.5 for original images). Right panel: Average number of nearest neighbors of the other DNA population over time in periodic boundary (mean ± s.d, $n > 10^3$ (ensemble average), black circles and line) and in rigid boundary (mean ± s.d, $n > 10^3$ (ensemble average), red squares and line).

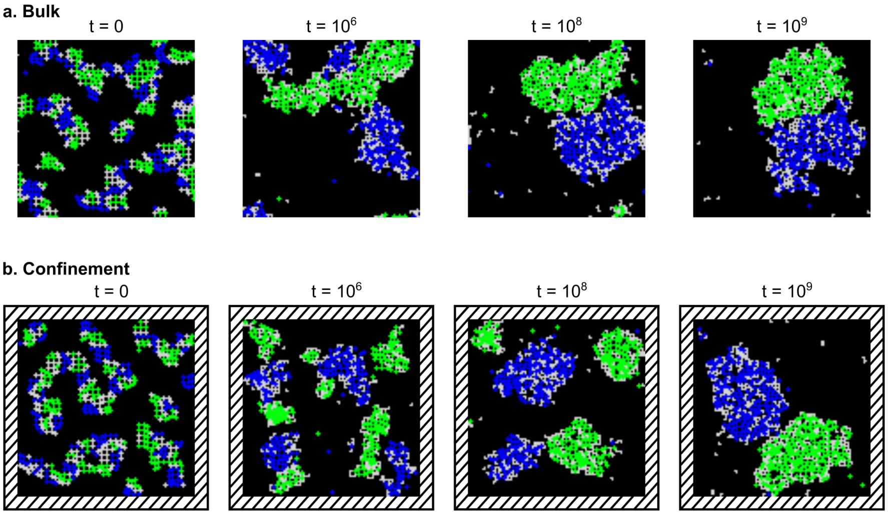

Figure 4.5: Original images of Fig. 4.4c. Snapshots of DNA droplets undergoing segregation with periodic boundary conditions, mimicking experimental bulk condition (a) and within rigid boundary, mimicking experimental confinement (b). The gray particles are set in its original color.

segregation kinetics in confinement are likely due to particles which detach in close proximity to the compartment boundary, which attach back in close proximity to their initial position as confirmed by tracing particle trajectories in the simulations (Fig. 4.6). This slows down the overall reorganization of the DNA droplets. This finding corroborates the role of cell-sized confinement on our DNA segregation process, accentuating the importance of including compartments while studying and constructing cellular components.

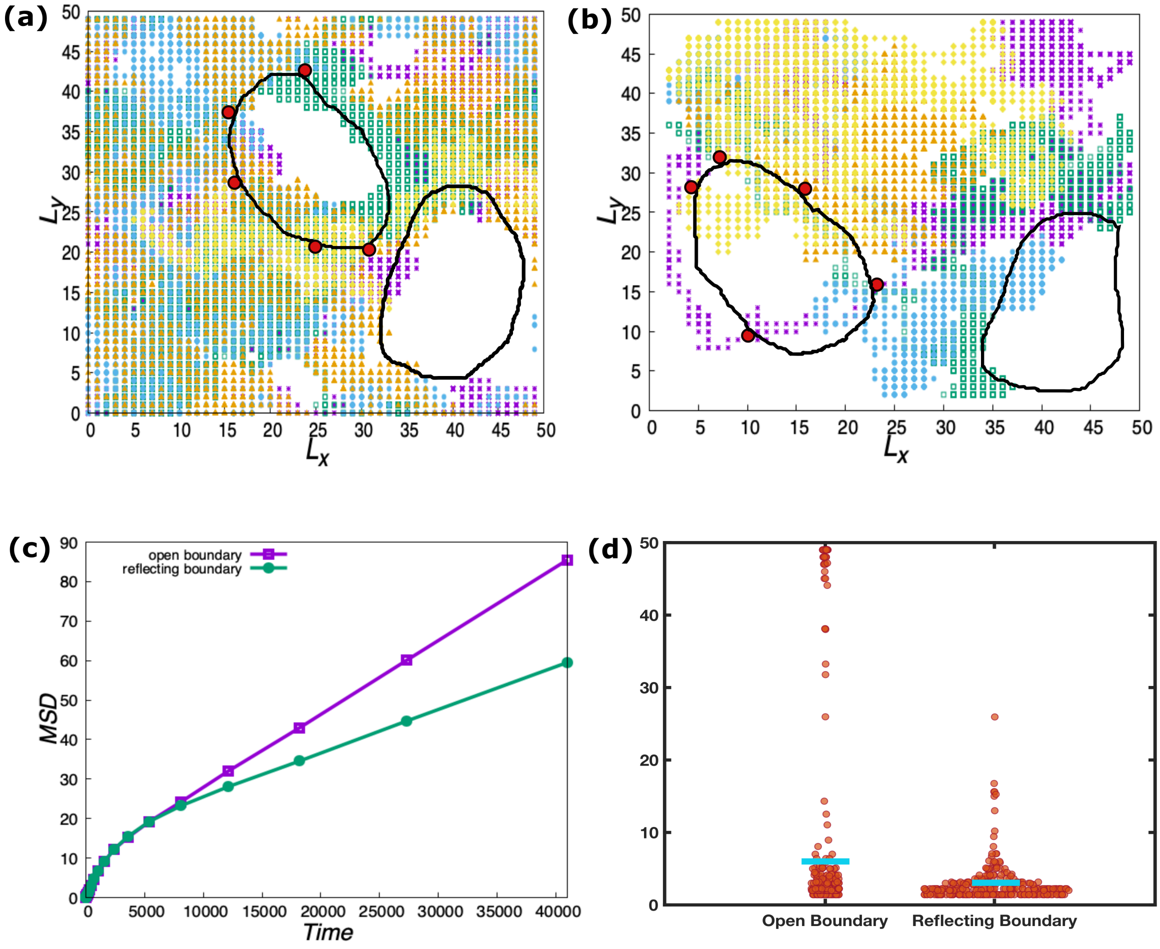

Figure 4.6: Effect of confinement on particle reattachment revealed by single particle tracing. Single tracer particles tracked for 5 different simulated realizations are shown in the top row panels (a) and (b). Tracking is done upon particles' detachment from the cluster (red circles) until their reattachment to the same cluster for periodic boundary (a) and reflecting boundary (b), which mimic the experimental condition in bulk and in confinement, respectively. Initial cluster-boundaries corresponding to two DNA clusters are outlined by black curves. The mean squared displacement (MSD) of the particles is plotted over time (c), showing more rapid growth in periodic boundary due to the faster exploration of the particles for the available lattice space (averaged over 10^4 trajectories). Finally, (d) shows a swarm plot of the return distances (distance between tracer motif detachment point and its re-attachment point to the same cluster) for each motif in the two conditions. The difference in the mean values and the tail distribution in the case of periodic boundary indicates further travelling distance of the particles under bulk condition.

4.3 Control of DNA segregation kinetics

Having demonstrated that DNA segregation is slowed down in confinement, we set out to elucidate mechanisms by which DNA segregation can be sped up and controlled in a compartment. We therefore probed different strategies to tune the interaction strength and the diffusion of the DNA Y-motifs. The most obvious parameter which will influence both, DNA-DNA interaction and diffusion, is temperature. We examined the segregation process at 35 –65 °C which covers the gel to liquid transition of DNA droplets [173]. At 35 °C and 45 °C, the cleaved droplets remain unchanged in both enzymatic and photocleavable systems (Fig. 4.7a-i,ii; Fig. 4.3b-i,ii). Neither fusion nor fission events occurred, indicating that the DNA droplets are in a gel state. When the temperature was raised to 55 °C after incubation at 35 °C or 45 °C, DNA segregation was observed (Fig. 4.8).

A temperature increase from 55 °C to 65 °C significantly speeds up the DNA segregation (Fig. 4.7a-iii,iv, Fig. 4.9-4.10). Complete segregation is detected in nearly all water-in-oil droplets after only 5 min of incubation at 65 °C (Fig. 4.7a-iv), whereas the process was not fully completed at 55 °C even after 45 min (Fig. 4.11).

At 65 °C, we additionally observed partial wetting of the blue DNA population on the water-in-oil interface (Fig. 4.11). Wetting is enabled by the presence of negatively charged Krytox molecules in the surfactant layer [186, 252]. It is interesting that it is only observed for the blue population. This is likely due to its lower unpaired fraction at elevated temperatures as revealed by a comparative analysis of the melting profiles of the two sequences (Fig. 4.12).

Another parameter which has been well-studied to affect DNA diffusion and interaction is the ionic strength of the solution [254, 255]. We thus formed the DNA droplets as previously in 0.35 M NaCl, 1× Tris-EDTA pH 8.0, pelleted and resuspended the droplets in solutions of different ionic strengths prior to encapsulation into water-in-oil droplets (Fig. 4.7b). We then imaged the droplets after photocleavage and 10 min incubation at 55 °C. As the concentrations of NaCl increases from 0.15 M to 1.5 M, the correlation coefficient increases from -0.69 to 0.52, respectively, indicating reduced DNA segregation (Fig. 4.7b). At 2 M and 4 M NaCl, we observed wetting interactions between the blue Y-motifs and the surfactant-stabilized water-oil interface (Fig. 4.7b-i). At high concentrations of monovalent salt, charge screening is effectively leading to an interaction between the DNA and the negatively charged Krytox in the surfactant layer [252]. 10 mM of divalent cations result in similar segregation kinetics to 0.15 M NaCl. Due to the more effective charge screening of divalent cations, more than 10 times lower concentrations are required here.

To investigate how the ionic strength affects specific and unspecific interactions among the Y-motifs, we hypothesize that increasing ionic strength increases the interactions between Y-motifs of the same type as well as the unspecific electrostatic interactions of all Y-motifs. To test this hypothesis, we simulated the DNA segregation process for different inter- and intra-population attractive interaction strengths and assuming that diffusion rate of free particles is not changing. In absence of any known explicit dependence among different interaction strengths in the experiment,

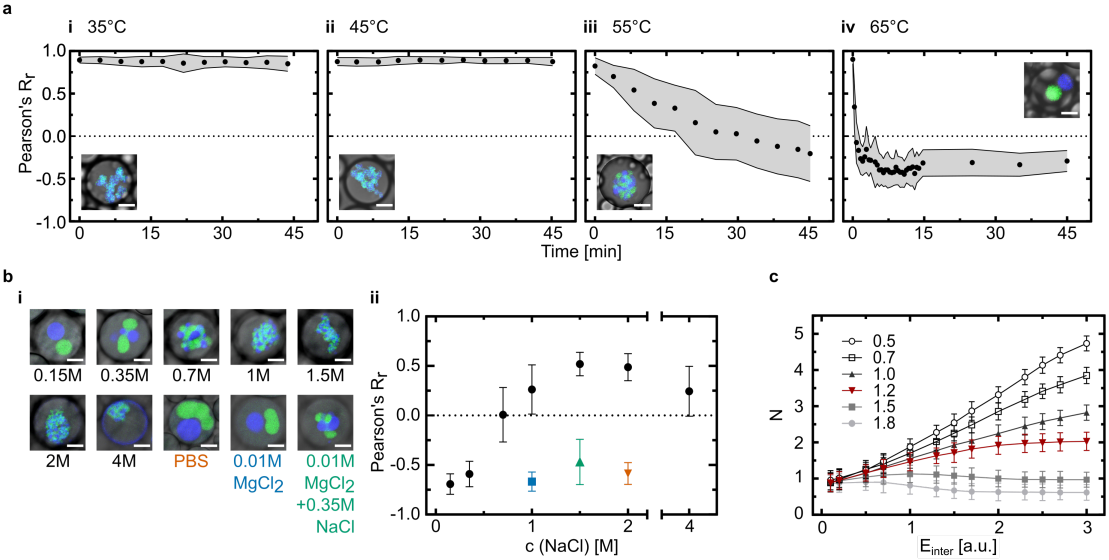

Figure 4.7: DNA segregation dynamics depends on different parameters. a) Temperature dependence. Photo-induced segregation process is observed over time in different water-in-oil droplets at different temperatures (i-iv) ($t = 45\,\text{min}$, $T = 35 - 65\,°\text{C}$, $10\,°\text{C}$ step) and Pearson's R_r values are plotted (mean ± s.d, $n > 60$ water-in-oil droplets). Graph insets: overlay of confocal fluorescence and brightfield images of representative water-in-oil droplets in each condition. The fluorescent pixels outside of the DNA droplets were removed for visibility. b) Ionic strength dependence. i) Overlay of confocal fluorescence and brightfield images of photo-cleaved DNA droplets in water-in-oil droplets after heat treatment ($t = 10\,\text{min}$, $T = 55\,°\text{C}$) at different ionic conditions. ii) Pearson's R_r values of the two DNA populations plotted against NaCl concentrations (black circles) and other ionic conditions in (i) (PBS in orange, 0.01 M $MgCl_2$ in blue and 0.01 M $MgCl_2$ + 0.35 M NaCl in green, mean ± s.d, $n > 70$ water-in-oil droplets). Scale bars: 10 µm c) Lattice simulations: Average number of neighbors N as a function of inter and intra-population strengths for several values of the linear multiplicative constant ($p = \frac{E_{\text{intra}}}{E_{\text{inter}}}$) ranging from 0.5 to 1.8. At the value $p = 1.2$, the curve (red line) is qualitatively similar to the dependence in experiment. Now, for $p < 1.2$, the intra-population interactions dominate and N increases as E_{inter}, leaving the system in a more mixed state, whereas for $p > 1.2$, the system is largely segregated into two DNA populations.

Figure 4.8: DNA droplet segregation after a temperature rise to 55 °C. After photocleavage and incubation for 45 min at either 35 °C (a) or 45 °C (b), the temperature was increased to 55 °C for either 5 min (a) or 7 min (b). Confocal overlay of brightfield and fluorescence channels of a representative water-in-oil droplet for each condition is shown. Scale bars: 20 µm

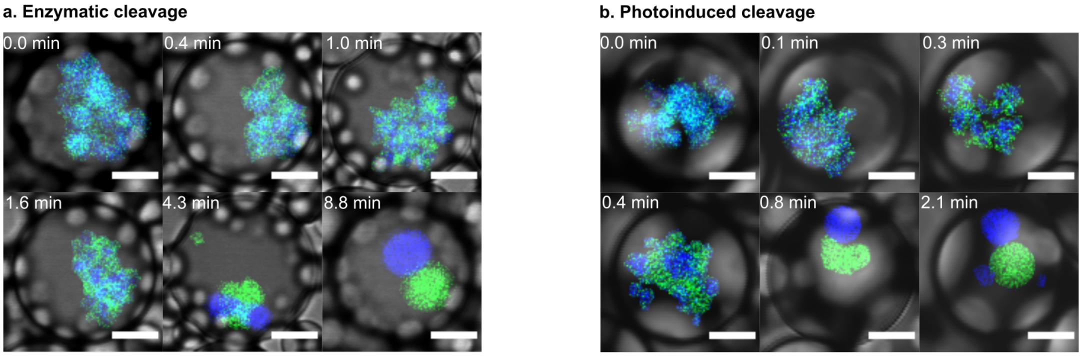

Figure 4.9: Time series of DNA droplet segregation at 65 °C. Representative confocal microscopy images of different time points showing DNA droplet segregation in water-in-oil droplets (fluorescence and brightfield overlay) after enzyme-induced (a) and photoinduced (b) cleavage. The fluorescent pixels outside of the DNA droplets were removed for visibility. The two DNA populations were labeled with ATTO-488 ($\lambda_{ex} = 488\,\mathrm{nm}$) and ATTO-647N ($\lambda_{ex} = 640\,\mathrm{nm}$). Scale bars: 10 µm.

we here assume a linear relation with a multiplicative constant $p = \frac{E_{\mathrm{intra}}}{E_{\mathrm{inter}}}$, where E_{intra} and E_{inter} represent the attractive interaction among similar (intra-population, i.e. green-green, blue-blue) and different (inter-population, i.e. green-blue) types of DNA-motifs, respectively. In the experiment, intra-population interactions are mediated by base-pairing and electrostatic interactions; inter-population interaction is mediated by electrostatics only. The simulation reveals that, depending on the values of p, the behaviour of the segregation process responds differently to varying interaction strengths, as shown in Fig. 4.7c. As p increases, DNA motifs of the same population form relatively robust clusters, reflected in a reduction in N, whereas decreasing p has the opposite effect (Fig. 4.7c). At p=1.2, the curve has qualitatively the same shape as in the experiment. This indicates a possible approximate relation between the two types of interactions (E_{intra} and E_{inter}), whereby the interaction be-

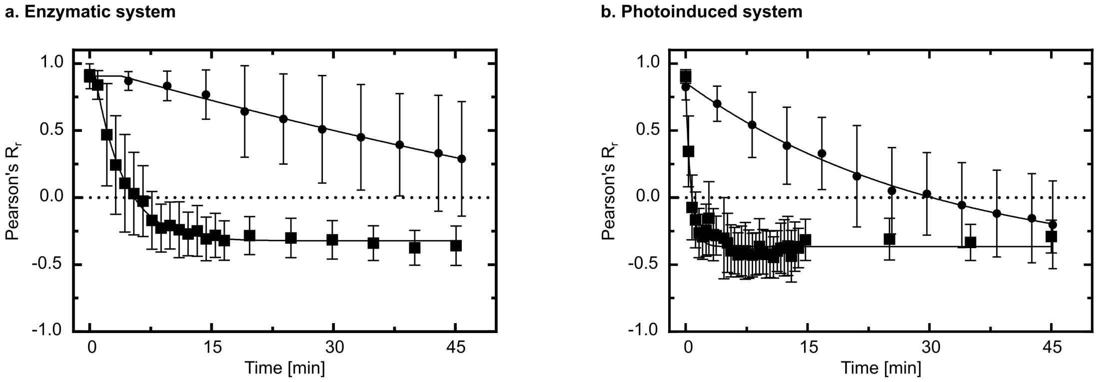

Figure 4.10: Comparison of DNA droplet segregation process at 55 °C and 65 °C. The data has been extracted from Fig. 4.7a and Fig. 4.3b. Pearson's R_r values over time for segregation process at 55 °C (circles) and 65 °C (squares) are fitted by a plateau followed by a one phase decay equation for enzymatic system (a) and by a one phase decay equation for photoinduced system (b). An extra sum-of-squares F test was performed to compare the fitted curves for data collected at 55 °C and at 65 °C (Y0 is shared value for all data sets, K > 0). P values are < 0.0001 for both systems.

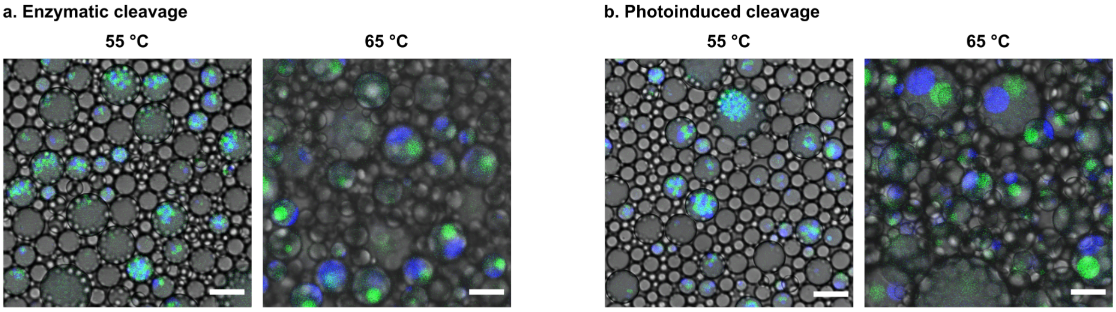

Figure 4.11: Overview of DNA droplet segregation after incubation at 55 °C and 65 °C. Overlay of brightfield and fluorescence confocal images showing DNA droplet segregation in multiple water-in-oil droplets in the same field of view. DNA droplets are cleaved using RNase A (a) or light illumination (b) and incubated for 45 min at 55 °C or 65 °C. The two DNA populations were labeled with ATTO-488 (λ_{ex} = 488 nm) and ATTO-647N (λ_{ex} = 640 nm). Scale bars: 20 µm.

tween the same population is enhanced by a factor of 1.2 more strongly at increased ionic strength. This appears reasonable as both base-pairing as well as electrostatic interactions are enhanced at increased ionic strength. Intra-population interactions, which are mediated by base-pairing and electrostatic interactions, should thus be affected more strongly. We can deduce that electrostatics contribute by about 20 % to the overall interaction, where base-pairing interactions dominate with 80 %.

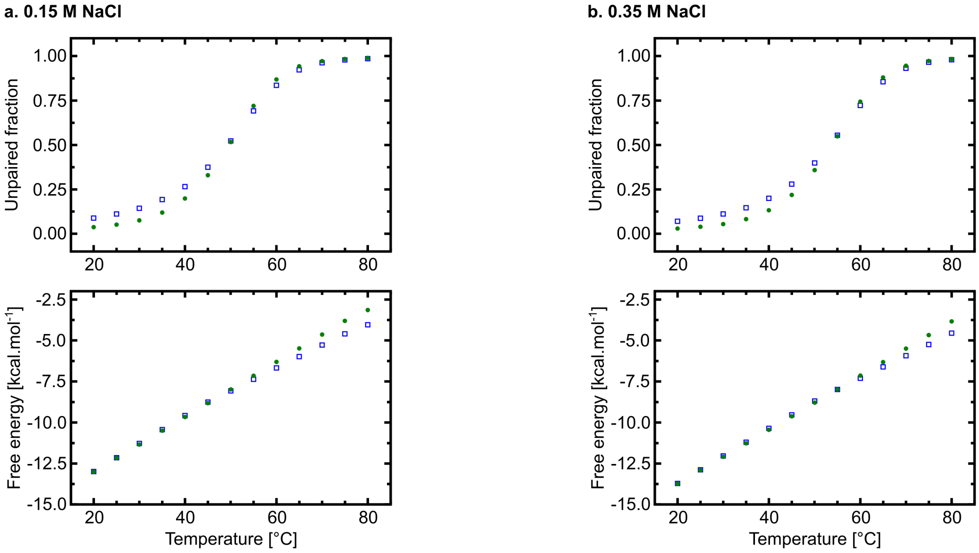

Figure 4.12: Melting profile of the sticky end sequences of the two DNA populations. The unpaired fraction and free energy of base pairing are plotted over different temperatures (20 −80 °C, 5 °C step) for the sticky end sequences of the green population (show in green circles) and the blue population (shown in blue empty squares). The melting profiles were simulated using NUPACK for 0.15 M NaCl (a) and 0.35 M NaCl (b) with a strand concentration of 160 µM.[253]

4.4 Towards a DNA segregation module for a bottom-up assembled synthetic cell

The evolvability of living systems requires a correlation between genetically encoded information (genotype) and function (phenotype). It is thus interesting to explore if the DNA segregation phenotype can, in principle, be controlled by the DNA sequence. The sequence of the sticky ends determines the strength of the intra-population interactions without affecting the interactions between the two different types of Y-motifs. According to our previous simulation results (Fig. 4.7c), we thus expect a sequence dependence of the segregation behaviour. More interestingly, the sticky end sequence can also impact the mechanical properties of the link, e.g. if unpaired bases are introduced which enhance the flexibility. We thus introduced one single free base between the arm of the Y-motif and its sticky end as illustrated in Fig. 4.13a. We observed a noticeable effect on the droplet formation for the blue Y-motif population (Fig. 4.14b), in agreement with previous reports [256]. Despite the higher melting temperature of the blue Y-motif compared to the green population (Fig. 4.12), this Y-motif forms more unstable droplets than the other population independent of the choice of fluorophores (Fig. 4.15) [257]. This is likely due to the lower fraction of unpaired bases of this population at elevated temperatures as revealed by an analysis of the melting profile (Fig. 4.12b). It is therefore interesting to study the effect of flexibility on the segregation process.

We find that increased flexibility alters not only the DNA droplet formation (Fig. 4.16) but also the DNA segregation. Upon cleavage at room temperature, all versions of the DNA droplets remain intact (Fig. 4.17) and only segregate upon heating.

With the original less flexible design, the DNA droplets undergo the previously reported segregation trajectory where the two populations become patchy before full segregation [173]. Now, in the cases where only one type of Y-motifs is modified, we observed a hierarchical core-shell organization within the DNA droplets where the modified population is the core shielded by the other population (Fig. 4.13a-ii,iii). The addition of the free base to both populations restored the patchy trajectory, however, with a more separated product (Fig. 4.13a-iv). These changes in spatial organization imply a change in the surface tension of the droplets which might be due to the exposed hydrophobic base of the unpaired adenine, which effectively acts as a surfactant. This also explains the observed wetting of the blue population during segregation at 65 °C (Fig. 4.11). Finite element simulations reveal a high dissociation probability of two bases in the sticky ends of the blue population at 65 °C while those of the green population remain fully paired (Fig. 4.18). This corroborates our hypothesis that unpaired bases may lead to surfactant-like behaviour of the corresponding DNA sequence.

RNA, which displays secondary structures exposing its bases, are a prominent constituent of many cellular condensates [258]. This poses questions on how much secondary structures and DNA unwinding influence the behaviours of their condensates and whether the cell also uses this to regulate its functions. In summary, we

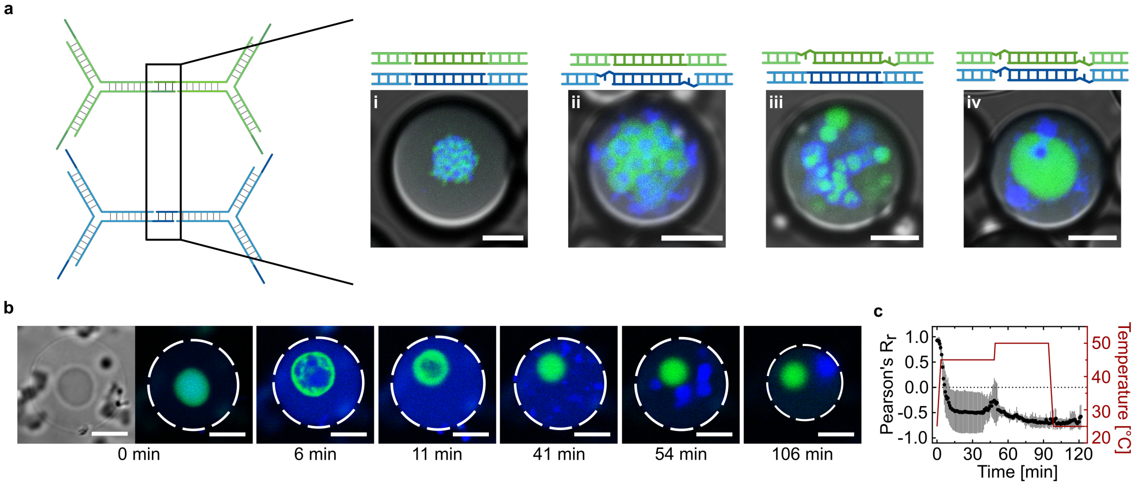

Figure 4.13: A DNA segregation module for synthetic cells. a) DNA sequence controls segregation phenotype. Confocal overlay images of photo-cleaved DNA droplets in water-in-oil droplets after heat treatment ($t = 5\,\text{min}$, $T = 50\,°\text{C}$). New sequences were designed by inserting one free base at the 3' end of both types of sticky ends (green and blue) and four combinations were generated from these four types of sticky ends (i-iv). The two DNA populations were labeled with ATTO-488 ($\lambda_{ex} = 488\,\text{nm}$) and ATTO-647N ($\lambda_{ex} = 640\,\text{nm}$). b) Confocal time series of a single DNA droplet inside GUV (brightfield image on the left) fully segregated into two daughter DNA droplets upon illumination ($\lambda = 405\,\text{nm}$, $t = 30\,\text{s}$, $I = 5\,\text{mW}$) and heat application. The two DNA populations were labeled with ATTO-488 ($\lambda_{ex} = 488\,\text{nm}$) and ATTO-647N ($\lambda_{ex} = 640\,\text{nm}$). Scale bars: 10 µm. c) Colocalization analysis of the two DNA populations (black circles, mean ± s.d, $n = 17$ z-planes) and the temperature profile (red line) over time.

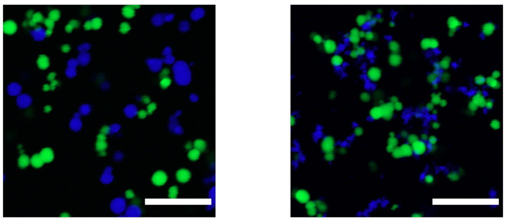

Figure 4.14: Introduction of one free nucleobase hinders DNA droplet formation of the blue population. Overlay of confocal images of the DNA droplets. The two populations were formed together without the linking motifs using the original strands (left) or the modified strands (right) where one free base is inserted between the sticky end and the Y-motif arm sequence. The two DNA populations were labeled with FAM ($\lambda_{ex} = 488\,\text{nm}$) and DY405 ($\lambda_{ex} = 405\,\text{nm}$). Scale bars: 20 µm.

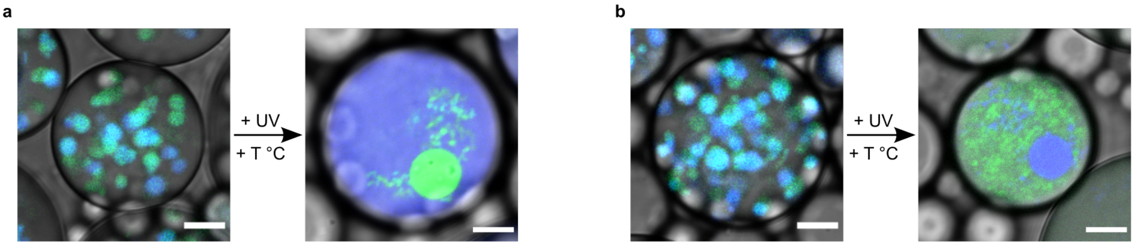

Figure 4.15: DNA droplet stability after exchanging fluorophores between the two populations. Confocal overlay of brightfield and confocal images showing DNA droplet stability inside water-in-oil droplets before (left) and after cleavage and incubation at 55 °C for 105 min (right). The green and blue populations were labeled with ATTO-488 ($\lambda_{ex} = 488\,\text{nm}$) and ATTO-647N ($\lambda_{ex} = 640\,\text{nm}$) respectively (a) and vice versa (b). The color of the two populations are switched in (b) to highlight that DNA droplet stability is independent of the fluorophore choices. Scale bars: 10 µm.

have shown that, with the DNA sequence, we can not only regulate the kinetics of the DNA segregation but also the segregation trajectory in confinement.

Beyond sequence programmability, another important feature of a DNA segregation module for synthetic cells is that it should ultimately function inside of lipid vesicles. As the next step, we thus reconstituted the DNA droplets in giant unilamellar lipid vesicles (GUVs). Since the reconsititution in water-in-oil droplets was successful, we decided to use the droplet-stabilized GUV formation method, which uses water-in-oil droplets as a template for the formation of free-standing GUVs [186, 252]. In brief, we encapsulated all components required for the DNA segregation together with small unilamellar lipid vesicles (SUVs) in water-in-oil droplets. The SUVs fuse at the water-oil-interface to form a spherical supported lipid bilayer, which can be released from the droplet as a conventional GUV. After GUV formation, the single-stranded DNA is annealed to form the initial DNA droplet in GUVs. The segregation process was successfully triggered by RNase A activity (Fig. 4.19) or locally by light (Fig. 4.13b, Fig. 4.20). The light-driven segregation is captured

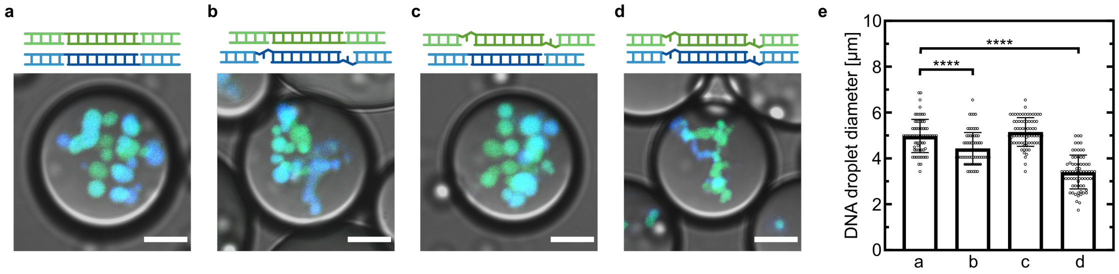

Figure 4.16: Introduction of one free nucleobase alters the DNA droplet formation process. Overlay of brightfield and fluorescence images of encapsulated DNA droplets in water-in-oil droplets. DNA droplet formation from the four combinations mentioned in Fig.4.13a was observed (a-d). The droplet diameter of each combination was analyzed (e), showing significant changes in droplet size when the nucleobase is introduced in the blue population (p-value < 0.0001 (****)). Two-tailed unpaired t-test with Welsch's correction was performed (n=71 DNA droplets pooled from $\geq$ 15 water-in-oil droplets). The two DNA populations were labeled with ATTO-488 ($\lambda_{ex} = 488\,\mathrm{nm}$) and ATTO-647N ($\lambda_{ex} = 640\,\mathrm{nm}$). Scale bars: 10 µm.

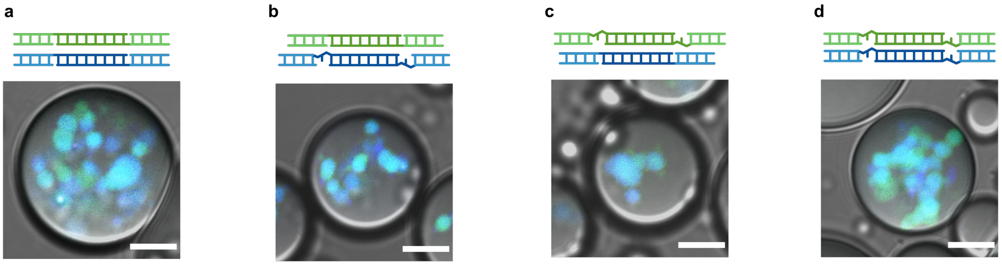

Figure 4.17: DNA droplet integrity after light cleavage.Overlay of brightfield and fluorescence images of the encapsulated DNA droplets in water-in-oil droplets after photocleavage. The DNA droplets were made from different strand combinations as desciribed in Fig.4.13a (i-iv). The two DNA populations were labeled with ATTO-488 ($\lambda_{ex} = 488\,\mathrm{nm}$) and ATTO-647N ($\lambda_{ex} = 640\,\mathrm{nm}$). Scale bars: 10 µm.

over time and colocalization was analyzed for a quantitative view of the segregation process (Fig. 4.13b,c). By reproducing DNA segregation in GUVs, we come closer to a controllable analogue of cell division which would open new doors for the idea of constructing a synthetic cell from scratch.

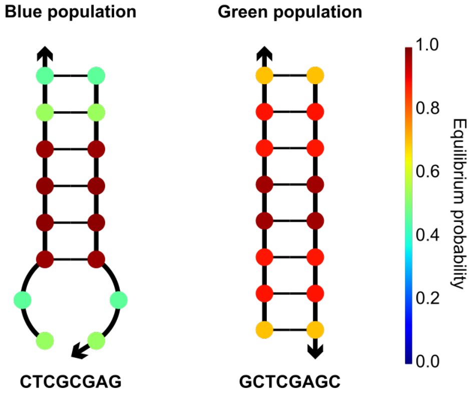

Figure 4.18: Simulated structures of sticky end sequences show unpaired bases for blue population at 65 °C. Minimum free energy secondary structures of the paired fraction are shown for the sticky end sequences of the blue population (left) and the green population (right). Each nucleobase is color-coded with its equilibrium probability. Structures were simulated using NUPACK with a DNA concentration of 160 µM (reflecting the crowded environment inside the DNA droplet) and a sodium ion concentration of 0.35 M at 65 °C.[253]

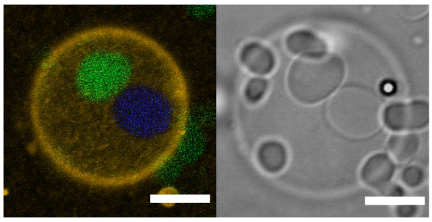

Figure 4.19: DNA droplet segregation triggered by enzymatic activity in GUVs. Fluorescence overlay (left) and brightfield (right) images showing segregated DNA droplet inside GUV after incubation at 50 °C for 30 min. The green population was labeled with FAM (λ_{ex} = 488 nm) and Cy5 (λ_{ex} = 651 nm). The blue population was labeled with DY405 (λ_{ex} = 405 nm). The lipid membrane was labeled with Liss Rhod PE (λ_{ex} = 561 nm). Scale bars: 10 µm.

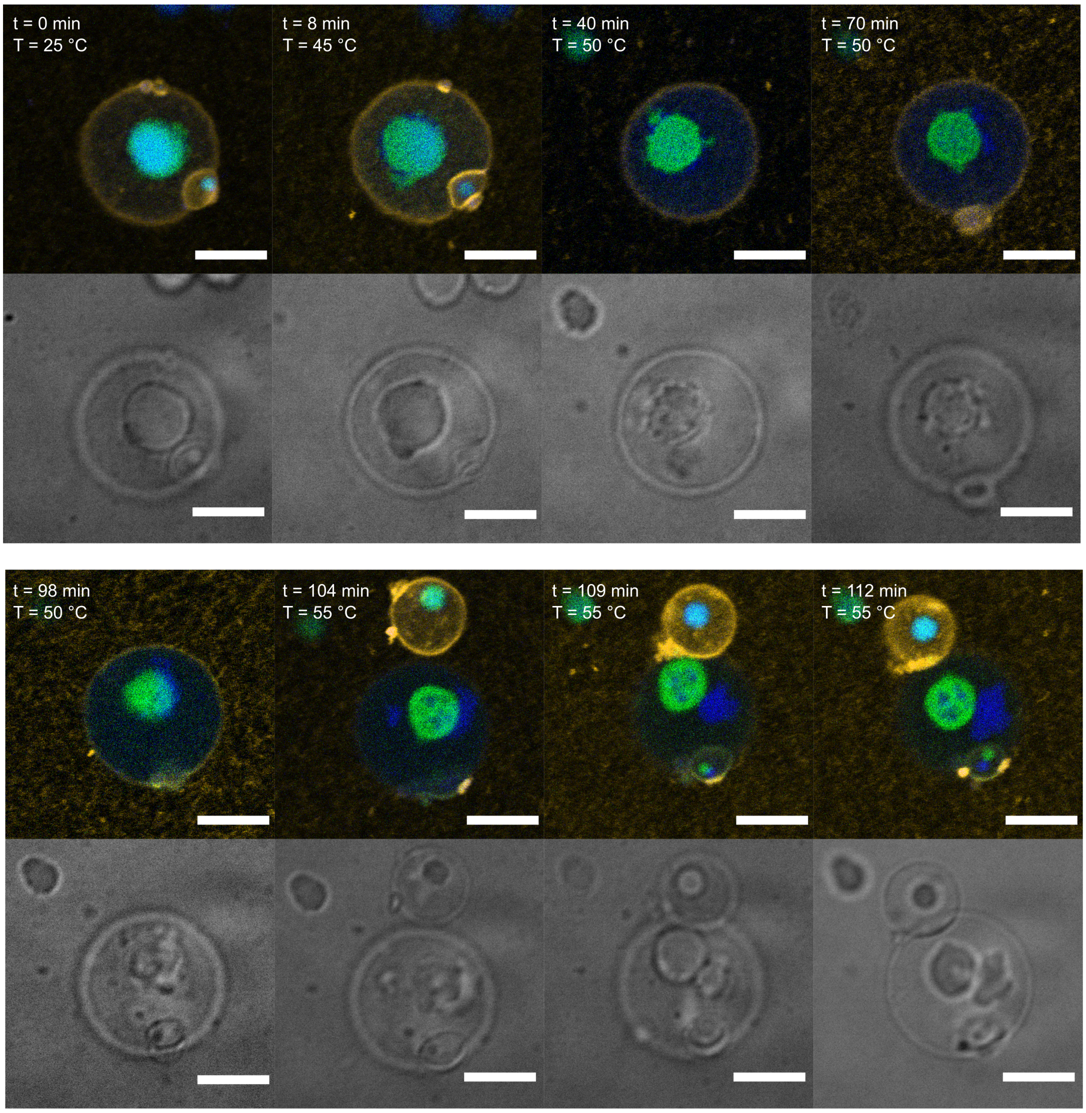

Figure 4.20: Time series of DNA droplet segregation locally triggered by light in GUVs. Fluorescence overlay (upper panel) and brightfield (lower panel) images showing DNA droplet segregation process inside GUV after photocleavage ($t = 1\,\text{min}$, $\lambda = 405\,\text{nm}$, 5 mW power). From 100 min, an unilluminated GUV entered the field of view (see also Video S4). The absence of DNA droplet segregation the unilluminated GUV highlights the spatiotemporal control over the cleavage. The two DNA populations were labeled with ATTO-488 ($\lambda_{ex} = 488\,\text{nm}$) and ATTO-647N ($\lambda_{ex} = 640\,\text{nm}$). The lipid membrane was labeled with Liss Rhod PE ($\lambda_{ex} = 561\,\text{nm}$). Scale bars: 10 µm.

4.5 Discussion

The segregation of informational molecules like DNA, is a hallmark of natural cell cycle, which makes the quest for a mechanism of DNA spatial segregation pivotal for the construction of a synthetic cell. Bottom-up synthetic biology has recently witnessed a myriad of successful and reliable approaches to divide lipid vesicles as synthetic cellular compartments. Now, it will be important to combine compartment division with suitable mechanisms for DNA segregation. Random partitioning, entropy-driven segregation and the reconstitution of the biological machinery have been proposed for this purpose [188]. Here, we realize a DNA segregation module in water-in-oil droplets and GUVs, which makes use of the physical principles of liquid-liquid phase separation. It provides more control than random partitioning, while maintaining a relatively simple set of components. It is conceivable that early synthetic cells could function with a membrane-free nucleus mimic. However, the downside of our system is the fact that at least the sticky end sequences of the daughter droplets cannot be identical. Therefore, the realization of multiple growth and division cycles would require a mechanism for regeneration. Yet, studying DNA droplets and their segregation kinetics is interesting in itself, as it provides a model system to shed light on the relation between DNA packing and access of DNA binding proteins like transcription factors. We have seen an example of this when revealing the different segregation kinetics for the enzymatic and the photo-induced segregation. Notably, the role of geometric confinement was observed to play a role in slowing down the segregation process, emphasizing compartmentalization as a requisite for the apprehension of cellular systems. Furthermore, a lattice-based model could capture the phenotypic behaviors of DNA droplet segregation. We also demonstrate orchestration of the system dynamics via temperature, ionic strengths and nucleobase sequences. With such versatile control toolbox, our system is not limited to the biomimicry of biocondensates but can be used as an engineerable model system for studying physical properties of LLPS and nucleotide interactions of natural cells. Our further implementation of the process into GUVs does not only bring the system closer to its natural analogue but also allows, in principle, for feeding mechanisms using targeted vesicle fusion to be applied for recurrent segregation [130, 194]. As a next step, it will be crucial to combine the DNA segregation modules with existing modules for compartment division [194]. Altogether, our work presents a physical approach towards providing a functional DNA segregation module for synthetic cells. Furthermore, our results will not only benefit the development of a fully synthetic cell but also prompt new questions on the role and properties of DNA in subcellular condensates.

5

Genetic encoding and expression of RNA origami cytoskeletons in synthetic cells

Author Contributions and Reuse Statement

This chapter includes material adapted from:
Mai P Tran*, Taniya Chakraborty*, Erik Poppleton, Luca Monari, Maja Illig, Franziska Giessler, Kerstin Göpfrich; 'Genetic encoding and expression of RNA origami cytoskeletons in synthetic cells', *Nat. Nanotechnol.* (2025), `https://doi.org/10.1038/s41565-025-01879-3`. * Contributed equally
This chapter, including figures and text, are excerpts from the aforementioned publication. These materials are reused with permission under a CC BY license. No individual citations are provided within this chapter for the reused content. All reused material has been integrated into the flowing narrative of this thesis and re-contextualized where necessary.
I did all the experiments and analyses presented in this chapter, except for the experiments and analyses in Figure 5.2e-h, 5.5, 5.6, 5.7, 5.8, 5.10, 5.12c, h, i, 5.19, 5.21, 5.29a, d, f, 5.30, 5.31b, c, 5.32, 5.33, 5.34, and 5.35. All co-authors provided feedback on experimental results and contributed to manuscript revisions. The final texts reflect a collaborative effort.

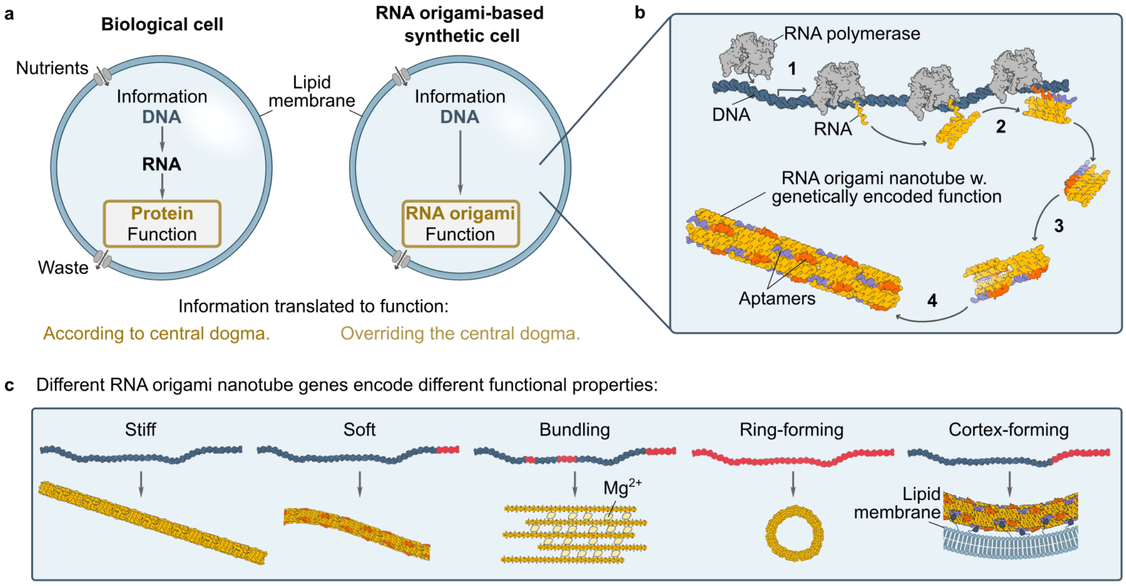

Figure 5.1: Motivation and conceptualization for engineering RNA origami-based hardware for synthetic cells. **a)** Biological cells function according to the Central Dogma (DNA serves as a template for RNA, and RNA directs protein synthesis), necessitating the involvement of about 150 genes in the translational process. In contrast, a synthetic cell built with RNA origami requires fewer genes while maintaining evolvability. **b)** Mechanism of co-transcriptional RNA origami. A DNA template is transcribed by RNA polymerase, whereby the RNA folds up into tiles that self-assemble into higher-order RNA origami nanotubes. The folding steps are numbered: the nascent RNA folds first into local secondary structures (stem-loops), followed by the formation of long-distance tertiary structures through internal kissing loops, and finally oligomerization via various quaternary interactions (external kissing loops, overhangs and aptamers). **c)** Information-function correlation. Mutations on the DNA template result in RNA origami nanotubes with different properties.

5.1 Expression of RNA origami within GUVs

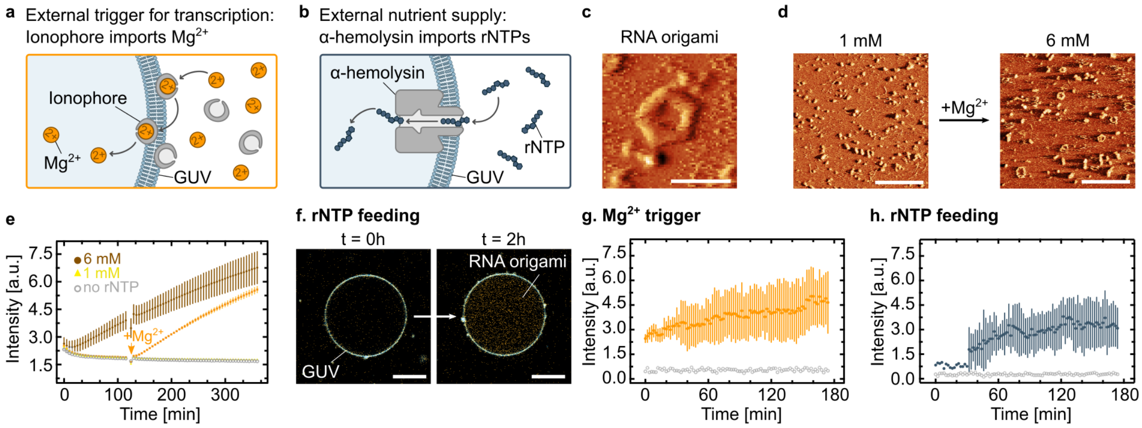

Figure 5.2: Expression of RNA origami inside GUVs. **a-b)** Schematic illustration showing the external triggers for RNA origami expression by Mg^{2+} import using ionophores **(a)** or rNTP feeding via α-hemolysin pores **(b)**. **c)** AFM micrograph of the pentagon-shaped RNA origami (3H-4DT-iSpi), composed of 5 subunit with three helices each. Scale bar: 50 nm. **d)** AFM micrographs of Mg^{2+}-triggered 3H-4DT-iSpi RNA origami. RNA was incubated for 2 h at 1 mM $Mg(OAc)_2$ (left) before transcription was triggered by increasing $Mg(OAc)_2$ to 6 mM and incubated for another 2 h (right). Scale bars: 200 nm. **c and d** are images from lock-in phase channel. The corresponding height images are shown in Fig. 5.4. **e)** Fluorescence plate reader experiments tracking 3H-4DT-iSpi RNA origami production by measuring DFHBI-1T emission over time ($\lambda_{ex} = 488$ nm, mean ± s.d, $n = 3$ wells). The orange arrow indicates the time point where the $Mg(OAc)_2$ concentration was increased from 1 mM to 6 mM. **f)** Confocal overlay images of 3H-4DT-iSpi RNA origami (orange, iSpinach binds DFHBI-1T, $\lambda_{ex} = 488$ nm) transcribed inside of a GUV (blue, membrane labelled with DiD, $\lambda_{ex} = 640$ nm). Quantification in Fig. 5.3. Scale bars: 20 µm. **g-h)** RNA origami transcription inside of GUVs triggered by addition of Mg^{2+} (**f**) or rNTPs (**g**) over time (mean ± s.d, $n = 6$ GUVs). The data was extracted from confocal fluorescence timelapse recordings. Empty gray circles denote the background fluorescent signal outside of the GUVs.

We first aimed to encapsulate the DNA template and the transcription machinery required for the production of RNA origami inside GUVs (Fig. 5.1). Compared to *in vitro* transcription (IVT) in bulk, we first have to ensure that transcription is indeed happening inside the compartment and not prior to encapsulation. Therefore, an external trigger is needed. Second, due to the limited reaction volume of the GUV, nutrient depletion and waste accumulation would stall and favor abortive initiation of the transcription process [259]. We thus introduce two distinct control schemes: restriction of the essential cofactor, Mg^{2+}, and restriction of rNTPs.

We chose a Mg^{2+} ionophore [260] capable of shuttling Mg^{2+} across the membrane with high specificity (Fig. 5.2a). The ionophore gives us a membrane-protein-free closed system [231], however, waste from the transcription process cannot escape the vesicle.

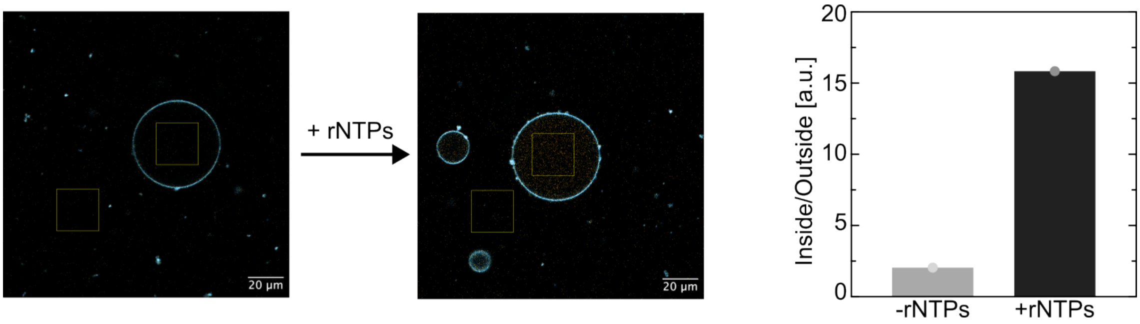

Figure 5.3: Quantification of the increase in fluorescence after addition of rNTPs shown in Fig. 2f. The mean intensity inside the GUV (highlighted by the yellow box) compared to the exterior region in the same image, both in the absence and presence of rNTPs. A 7-fold higher mean intensity was observed upon the addition of rNTPs.

For combined Mg^{2+} import, nucleotide feeding and waste removal, we incorporated the commonly used bacterial transmembrane pore α-hemolysin. With a constriction of 1.4 nm, this pore allows us to continuously fuel transcription from a bulk feeding solution (containing rNTPs and Mg^{2+}), while preventing the escape of the larger DNA template, RNA polymerase, and RNA origami structures (Fig. 5.2b).

We initially chose a previously realized 2D RNA origami that has a well-defined structure and attached a fluorescent iSpinach aptamer [261] to the 3' end (3H-4DT-iSpi, originally designed in [89], Fig. 5.4). The RNA origami folds into a 3-helix tile, which further assembles into a 5-tile pentagon with 20 nm edges (Fig. 5.2c). Experiments showed that 1 mM Mg^{2+} is insufficient for transcription (Fig. 5.2d, left), while we obtained the correctly folded RNA origami at 6 mM (Fig. 5.2d, right, Fig. 5.2e, Fig. 5.4b). We verified these findings with another RNA origami design [89] (Fig. 5.5).

Next, we moved the transcription of the RNA origami into GUVs. The ionophore and Mg^{2+} were added to the external buffer after GUV formation. We tracked RNA origami production by observing iSpinach fluorescence inside individual GUVs with confocal microscopy (Fig. 5.2g, Fig. 5.6, Fig. 5.7). The mean fluorescence intensity inside the GUVs increased consistently over time compared to the bulk solution, confirming successful RNA origami production.

To implement nucleotide feeding, we reconstituted α-hemolysin in the GUVs [128]. As all salts required for transcription could be supplied after formation, this strategy improved the GUV formation efficiency, which is sensitive to ions [262]. RNA origami production was successfully initiated by adding rNTPs and salts to the external buffer (Fig. 5.2f,h, 5.8, 5.9, 5.10). A control experiment showed similar transcription patterns triggered with rNTPs in bulk solution (Fig. 5.7).

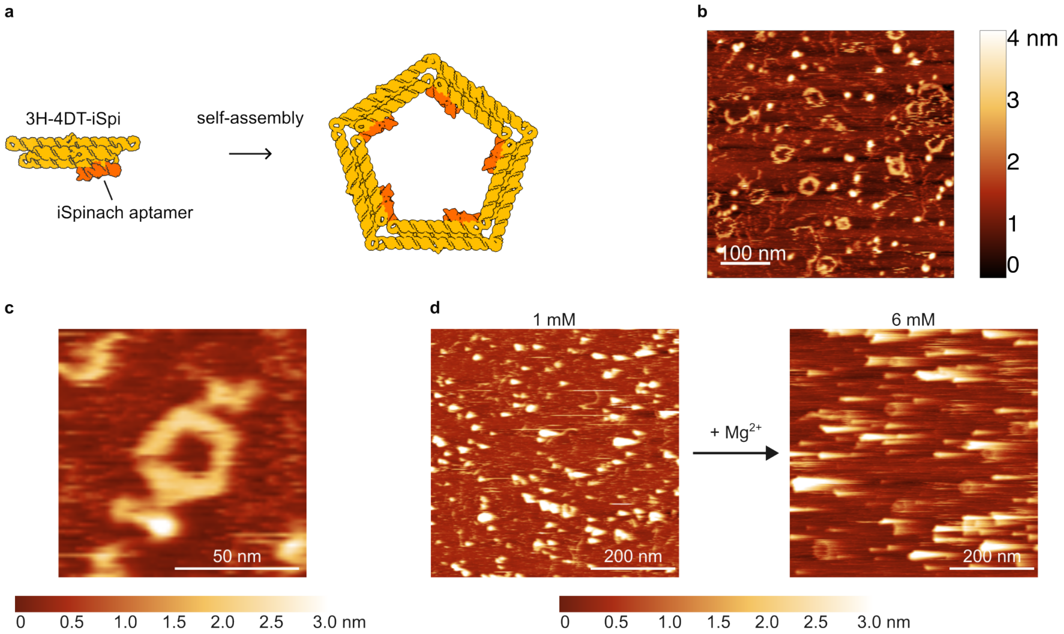

Figure 5.4: Verification of RNA origami production. **a)** Schematic representation of the 3H-4DT-iSpi RNA origami design. **b)** AFM image of the 3H-4DT-iSpi RNA origami folded co-transcriptionally in a buffer containing 6 mM Mg^{2+}. The 3H-4DT-iSpi RNA origami design is taken from Geary et al. [89]. **c-d)** The height images corresponding to the micrographs in Fig. 5.2c-d, respectively.

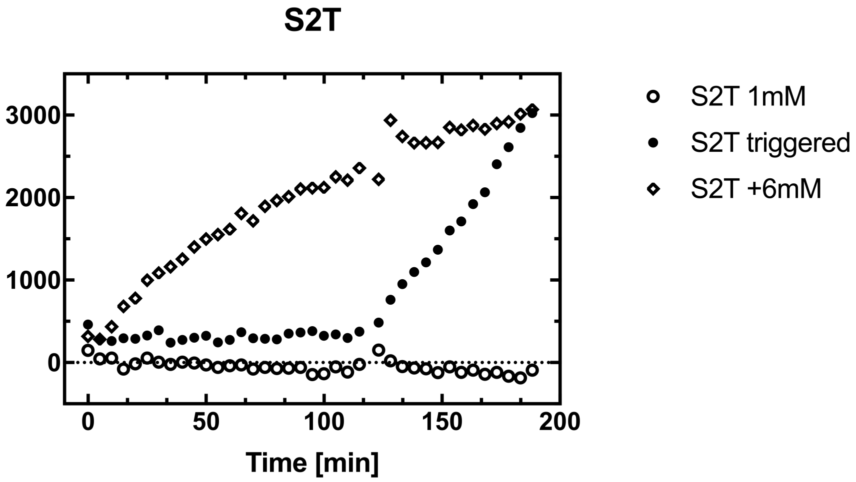

Figure 5.5: S2T RNA origami production upon Mg^{2+} addition. Mean spectrophotometer readout of DFHBI-1T fluorescence ($\lambda_{ex} = 488\,\text{nm}$) is plotted over time ($n = 3$ wells per condition). At 1 mM $Mg(OAc)_2$ (empty circles), the fluorescence remains constant, indicating that no RNA origami is produced. However, addition of 5 mM $Mg(OAc)_2$ to reach a final concentration of 6 mM (here at t = 120 min) leads to an immediate increase in fluorescence, indicative of RNA origami production (filled circles). This increase is also seen in a positive control where the initial solution contains 6 mM $Mg(OAc)_2$ throughout the entire measurement (empty diamonds). This confirms that RNA origami production can be triggered by the addition of Mg^{2+}. The S2T RNA origami design is taken from Geary et al [89].

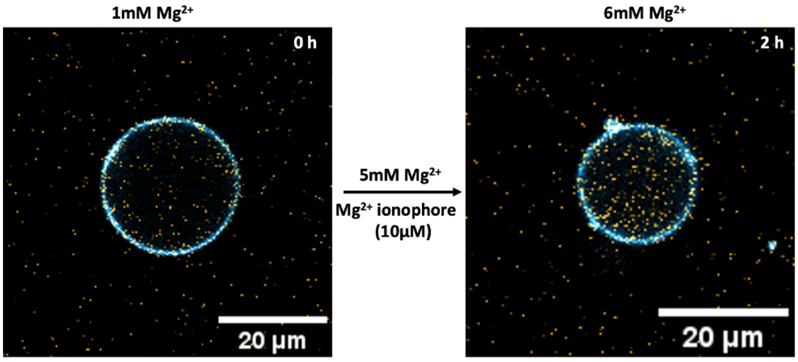

Figure 5.6: Expression of the 3H-4DT-iSpi RNA origami in GUVs triggered by externally added Mg^{2+}, transported into the GUVs by using ionophores. Left: GUV containing 1 mM Mg^{2+} and all other transcriptional components along with rNTPs. Right: Transcription of 3H-4DT-iSpi RNA origami was triggered by addition of 5 mM Mg^{2+} and 10 µM Mg^{2+} ionophore. Image taken after 2 h incubation at 37 °C.

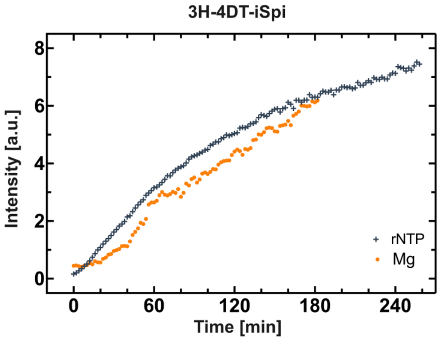

Figure 5.7: RNA origami production in bulk measured with confocal microscopy. Mean fluorescence intensity of 3H-4DT-iSpi RNA origami was monitored at 37 °C. Transcription was triggered by the addition of 5 mM Mg^{2+} (orange circles) or with 4 mM rNTPs (gray crosses) for 3 h or 4 h, respectively.

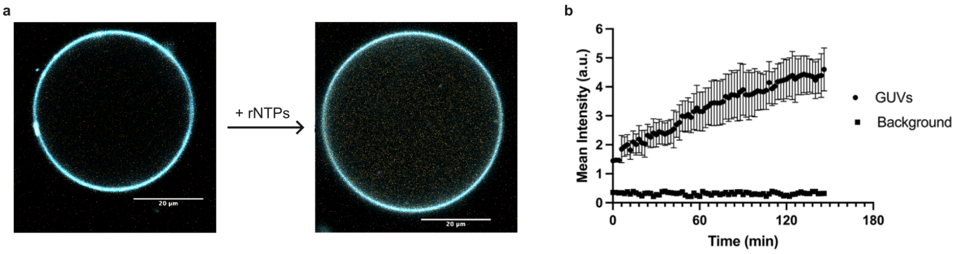

Figure 5.8: S2T RNA origami transcription and folding inside GUVs triggered by rNTP addition. **a)** Confocal images showing S2T RNA origami expression initiated by the external addition of 4 mM rNTPs. GUVs were incubated for 2 h before the left image was taken; the right image was taken 2 hours after transcription was initiated. rNTP fuelling was achieved by the presence of α-hemolysin in the GUV membrane. **b)** S2T RNA origami transcription inside of GUVs triggered by addition of rNTPs plotted over the first 2.5 h of expression (mean ± s.d, $n = 10$ GUVs). The data was extracted from confocal fluorescence timelapse recordings. Background fluorescence outside of the GUVs is plotted as black squares.

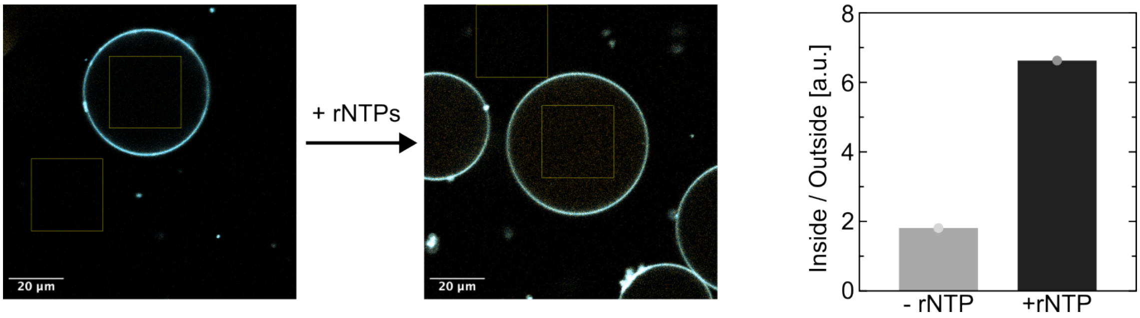

Figure 5.9: Quantification of the increase in fluorescence after addition of rNTPs shown in Fig. 5.8a. The mean intensity inside the GUV (highlighted by the yellow box) compared to the exterior region in the same image, both in the absence and presence of rNTPs. A 3-fold higher mean intensity was observed upon the addition of rNTPs.

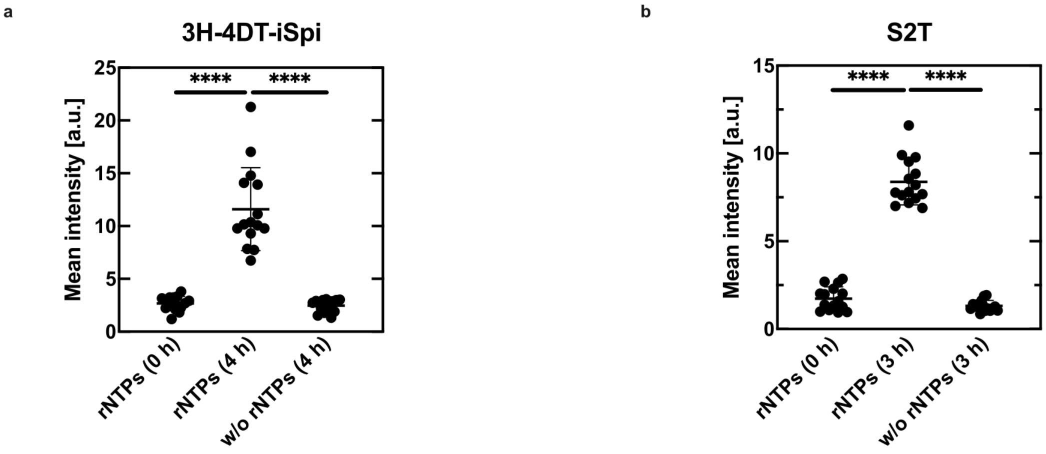

Figure 5.10: RNA origami transcription in GUVs triggered by rNTP addition and measured by confocal microscopy. Transcription was carried out at 37 °C. GUVs (n = 15) were initially randomly chosen in the membrane dye channel (DiD), followed by a comparison of their fluorescence intensity in the iSpinach channel. **a)** The mean fluorescence intensity of 3H-4DT-iSpi RNA origami increased significantly 4 h after the addition of rNTPs, compared to the intensity before or without the addition of rNTPs. **b)** Mean fluorescence intensity of S2T RNA origami increased significantly 3 h after the addition of rNTPs, compared to the intensity before or without the addition of rNTPs. The mean and standard deviation are represented in black lines. Parametric, unpaired t tests with Welch's correction were performed. Two-tailed P values are marked with **** (p = 3.3e−7, 2.7e−7, 7.6e−14, 1.5e−12 , from left to right).

5.2 Co-transcriptional folding of RNA origami nanotubes

Having successfully expressed RNA origami in GUVs, we set out to provide a proof-of-principle for the genetic encoding of RNA origami structures with cell-like functions. Inspired by the success of DNA-based mimics of cytoskeletons [68, 159–161, 163, 168], we wanted to realize genetically encodable RNA origami nanotubes. For our purpose, an RNA cytoskeleton has to fold co-transcriptionally and form stiff, cell-sized structures from a low number of genes (strands). Previous studies have demonstrated micrometer-scale 1D [263] and 2D [157, 158, 264] RNA filaments; however, they required thermal annealing and were not produced co-transcriptionally. Moreover, microtubules, nature's stiffest filaments, have a hollow 3D architecture which maximizes the trade-off between material and persistence length. In line with these criteria, we engineered single-stranded RNA tiles that were able to co-transcriptionally fold and assemble into micrometer-length nanotubes.

The design process (Fig. 5.11a) yielded a "wild-type" (WT) tile with approximate dimensions of 11 nm x 5 nm x 2.5 nm forming a nanotube with an outer diameter of 11 nm (Fig. 5.11b). The *in silico* design was then validated experimentally with AFM. The co-transcriptionally folded tiles assembled into nanotubes up to several micrometers in length. AFM yielded an apparent nanotube height of 5 to 6 nm which corresponds to at least two RNA duplexes lying on top of one another (an unravelled nanotube would have a height below 2 nm corresponding to a single RNA duplex) (Fig. 5.12b). At the same time, the measured width is ~22 nm (Fig. 5.13). The deviations from the expected dimensions are consistent with the expected tip compression and surface collapse for a hollow nanotube design. Due to strong kissing loop interactions, RNA nanotubes withstand temperatures up to 50 °C (Fig. 5.14).

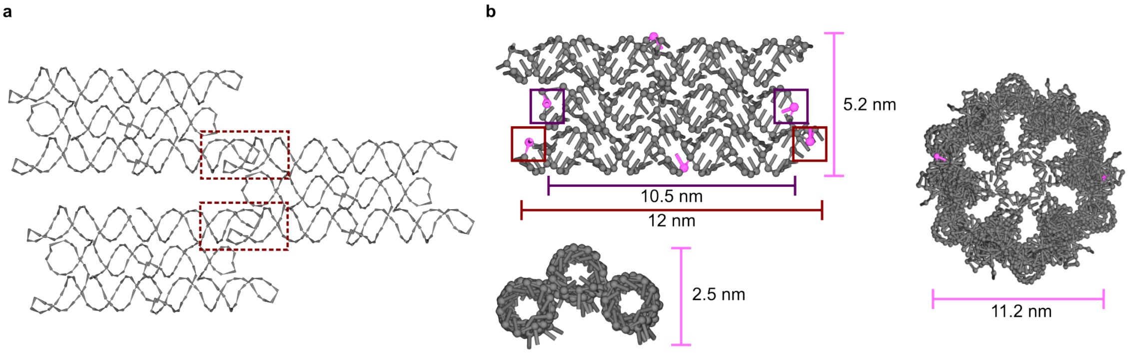

Figure 5.11: *In silico* design of the wildtype (WT) RNA origami tiles for nanotube formation. **a)** Schematic of intertile interactions indicating the direction of the external kissing loops (dotted red box). To minimize the number of components, we employed 180° kissing loops for homotypic tile-tile interactions. These external kissing loops allow for more tile-tile cohesion points per strand, which are necessary for strengthening the nanotubes, than traditional sticky-end hybridization methods. Additionally, this approach allows us to compose each tile from a single strand rather than the conventional five strands per tile used in double-crossover (DX) tile motifs known from DNA nanotechnology [109, 110, 158]. Furthermore, unlike traditional multi-strand RNA/DNA nanotube designs where intrinsic curvature is introduced at the tile-tile interaction level using offsets in the helix axes [110], we introduced curvature directly in individual tiles with dovetail junctions (−3 dovetail) [89, 227]. This produced the desired radial curvature of 120° for a three-tile nanotube where each tile is connected corner-to-corner by 180° kissing loops. Given that the 11 base-per-turn characteristic of the RNA helix does not enable symmetrical tile designs, we optimized the loop lengths by visual inspection, and generated the sequence using Revolvr [83, 89]. **b)** Dimensions of the WT tile and the resulting RNA origami nanotube extracted from RNAbuild[89] of the *in silico* design. The nucleotides used as reference points for measurement are highlighted in pink.

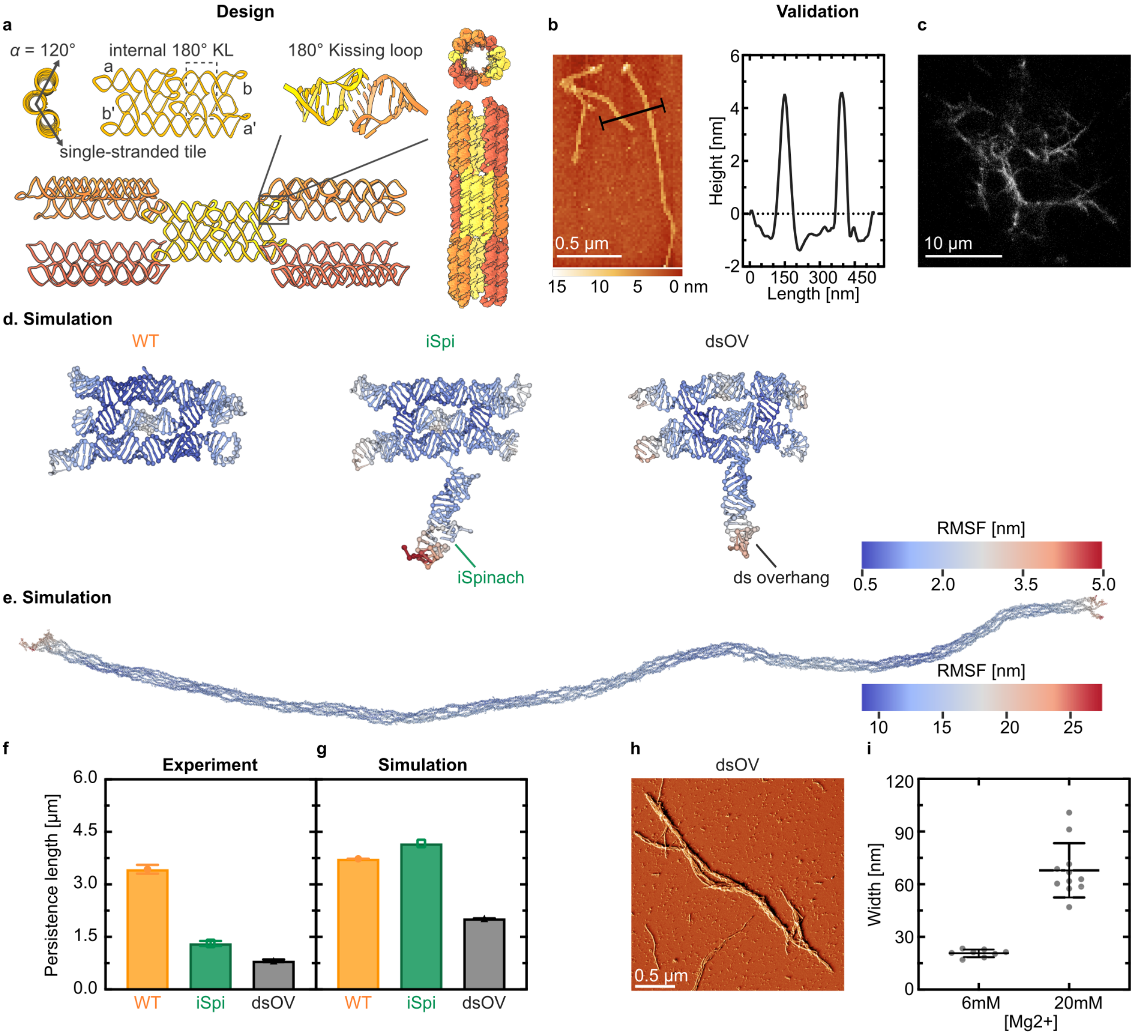

Figure 5.12: Design and characterization of cytoskeleton-like RNA origami nanotubes. **a)** *In silico* design of RNA origami nanotubes. The nanotube-forming RNA origami tiles assemble co-transcriptionally from a single RNA strand, forming 3 duplexes with $\alpha = 120°$ intrinsic curvature. The 180° external kissing loops for nanotube assembly are paired corner-to-corner (a-a' and b-b'). **b)** AFM micrograph of WT RNA origami nanotubes. The height profile is plotted along the black line. **c)** Confocal image of iSpi RNA origami nanotubes after 12 h of IVT. Fluorescence visualization was achieved by including an iSpinach aptamer and DFHBI-1T dye ($\lambda_{ex} = 488\,\text{nm}$). **d)** OxRNA molecular dynamics simulations of WT, iSpi and dsOV RNA origami tiles. **e)** OxRNA molecular dynamics simulation of a 300-tile assembly (here: WT). **d,e)** show the centroid structures from simulation. Each nucleotide is colored by its root-mean-square fluctuation (RMSF). **f-g)** Persistence length of the RNA origami nanotubes calculated from AFM images (mean ± s.d of fit, see Methods) and simulations (300-tile nanotubes during the final 10% of the time steps, mean ± propagated s.d of fit, $n = 603$ simulation frames). (Continued on the following page.)

Figure 5.12: (continued) **h)** AFM micrograph (error signal mode) of bundled dsOV RNA origami nanotubes upon addition of Mg^{2+} as a crosslinker. The corresponding height image is shown in Fig. S18. **i)** Width of non-bundled and bundled dsOV RNA origami nanotubes (mean ± s.d, $n = 8$ and 11 nanotubes, respectively).

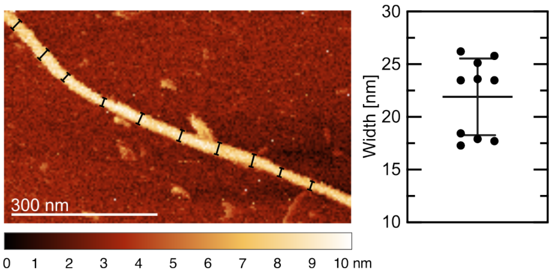

Figure 5.13: AFM micrographs of cotranscriptionally folded RNA origami nanotubes. High magnification AFM micrographs of a WT RNA origami nanotube. Ten width measurements from one exemplary nanotube were performed along the black lines and shown in the plot on the right ($n = 10$). The measurements yielded dimensions of 21.91 ± 3.632 nm. The mean and standard deviation are represented in black lines.

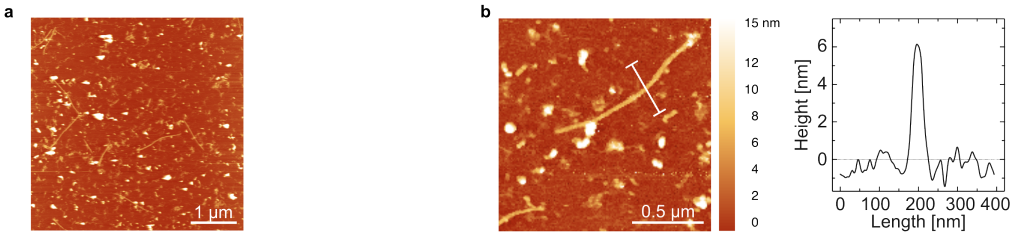

Figure 5.14: Stability of RNA nanotubes. **a)** AFM micrograph of cotranscriptionally folded RNA origami nanotubes after incubation at 50 °C for 1 h. **b)** A zoom in showing the height profile of the RNA nanotube at the white line. The RNA nanotube was intact and at the correct height of 6 nm. In contrast, DNA nanotubes have been shown to completely disintegrated at 46 °C after 30 min [265]. The AFM micrographs acquired in this paper were done at 50-100 pN on mica substrate and imaging was done between 20-90 min. The RNA nanotubes remained unopened during the imaging process.

Next, we designed a tile with an iSpinach aptamer extending from the the 3' end (hereafter "iSpi") to vizualize the RNA origami nanotubes with confocal microscopy. We obtained cytoskeleton-like networks tens of microns across (Fig. 5.12c). Compared to AFM, confocal microscopy was performed without removing the DNA template and the polymerase in a purification step. The addition of the relatively bulky iSpi aptamer does not influence the mean length of the RNA origami nanotubes (Fig. 5.15).

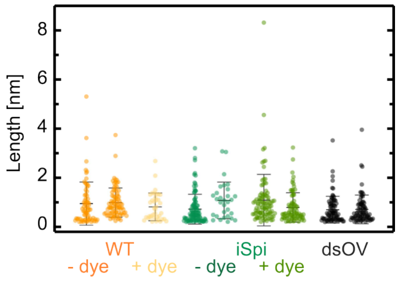

Figure 5.15: Contour length distribution of RNA origami nanotubes extracted from AFM images. Wild-type: WT; iSpinach aptamer on the 3' end: iSpi; and double-stranded overhang on the 3' end: dsOV. Mean lengths of WT, iSpi and dsOV (from left to right, all replicates pooled) are: 970.9 ± 735.1 nm and 814.8 ± 564.1 nm; 802.1 ± 657.0 nm and 952.4 ± 883.3 nm; and 706.1 ± 563.8 nm, respectively. Each column represents one replicate. All conditions have 2 replicates except WT+dye. $n = 152$ (69 and 83), 38, 133 (103 and 30), 175 (95 and 80), 159 (80 and 79) for WT, WT+dye, iSpi, iSpi+dye and dsOV, respectively. Mean and standard deviation are presented in black lines. The spread of the contour length is indicative of possible frequent assembly defects.

Since the modification of individual tiles is key for the creation of functional cytoskeletons, we generated a third design modified with a double-stranded loop-out (hereafter "dsOV"). The loop-out sequence is connected to the tile via a three-way junction near, but not at, the 3' end (Fig. 5.12d). The dsOV nanotubes feature slightly lower mean length (706.1 ± 563.8 nm versus 970.9 ± 735.1 nm for WT).

With coarse-grained molecular dynamics (MD) simulations, we simulated single tiles (Fig. 5.12d) as well as 1 µm (300-tile) nanotubes using the oxRNA model [232, 236]. The 300-tile assemblies were built from relaxed monomers, resulting in simulations with over 90000 nucleotides (Fig. 5.12e, Fig. 5.16). To our knowledge, these are the largest structures simulated in oxRNA to-date. We compared the persistence length of the nanotubes extracted from AFM images with the that of simulated nanotubes (Fig. 5.12f,g). Experiments yielded a persistence length of 3.4 µm for WT nanotubes, while iSpi and dsOV exhibited lower persistence lengths (1.3 µm and 0.8 µm, respectively). The addition of dye did not impact the persistence length (2.6 µm for WT and 1 µm for iSpi, Fig. 5.24).

Despite overestimating the persistence lengths of iSpi and dsOV nanotubes (4.2 µm and 2.0 µm, respectively), the MD simulations estimated the persistence length of the WT nanotubes almost correctly at 3.7 µm. The simulation also reproduced the fact that the dsOV tiles yield the least stiff nanotubes. Since oxRNA

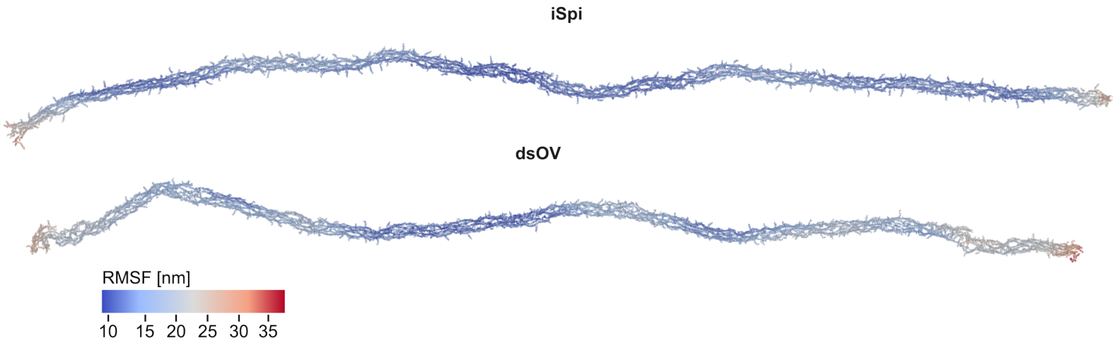

Figure 5.16: Coarse-grained molecular dynamics simulation of a 300-tile assembly (top: iSpi, bottom: dsOV). The centroid structure from one of the simulation runs is shown. Each nucleotide is color-coded according to its root-mean-square fluctuations (RMSF).

lacks the ability to model non-canonical base-pairing and charges are represented implicitly, we do not expect to perfectly capture the effects of highly structured aptamers such as iSpinach. However, the results with the WT and dsOV structures give us confidence in using the coarse-grained simulations to explore the observed differences in stiffness at the nucleotide level.

In the simulations of the dsOV nanotubes, we observe higher rates of bond-breaking, which are not seen in the WT design (Fig. 5.17, 5.18). This indicates that the lower persistence length of dsOV may result from assembly defects and fragmentation of assembled RNA origami nanotubes.

In experiments, the ratio of calculated persistence length to mean contour length, which indicates the flexibility of the nanotubes, was approximately 3.5 for WT, 1.6 for iSpi and 1.1 for dsOV. These results suggest that while the addition of a helix does not affect the length of the resulting nanotubes (Fig. 5.15), it does impact their flexibility (Fig. 5.12f). We hypothesize that there are two major factors impacting nanotube stiffness, namely steric hindrance during assembly and intrinsic tile flexibility in the assembled nanotubes (as discussed in the next section, Fig. 5.17, 5.18, 5.19, 5.20).

It is known that flexibility impacts polymer aggregation. Flexible polymers experience negligible loss of entropy during dimerization, making bundling more favorable compared to semiflexible polymers [266]. Since bundling is key in cytoskeletal organization, we examined our nanotubes for their bundling capacity. We induced bundling in the highly flexible dsOV by increasing the Mg^{2+} concentration to 20 mM, comparable to cellular concentrations, which has previously been used to bundle DNA nanotubes [96]. We observed the formation of long nanotube bundles with a width of 67.91 ± 15.47 nm (Fig. 5.12h,i, Fig. 5.21). By comparison, bundling was not seen for the semiflexible WT and iSpi designs (Fig. 5.22).

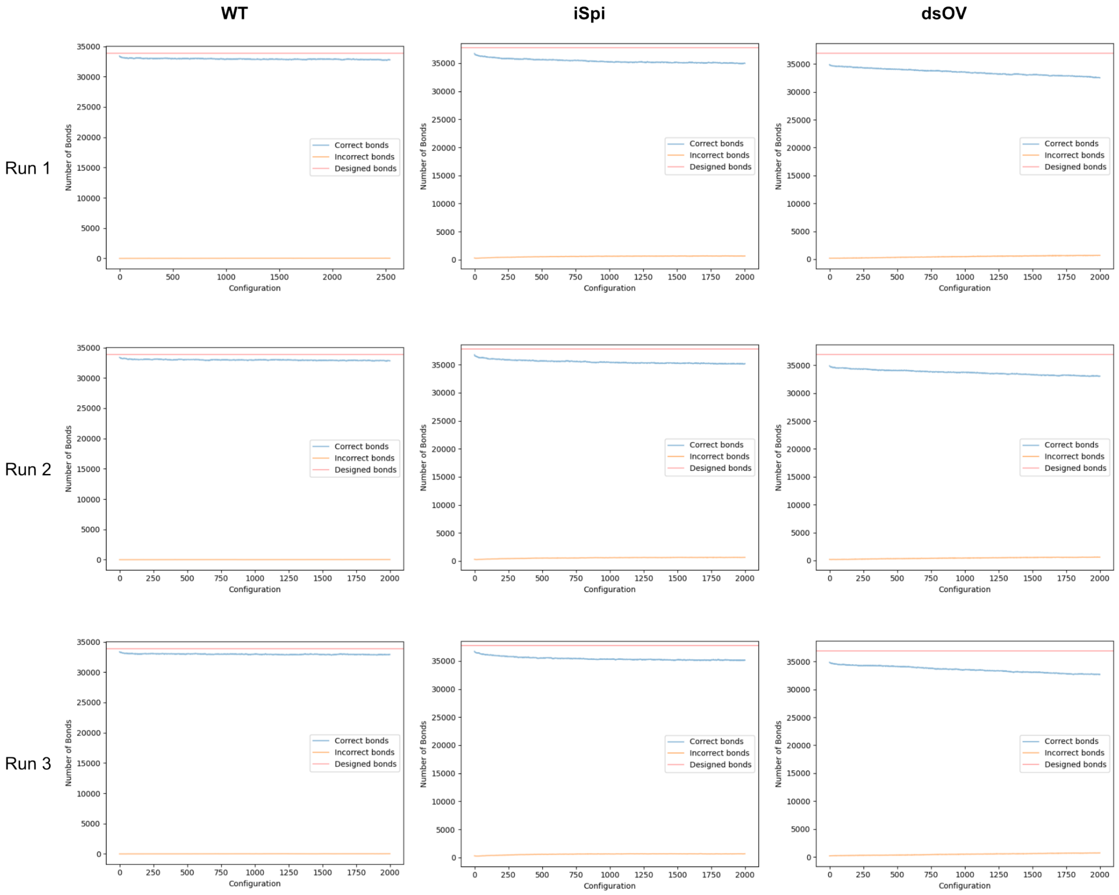

Figure 5.17: Bond occupancy compared with the target design of 300-tile RNA origami nanotubes over the course of equilibrium oxRNA simulations (1e9 steps, $dt = 0.003$). The graphs are organized by column (designs) and row (simulation run replicate). The number of correct bonds experienced a decrease at the beginning of the simulation, then remained at a constant level for WT and iSpi designs. In contrast, dsOV design exhibited a constant decrease in the number of correct bonds throughout the simulation.

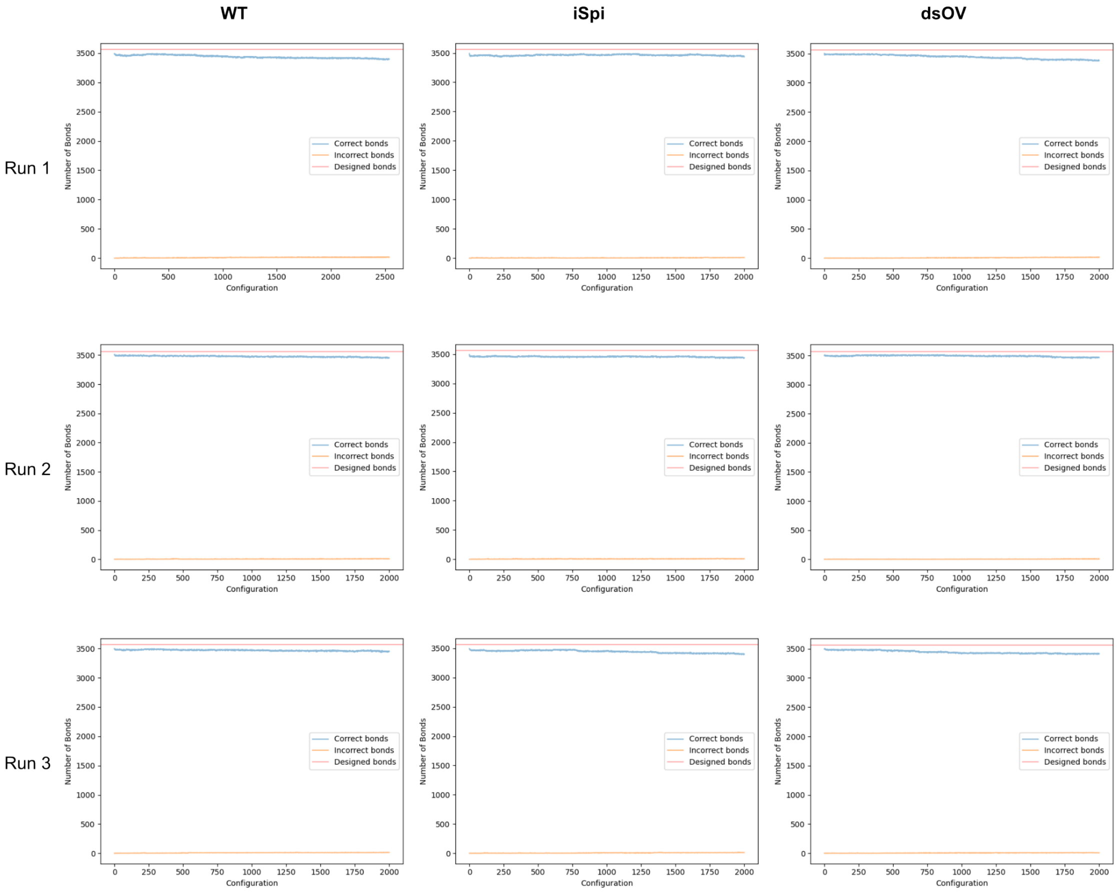

Figure 5.18: Bond occupancy in intertile kissing loops of 300-tile RNA origami nanotubes over the course of equilibrium oxRNA simulations (1e9 steps, $dt = 0.003$). The graphs are organized by column (designs) and row (simulation run replicate). Throughout the simulation, the number of correct bonds is maintained for all three designs. Note that the overall bond occupancy of the dsOV design decreases consistently (Figure 5.17), while the inter-tile bonds remain stable and correct. This indicates that bond breakage primarily occurs within the internal bonds of the tile.

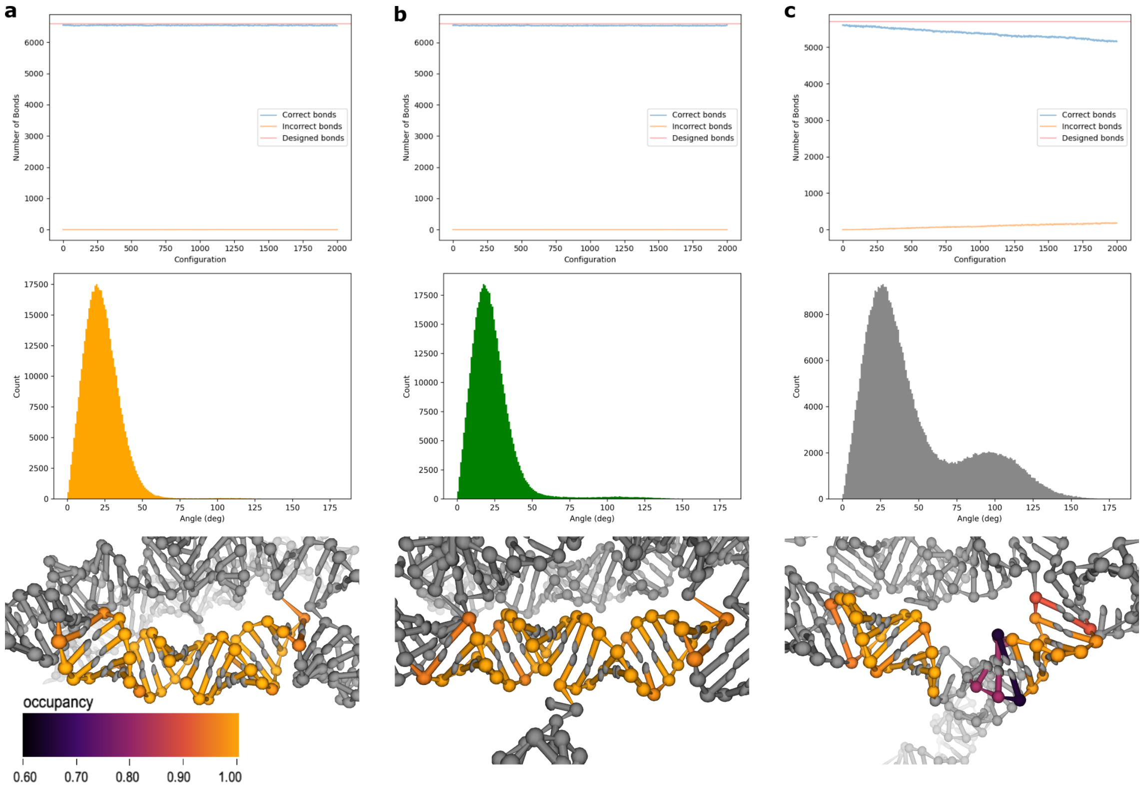

Figure 5.19: Base-pairing patterns (top, bottom) and angle across nick (middle) from oxRNA simulations of the 1 µm filament. Each column corresponds to a tile design: WT (**a**), iSpi (**b**), and dsOV (**c**). The data is for all 300 tiles in the helix (base-pairing) or for the middle 240 tiles (angles). Data from just one replicate shown here, however the pattern of both bond occupancy and angle distribution are similar for all three replicates.

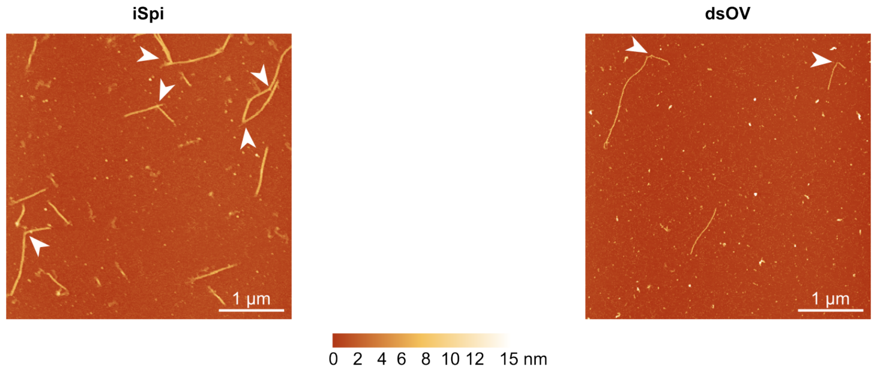

Figure 5.20: AFM micrographs of RNA origami nanotubes displaying kinks and branching (highlighted by white arrowheads) in the structure. The nanotubes are made from iSpi tiles (height channel, left) and from dsOV tiles (height channel, right).

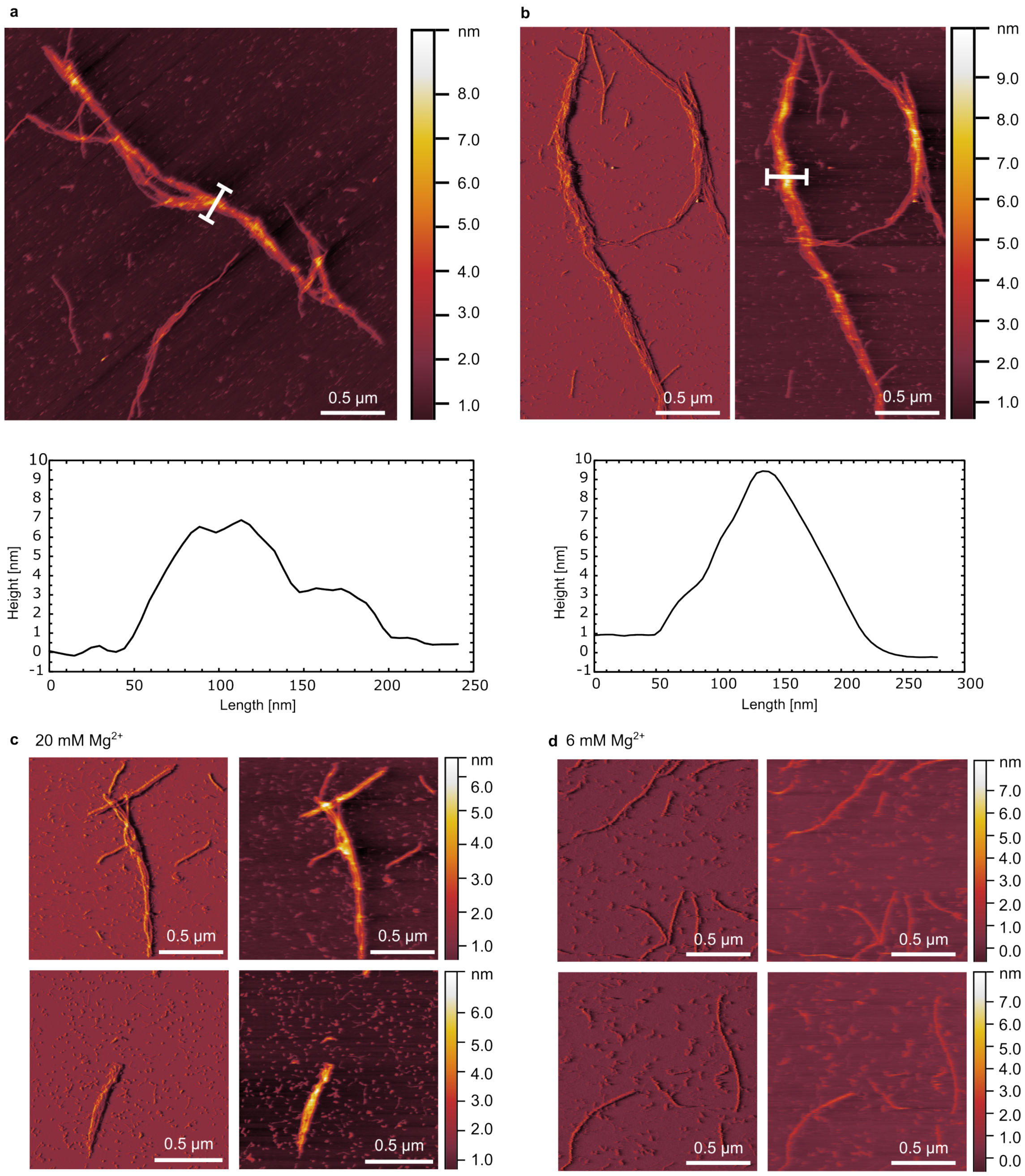

Figure 5.21: Examples of bundling of annealed RNA origami nanotubes (dsOV design) upon addition of Mg^{2+} (20 mM) as a crosslinker. **a-b)** AFM micrographs of bundled RNA origami nanotubes. **a)** shows the height channel corresponding to the AFM image in Fig. 3h. **b)** shows another RNA origami nanotube bundle. The height profiles corresponds to the height measurement along the white lines. **c-d)** AFM micrographs of RNA origami nanotubes at bundles at 20 mM Mg^{2+} **(c)** and 6 mM Mg^{2+} **(d)**. The error signal and height channel is shown on the left and right side, respectively, for **b-d**.

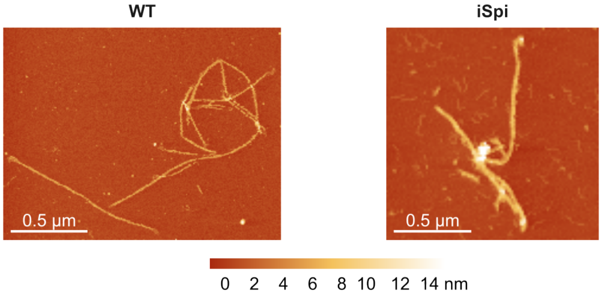

Figure 5.22: AFM micrographs of thermally annealed RNA origami nanotubes of the WT and iSpi design in 20 mM Mg^{2+} after $>$ 45 min incubation.

5.3 Persistence length analysis of RNA origami nanotubes

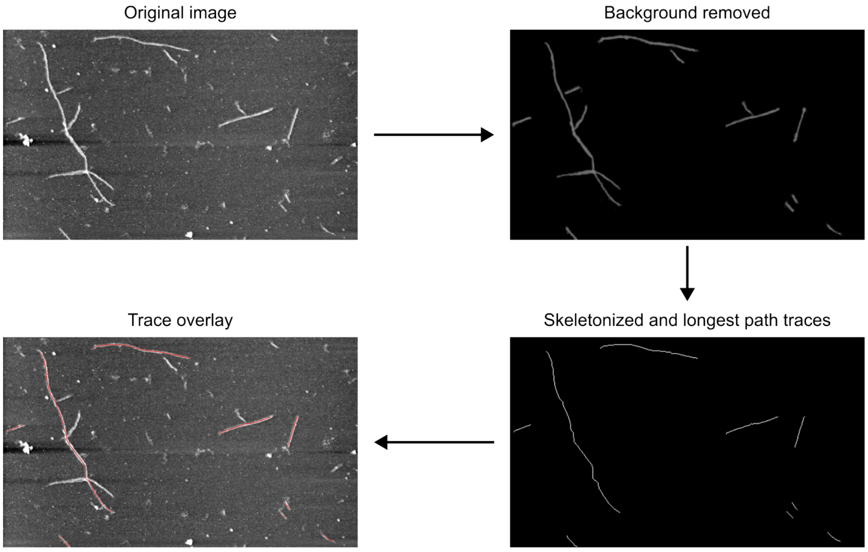

Figure 5.23: Image analysis workflow for detection of RNA nanotubes. Example of an image of RNA nanotubes from iSpi design. The AFM micrograph is first exported as a TIFF image. The background was then removed with the help of Selection Tools in Adobe Photoshop 2024. The background-removed images were then skeletonized and the longest path for each nanotube was traced (See Methods, Persistence length analysis). The traces were then exported as XY coordinates and used for contour and persistence length analysis.

Image analysis workflow for tracing RNA nanotubes is shown in Fig. 5.23. Due to the large distribution in the contour lengths of the nanotubes observed in AFM imaging, we used the mean squared end-to-end distance (MSED) method to determine persistence lengths (Fig. 5.24).

$$\langle R^2 \rangle_{3D} = 2sPL \left(1 - \frac{sP}{L} (1 - e^{-L/sP)} \right) \tag{5.1}$$

Where $\langle R^2 \rangle$ is the mean squared end-to-end distance, P is the persistence length, and L is the contour length. s is a surface parameter which is equal to 2 for a 2D surface, and 1 for 3D measurements. Since the AFM imaging is done in solution, we used $s = 1$ [226, 267].

We pooled all imaged nanotubes from 2 independent experiments, with the exception of WT+DFHBI which was only tested once (see Fig. 5.15).

For the oxRNA simulations of nanotubes, the length is limited within a small range (since all nanotubes contain exactly 300 tiles). Therefore the $\langle R^2 \rangle$ measurements were generated by measuring the distance between slices of the nanotube, where the midpoint of each slice was defined as the center of mass of the three tiles

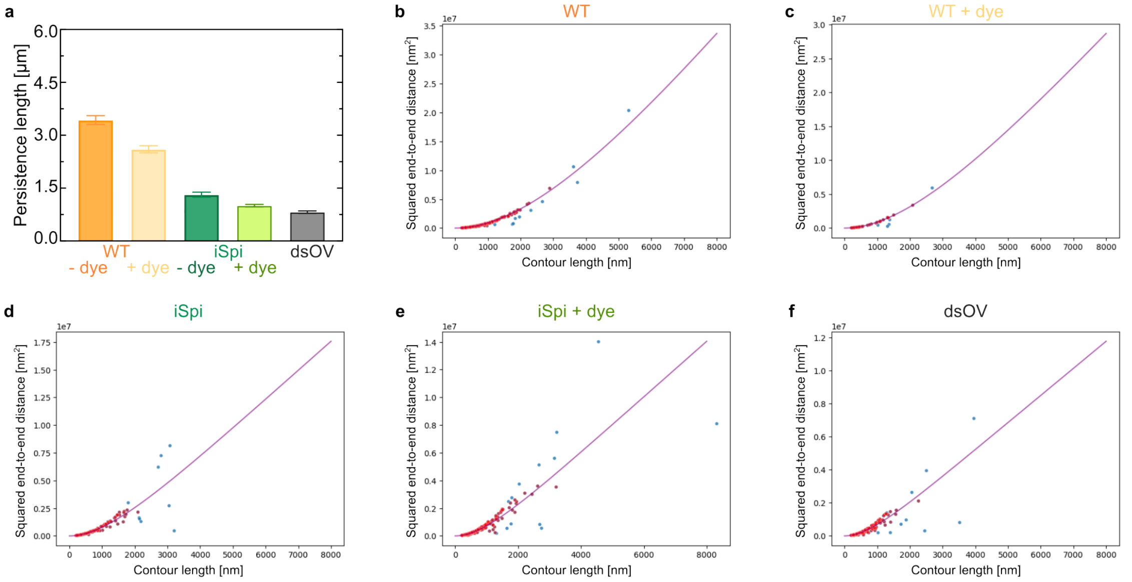

Figure 5.24: Fitting persistence length to graphs of contour length vs squared end-to-end distance. (a) Fitted persistence lengths for all tile designs (WT and iSpi with and without DFHBI dye) (fitted value ± standard error of fit) (b) WT tile (n = 141). (c) WT tile with DFHBI dye (n = 33). (d) iSpi tile (n = 124). (e) iSpi tile with DFHBI dye (n = 162). (f) dsOV tile (n = 149). Length measurement was performed using all nanotubes (blue), while the persistence length fit was done using only those points within 1 standard deviation of an initial fit (red).

that made up each layer in the nanotube. Fitting to all pairwise distance, each trajectory frame yields one persistence length and the standard error of the fit. These persistence lengths were then averaged and the standard errors were propagated and reported in Fig. 5.12g.

Note that due to experimental limitation of AFM imaging (resolution and size limit), bending of correctly assembled nanotubes cannot be distinguished from bending caused by assembly defects and regular branching. The analysis takes into account the longest path of any given nanotube regardless of the bending type. The calculated persistence length will therefore report stiffness as a result of not only the material properties but also the assembly success and branching frequency.

The persistence lengths derived from the analysis (Fig. 5.12f,g, Fig. 5.24) suggest that both steric hindrance during assembly and tile stability in assembly affect the stiffness of the nanotubes.

If an overhang was disrupting nanotube assembly for purely steric reasons, one would expect the iSpi design to show lower persistence length than the dsOV due to the larger size of the additional structure. However, we do not see this effect, suggesting that the manner of attachment—a ssRNA overhang for the iSpi versus the more rigid 3-way junction for the dsOV—has a significant impact on the ability of the tiles to assemble and the stiffness of the resulting assembly. This hypothesis is further supported by the instability of the dsOV design in oxRNA simulations, where it showed continuous loss of intra-tile bonds, specifically in the helix contain the overhang, over the course of the simulations at a much higher rate than iSpi or WT (Fig. 5.17, 5.18, 5.19). This increases the flexibility of the branched helix in the dsOV tiles compared with the other two designs (Fig. 5.19). The steric hindrance hypothesis is supported by the difference between the stiffness of the nanotubes containing overhangs to the WT design. The fact that the nanotubes often exhibit kinks and branching rather than smooth contours in AFM for iSpi and dsOV designs (Fig. 5.20) also points towards the fact that the primary source of nanotube flexibility are broken bonds, transcription errors, or incorrect incorporation of tiles during assembly. This is consistent with the higher persistence lengths measured in simulations, where the nanotubes were first forced to be perfectly formed, as opposed to the stochastic and error-prone polymerization process in experiments.

5.4 Formation of RNA origami rings

During our exploration of RNA origami nanotube designs, we identified mutations on the DNA template that consistently formed RNA origami rings rather than nanotubes. The ring-forming design used the same strand routing as WT, however with a different sequence. It also contained a single-stranded, U-rich overhang at the 5' end (hereafter, WT-mut-polyU) (Fig. 5.25a).

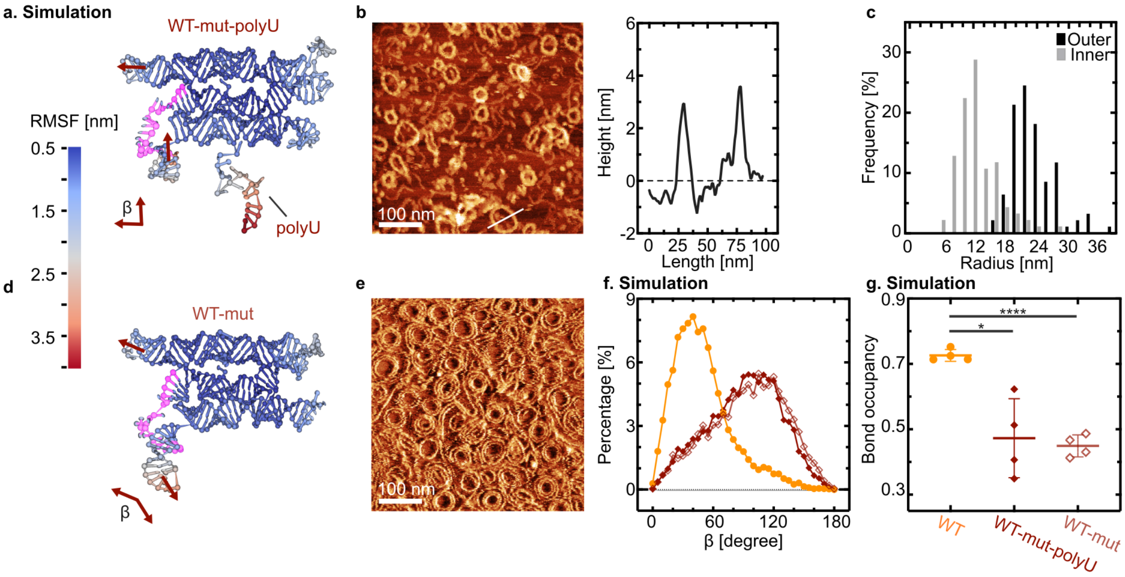

Figure 5.25: Formation of RNA origami rings. **a,d)** Coarse-grained MD simulation of a sequence-mutated WT tile (WT-mut) with (**a**) and without (**d**) single-stranded overhang polyU. All designs have GGAA starting sequence. The 12 U nucleotides 5' overhang of WT-mut-polyU was intended for binding to a fluorescent probe. β denotes the angle between the upper left and lower left duplexes as shown. The broken stem-loop in the middle left helix is highlighted in pink. The centroid structure from simulation is shown. Each nucleotide is color coded according to its RMSF. **b)** AFM micrograph and corresponding height profile of *in vitro* transcribed WT-mut-polyU RNA origami rings. The height profile is plotted along the white line. **c)** Histogram of the inner and outer radius of RNA origami rings ($n = 94$, calculated as half the Feret's diameter). **e)** AFM micrograph (lock-in phase channel) of RNA origami rings from the WT-mut tile. The corresponding height image is shown in Fig. 5.27b. **f)** Distribution of the angle β of simulated single tiles using oxRNA coarse-grained simulation (WT: orange circles; WT-mut-polyU: maroon filled diamonds; WT-mut: light-maroon empty diamonds). **g)** Bond occupancy of the stem-loop highlighted in **a,d** (mean ± s.d, n = 4 simulation runs). A parametric, unpaired t test with Welch's correction was performed. Two-tailed P values of the comparison between WT and the mutated designs are marked with **** ($p = 5.3e{-5}$), * ($p = 0.0234$). The difference is not significant among the mutated designs ($p = 0.7295$).

In oxRNA simulations, WT-mut-polyU consistently displayed misfolding in the stem-loop on the "left" side of the middle helix, which was not observed in WT, iSpi or dsOV (Fig. 5.25a, highlighted sequence, Fig. 5.26). This region in the new sequence is 50% GC compared to 75% GC in the other designs. The nanorings formed both co-transcriptionally (Fig. 5.25b) and via thermal annealing (Fig. 5.27a), indicating that the misfolding is inherent to the sequence and not a kinetic trap. Notably, the height of the ring was lower than that of the nanotubes (4 nm versus 6 nm, Fig. 5.25b) and the rings displayed a relatively homogeneous radius (23.44 ± 4.18 nm, Fig. 5.25c).

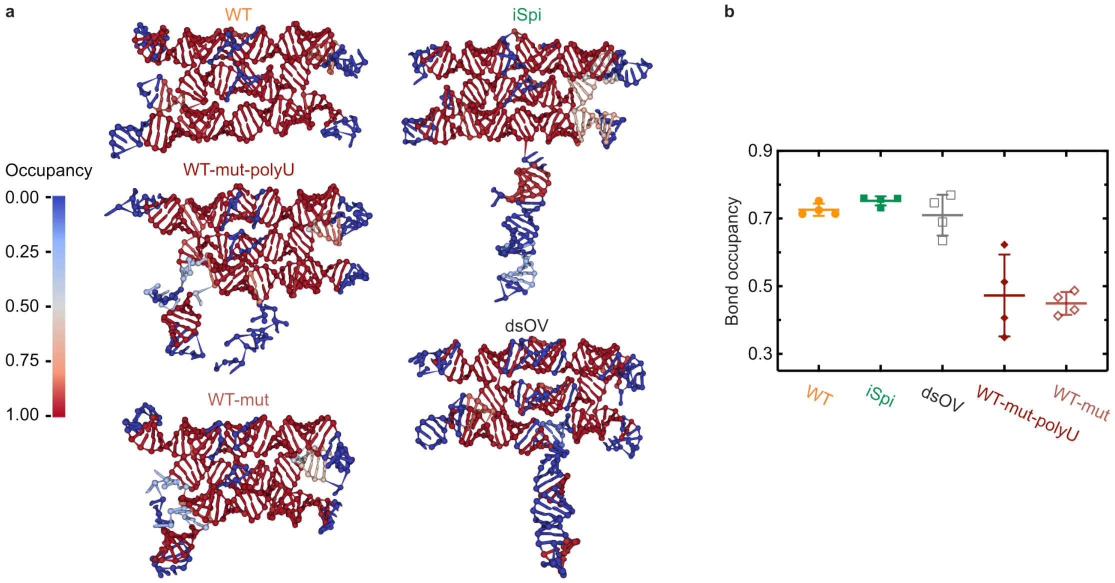

Figure 5.26: Bond occupancy of single-tile simulations. **(a)** OxRNA molecular dynamics simulations of the RNA origami tile designs. The centroid structure of the concatenated trajectory from 4 simulation runs is shown. Each nucleotide is color-coded according to its bond occupancy compared with the target design throughout the simulation. **(b)** Bond occupancy of the hairpin highlighted in Fig. 5.25 across designs (mean ± s.d, $n = 4$ simulation runs). Note that the 4-nucleotide tetraloop at the ends of the hairpin are "unpaired" in the secondary structure, thus the maximum occupancy value around 0.75. The data from Fig. 5.25g is replotted for comparison in **(b)**.

To confirm that the rings resulted from misfolding in the indicated region and not the overhang, we removed the overhang (hereafter, WT-mut). We continued to observe misfolding in oxRNA simulations (Fig. 5.25d), while in experiments, WT-mut also formed nanorings after both thermal annealing (Fig. 5.25e) and co-transcriptional folding (Fig. 5.27b). We characterized the angle, β, between the upper and lower left KL-containing duplexes of WT-mut in single-tile simulations to assess the effect of misfolding on intertile connections (Fig. 5.25a,d,e). The WT, WT-mut-polyU and WT-mut designs exhibited an angle β of 49.50 ± 28.82°, 90.61 ± 35.62°, 94.29 ± 37.23°, respectively (Fig. 5.25f). These duplexes are intended to be parallel to facilitate polymerization into a straight nanotube; however, in the mutated designs, the misfolded stem-loop shifts the distribution to a perpendicular angle between the helices, which favors assembly into rings. Bond occupancy in this region in the single-tile simulations dropped from 0.73 ± 0.02 (WT design) to 0.47 ± 0.12 and 0.45 ± 0.03 (WT-polyU-Mut and WT-mut, respectively) (Fig. 5.25g).

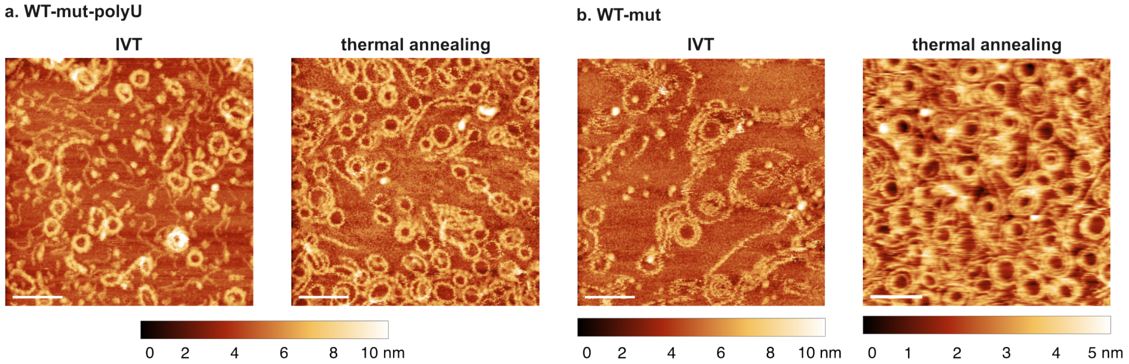

Figure 5.27: AFM micrographs of ring-forming RNA origami assembled from WT-mut-polyU tiles **(a)** and WT-mut tiles **(b)**. The RNA origami was formed by co-transcriptional folding (left, IVT) or by thermal annealing (right). The height image of the thermally annealed RNA origami ring of the WT-mut design corresponds to the micrograph in Fig.5.25. Scale bars: 100 nm.

We validated the hypothesis that ring formation is caused by opening of the stem-loop experimentally by expressing and co-transcriptionally folding WT-mut tiles at 50 mM Mg^{2+}, as divalent ion concentration enhances stiffness and hybridization in nucleic acids. As expected, the phenotype shifted towards short filaments of 3 nm in height and 81.14 ± 45.36 nm in length (Fig. 5.28). This indicates the ring formation was indeed dependent on the opening of the stem-loop. However, the length distribution peaked at 45 nm, less than half the length of an opened ring. This suggests additional intra-tile twist that hinders the growth of the filament.

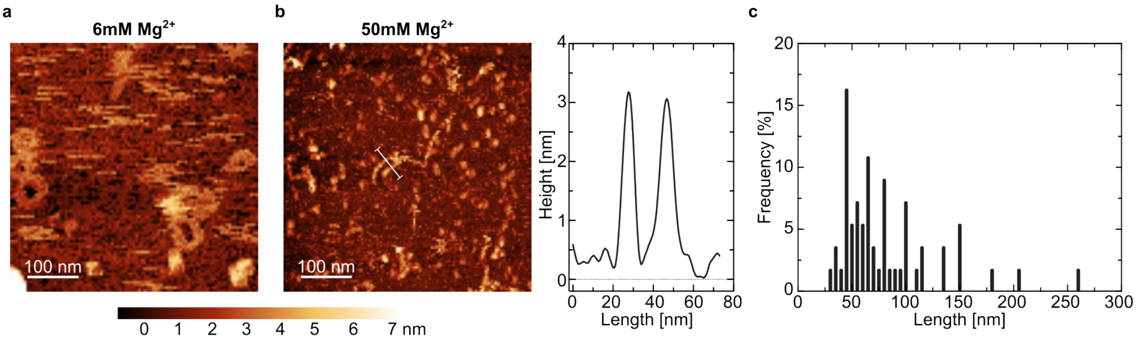

Figure 5.28: Phenotype transition from nanorings to filaments in response to Mg^{2+} concentration of WT-mut design. AFM micrographs of RNA nanostructures produced after 2 h IVT at 6 mM Mg^{2+} **(a)** and 50 mM Mg^{2+} **(b)**. The height profile of the RNA filaments at the white line is shown in **(b)**. **(c)** Histogram of the length of RNA filaments produced at 50 mM Mg^{2+} ($n = 55$ filaments).

While RNA nanorings as such have been demonstrated before [89], the rings here arise from mutations in the tile design, demonstrating phenotypic plasticity of the system. With the same RNA tile blueprint, we have two distinctly different phenotypes.

5.5 Expression of RNA origami cytoskeletons in synthetic cells

The cytoskeleton plays a crucial role in regulating cell shape and mechanics. Having built cytoskeleton-like RNA nanotubes that can fold co-transcriptionally, our next goal was to express these structures inside GUVs. Transcription of the iSpi tile inside GUVs was triggered by supplying 4 mM rNTPs externally via α-hemolysin pores and monitored with confocal microscopy, showing the appearance of a network of RNA origami nanotubes over the course of 6 h (Fig. 5.29a). Both mean fluorescence intensity (Fig. 5.29b) and area fraction of the cytoskeleton network within the GUVs increased over time (Fig. 5.29c, Fig. 5.30).

Inspired by septin, a natural membrane-binding cytoskeleton component [268], we aimed for cortex formation as the first function of our RNA cytoskeleton. To establish binding between RNA nanotubes and the vesicle membrane, we added a biotin aptamer to the iSpi tile (Fig. 5.29d, left, Fig. 5.31a). We expressed these tiles in GUVs with 5% biotinylated lipids. When transcription was triggered with rNTPs, the RNA nanotubes containing iSpinach and biotin aptamers assembled into a cortex on the inner GUV membrane (Fig. 5.29d, right). RNA origami nanotubes were exclusively observed bound to the biotinylated membrane in presence of biotin aptamer (Fig. 5.31b). Without the biotin aptamer, RNA origami nanotubes were observed in the GUV lumen as in previous experiments (Fig. 5.31c). We quantified membrane binding by calculating the center of mass of the fluorescence radial distribution in the expressing GUVs. Membrane binding results in a shift in the center of mass of the RNA fluorescence signal towards the GUV membrane (Fig. 5.29e, Fig. 5.31d,e). Interestingly, continuous supply of nucleotides resulted in high expression levels in some GUVs, which, in turn, caused GUV deformation both with and without biotin aptamers (Fig. 5.29f, Fig. 5.32, 5.33, 5.34). Note that due to the stochasticity of the GUV encapsulation process of polymerase, DNA template or nanopores, deformation is observed in only about 5% of the RNA nanotube-producing GUVs, but never in non-expressing GUVs (Fig. 5.35).

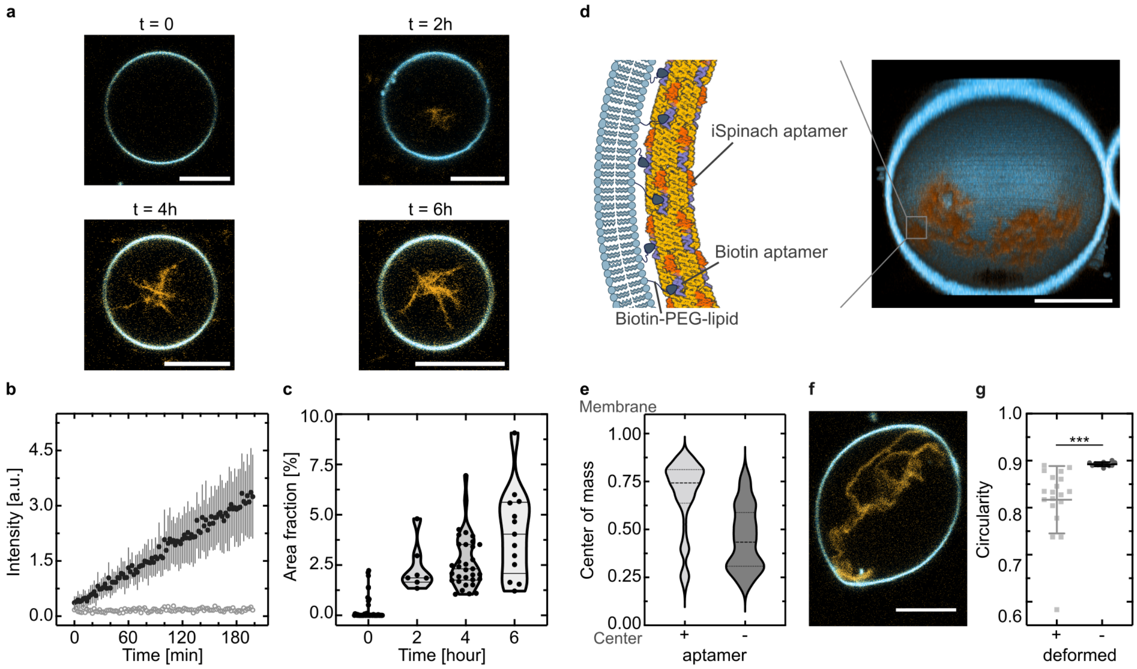

Figure 5.29: Expression of RNA origami cytoskeletons in synthetic cells. **a)** Confocal time series of cytoskeleton-like iSpi RNA origami nanotubes (orange, $\lambda_{ex} = 488\,\text{nm}$) expressed inside a GUV (blue, membrane labelled with DiD, $\lambda_{ex} = 640\,\text{nm}$). Scale bars: 10 µm. **b)** RNA nanotube transcription inside of GUVs triggered by addition of rNTPs plotted over the first 3 h of expression (mean ± s.d, $n = 6$ GUVs). The data was extracted from confocal fluorescence timelapse recordings. Background fluorescence outside of the GUVs is plotted as gray circles. **c)** Area fraction occupied by the RNA origami nanotubes plotted over time (n = 50, 6, 32, 12 GUVs, left to right). **d)** Cortex formation with RNA origami nanotubes on the inner GUV membrane. Left: Schematic representation of an RNA origami nanotube adhering to the biotinylated GUV membrane via a biotin aptamer attached to the iSpi tile [157]. Right: Confocal 3D reconstruction of an RNA origami cortex on the inner GUV membrane after its expression. Scale bar: 10 µm **e)** Distribution of RNA nanotubes with or without the biotin aptamer inside of the GUV. The distribution of the center of mass of the iSpi fluorescence relative to the GUV center is plotted ($n = 78$ (+) and 87 (-) GUVs, median: dashed lines, first and third quartile: dotted lines). **f)** GUV deformation caused by biotin aptamer-functionalized RNA origami nanotubes. Scale bar: 10 µm. **g)** Quantification of GUV deformation. The circularity of deformed GUVs ($n = 19$) and GUVs not expressing nanotubes ($n = 12$) are plotted (mean ± s.d). A parametric, unpaired t test with Welch's correction was performed. Two-tailed P value is marked with *** (p = 0.0002).

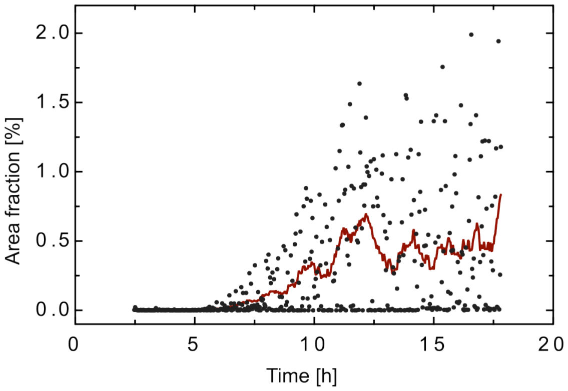

Figure 5.30: Tracking of RNA origami nanotube growth inside a single GUV after rNTP triggering. The area fraction is plotted over time (2 min interval). Fluctuations of the area fraction are inevitable due to the constant Brownian diffusion of the RNA origami nanotubes in and out of the focus plane. The red line is drawn to guide the eye, obtained by curve smoothing in Prism (Version 10.2.3) using 10 neighbors on each side with 0th order smoothing polynomial. The area fraction was extracted from a confocal time series using similar method as in Fig. 5c. The GUV detection and measurements were done automatically using a custom-written code (see Code availability). The data was then filtered using a custom-written Python code (see Code availability).

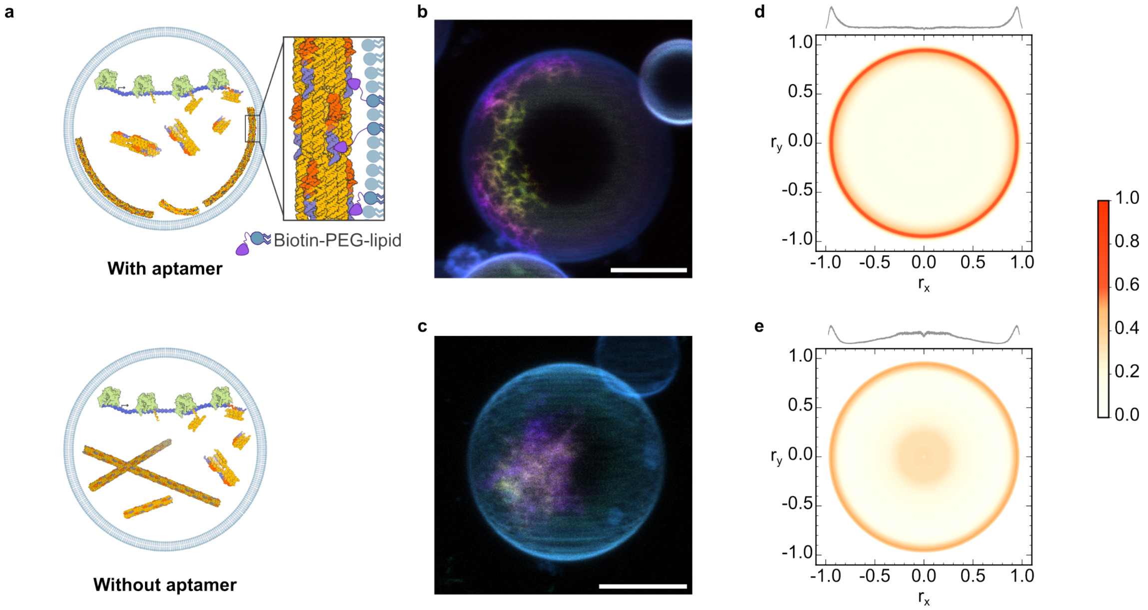

Figure 5.31: Functionalized RNA origami nanotubes for membrane binding. **a)** Schematic representation of the biotin-aptamer containing RNA origami nanotubes for binding to biotinylated GUV membranes. **b-c)** Confocal z-stack projections of biotin-aptamer containing **(b)** and aptamer-free **(c)** iSpi RNA origami nanotubes inside a GUV. **(b)** shows the z-projection of the image presented in Fig. 5d. The membrane is labelled with DiD (λ_{ex} = 640 nm, blue). The RNA origami z-projection is colour coded. **d-e)** Radial fluorescence distribution of the RNA origami nanotubes with **(d)** (n = 78) and without biotin aptamer **(e)** (n = 87) inside the GUVs. Membrane binding is indicated by a shift in the center of mass of the radial RNA fluorescence signal towards the biotinylated membrane. Scale bars: 10 µm.

We quantified this deformation by measuring the circularity of the deformed GUVs compared to non-expressing control GUVs (Fig. 5.29g). The deformation is statistically significant, reducing the circularity to a mean value of 0.8. Deformation happens primarily along the axis of the RNA-origami cytoskeleton inside the GUV (examples of deformed GUVs shown in Fig. 5.32, 5.33, 5.34), suggesting an active deformation by polymerization rather than osmotic deflation. Osmolarity changes during the experiment are negligible (within μM range). The deformed GUVs were pre-encapsulated with DNA templates and T7 polymerase (see Method). The DNA template solution was in water with a concentration of 4-8 ng μL^{-1} which is equivalent to 20-40 nM (the DNA template is 220-250 kDa). The T7 polymerase is stored in 50 mM Tris-HCl (pH 8.0), 150 mM NaCl, 5 mM DTT, 0.1 mg mL^{-1} BSA, 0.03% (v/v) ELUGENT Detergent and 50% (v/v) glycerol. The T7 solution is diluted 50 to 250 times when added to the GUV solution. Those components that cannot go through the α-hemolysin are T7 polymerase and BSA which are both at μM concentration. The T7 concentration is (0.2 U μL^{-1} to 1 U μL^{-1}) which results in 2.4 mM to 12 mM of rNTP incorporation in 12 h at 37 °C. This results in an RNA tile concentration of 6 μM to 35 μM after 12 h of transcription in GUVs. Overall, due to the presence of α-hemolysin, as well as the millimolar concentration of salt and sucrose, the osmolarity of the inner solution fluctuates a negligible amount, preventing osmotic shock. Note that the osmolarity of the outer solution is kept constant against evaporation by sealed chambers and sealed reaction tubes.

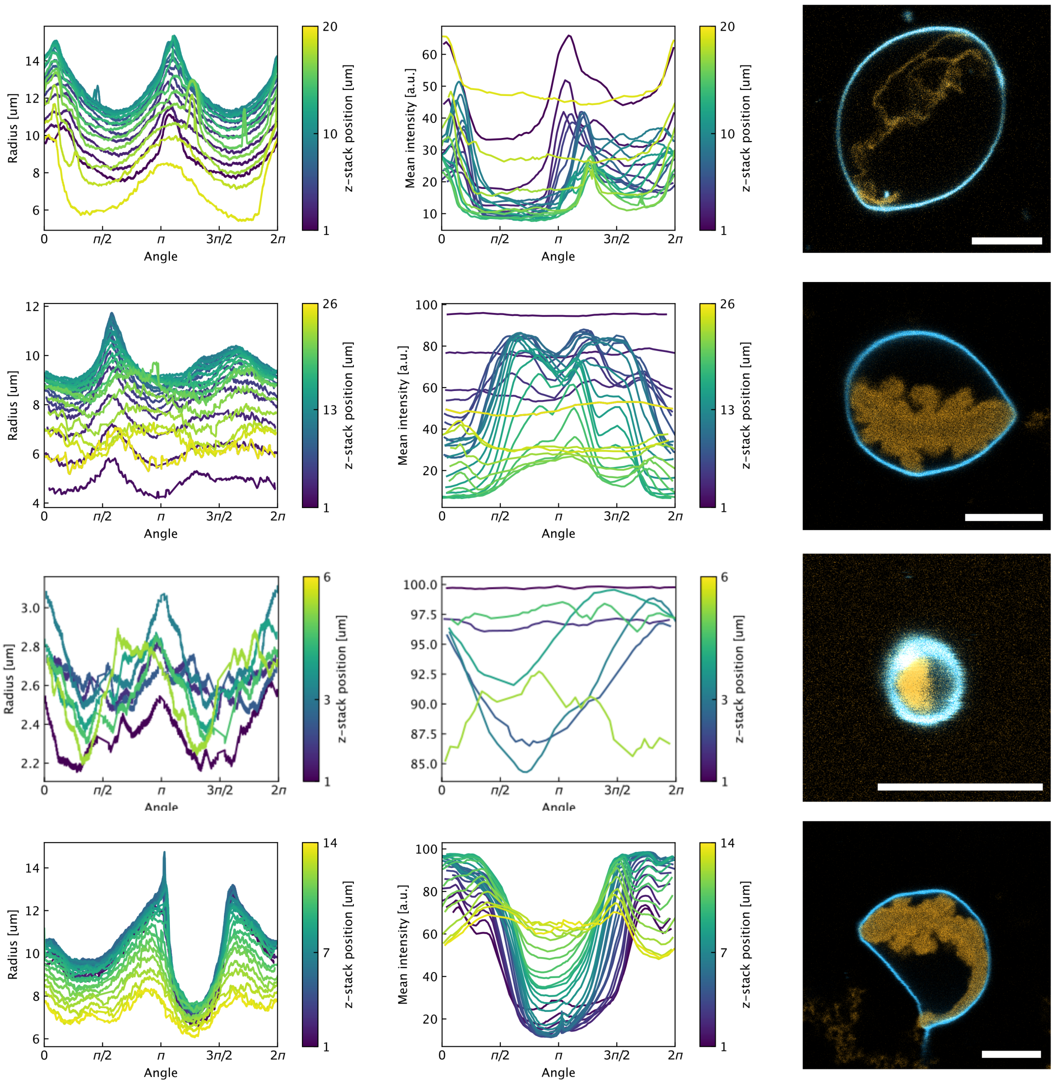

Figure 5.32: Analysis of confocal z-stacks of multiple deformed GUVs ($n = 4$). Deformation is caused by the production of RNA origami nanotubes with biotin aptamers inside the GUV. **Column 1-2:** Angular distribution of the GUV radii and RNA fluorescence signal, respectively, over the perimeter of the GUV. The analysis was done over all z-stacks. **Column 3:** RNA nanotube-expressing GUVs were incubated for 6 h to 8 h prior to imaging. The membrane is labelled with DiD ($\lambda_{ex} = 640\,\text{nm}$) shown in blue and RNA nanotube ($\lambda_{ex} = 488\,\text{nm}$) shown in orange. Scale bars: 10 µm. Peaks represent the maximum distance from the center, corresponding to membrane deformations caused by the RNA nanotubes. For example, lemon-shaped deformed GUVs show two peaks (angular distance between the two peaks = π), whereas one-sided elongated GUVs exhibit a single peak, and non-deformed, round GUVs display no peaks (see Fig 5.35). Deformation is more pronounced in the middle of the Z-stack compared to higher and lower Z-stack positions.

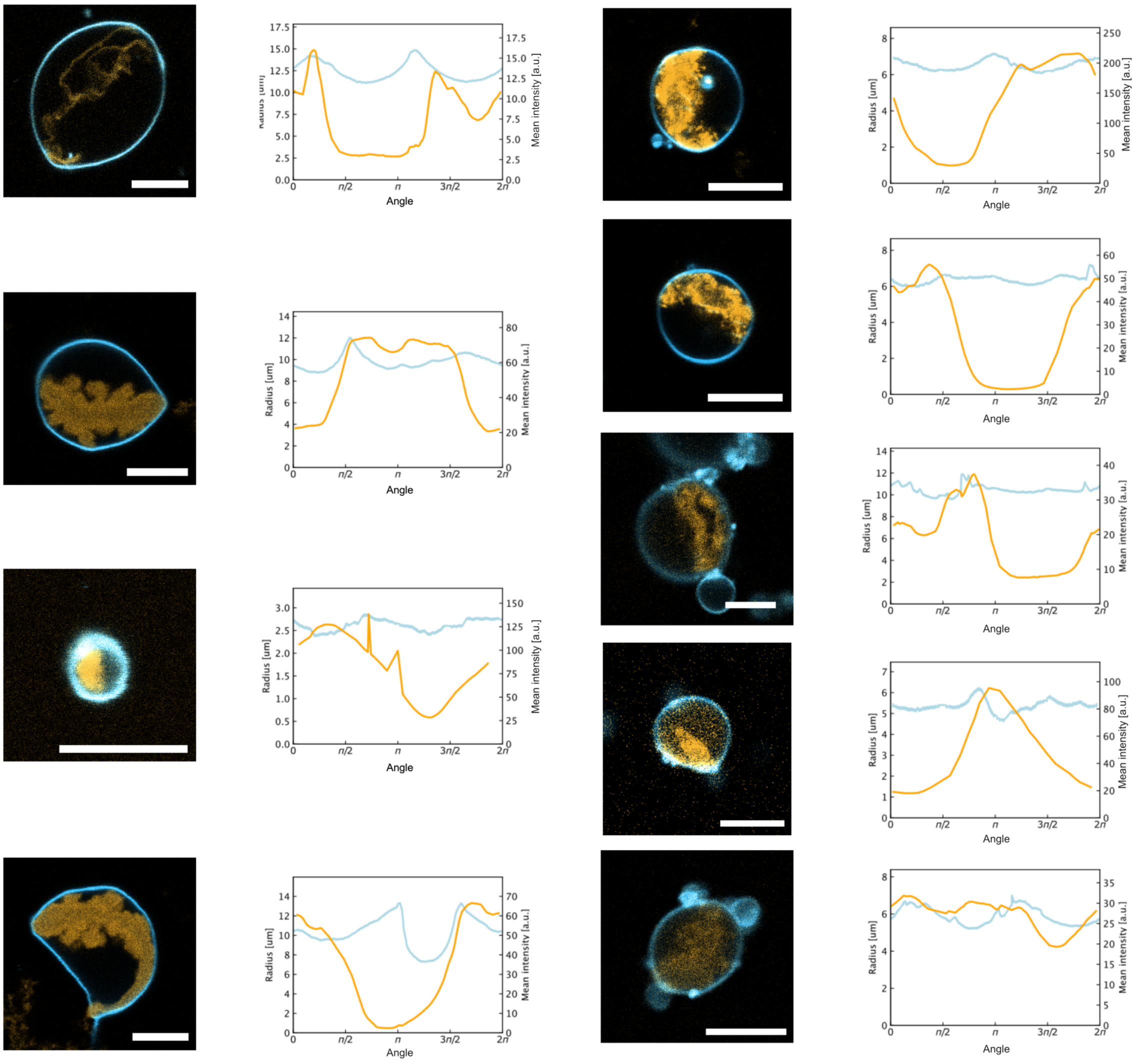

Figure 5.33: Deformation of GUVs containing RNA origami nanotubes with biotin aptamers. Confocal images of multiple deformed GUVs ($n = 9$) and corresponding angular distribution of GUV radii (blue) and RNA intensities (orange) over the GUV perimeter. GUVs were incubated with all transcription components, including rNTPs, at 37 °C for 6 h to 8 h prior to imaging. The angular distributions are plotted from a 2D plane of a single GUV image. Scale bars: 10 µm.

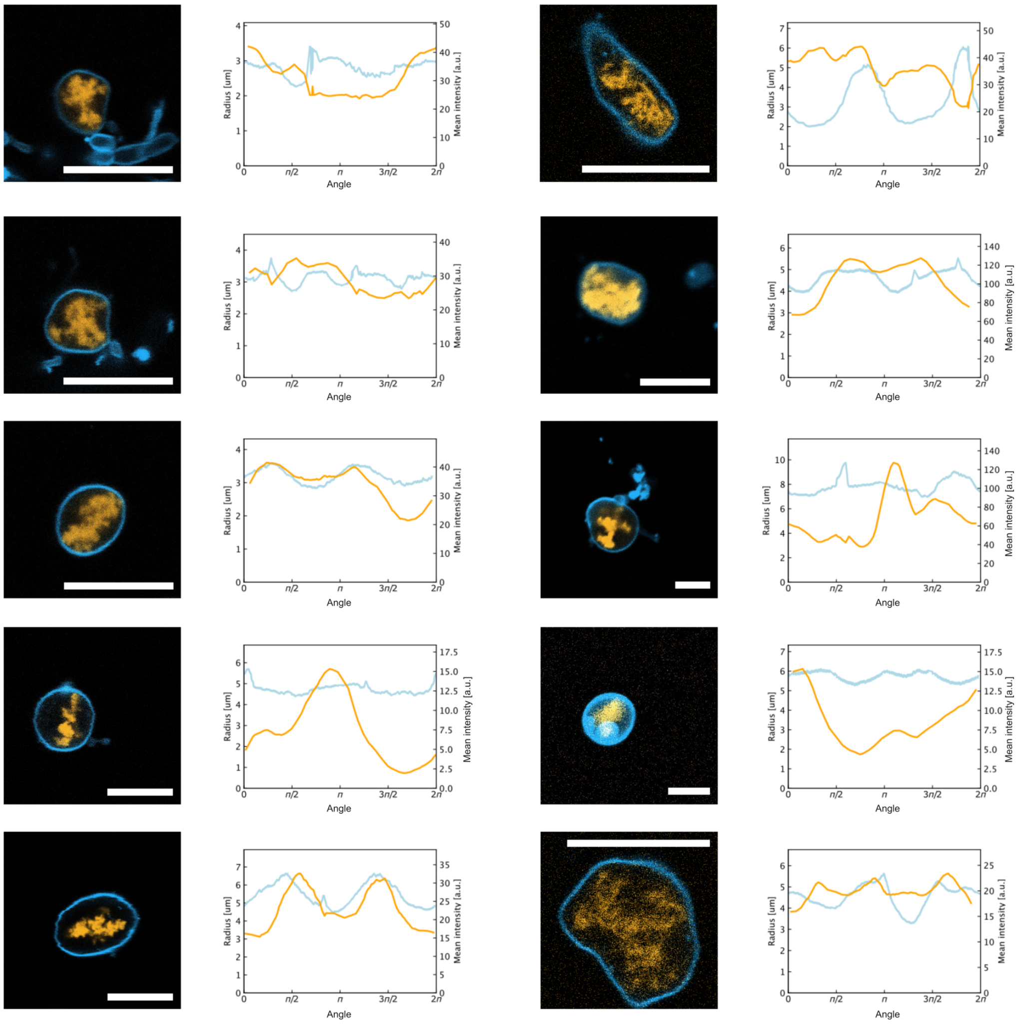

Figure 5.34: Deformation of GUVs containing RNA origami nanotubes without biotin aptamers. Confocal images of multiple deformed GUVs (n = 10) and corresponding angular distribution of GUV radii (blue) and RNA intensities (orange) over the GUV perimeter. GUVs were incubated with all transcription components, including rNTPs, at 37 °C for 6 h to 8 h prior to imaging. The angular distributions are plotted from a 2D plane of a single GUV image. Scale bars: 10 µm.

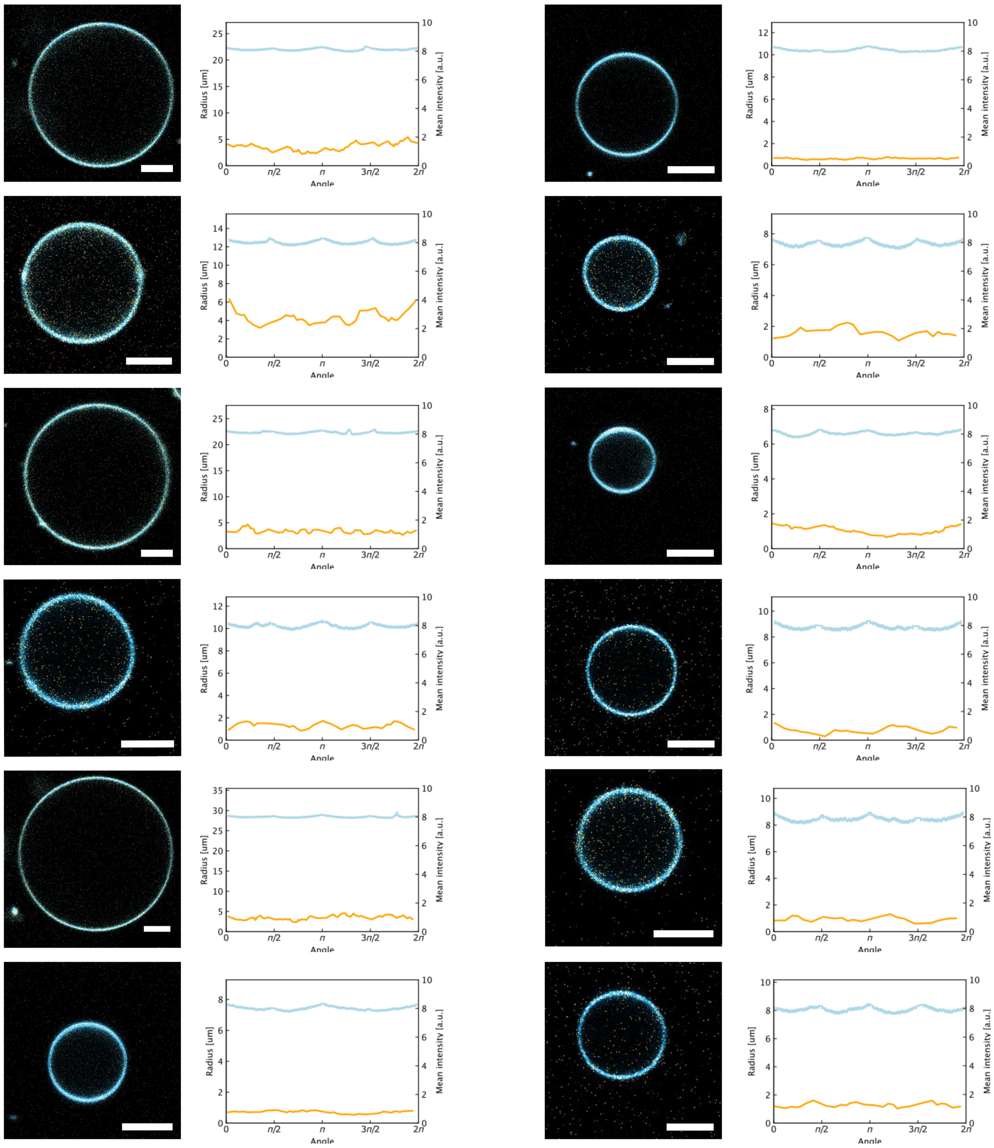

Figure 5.35: Undeformed GUVs in the absence of RNA origami nanotube formation within the GUV compartments. Confocal images of multiple undeformed GUVs ($n = 12$) and corresponding angular distribution of GUV radii (blue) and RNA intensities (orange) over the GUV perimeter. GUVs were incubated with all transcription components, excluding rNTPs. The angular distributions are plotted from a 2D plane of a single GUV image. Scale bars: 10 µm. No peaks were observed in the round GUVs, indicating the absence of deformation.

5.6 Discussion

Here we provide a conceptual framework for the construction of synthetic cells based on the expression of RNA origami inside of lipid vesicles. Compared to DNA origami, RNA is genetically encodable, which means that the synthetic cells can produce their own building blocks in an active, out-of-equilibrium process. This makes the approach different from the mere encapsulation of DNA origami structures. Additionally, we have shown that we can incorporate functionality, like membrane binding, using RNA aptamers instead of covalent modification with e.g. cholesterol needed on DNA structures. Finally, subtle changes to the design, like simply swapping out overhanging sequences or weakening specific helices, can result in substantial morphological changes, hinting towards exciting prospects for directed evolution approaches. Compared to proteins, RNA origami expression in GUVs required far fewer biologically-derived components—only T7 polymerase compared to the entire transcription-translation machinery with over 150 genes. This could mean that the realization of a self-sustained chemical system capable of evolution becomes more accessible [12, 269]—although this remains speculative for now and diverse scientific communities may, one day, realize diverse variants of synthetic cells.

We expect future RNA origami-based hardware to incorporate ribozymes for the realization of molecular machines which execute complex cellular tasks. From a more fundamental point of view, the study of ribozyme activity in confinement has been shown to deviate from bulk activity [270, 271], which hints towards exciting prospects for active RNA origami in vesicles. Additionally, it will be interesting to develop methods to copy the DNA template, e.g. by templated ligation [272], and the use of polymerase ribozymes [273] instead of T7 for RNA production or direct self-replication of RNA origami. Notably, the construction of synthetic cells based on co-transcriptional RNA origami is inherently compatible with evolution and AI-guided design, which allows orders of magnitude higher throughput and design testing compared to traditional rational engineering approaches. This will increase the functional complexity of synthetic cells, while at the same time, incorporating evolution, as a fundamental characteristic of life, into the design process itself. From a practical point of view and beyond synthetic life, genetically encodable hardware made from RNA origami may lead to new exciting biophysical tools to manipulate cells and to address questions in cell biology.

5.7 Integration of nucleic acid droplets to a synthetic cytoskeleton

Inspired by how natural cytoskeletons interface with membraneless organelles, we explored similar interactions in synthetic systems using nucleic acid components. We first coupled DNA droplets with DNA nanotubes [68] via connector strands that bridges their sticky ends. When co-annealed, this produced DNA droplets with localized clustered nanotubes (Fig. 5.36), whereas in the absence of the connector, the two components remained spatially separated (Fig. 5.36). To move toward *in situ* expression of the system, we translated this concept to RNA. When co-expressed

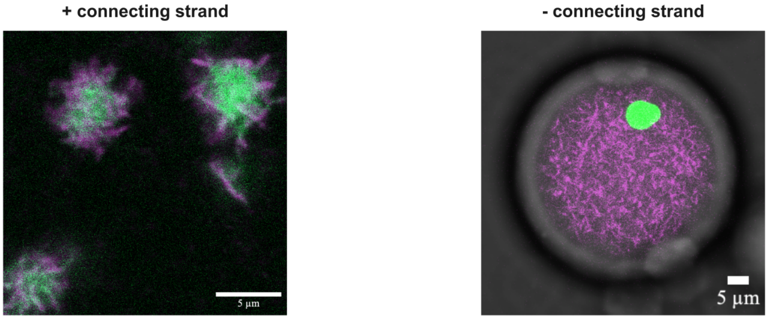

Figure 5.36: Preliminary data: DNA droplet in connection with DNA tiles. Confocal overlay of brightfield and confocal images showing DNA droplet (green) annealed together with DNA tiles (purple) in presence of connecting strands in bulk (left) and without connecting strands inside water-in-oil droplets (right). Connecting strand sequences are: GCTCGAGCTTATGGA and GTCTGTTGCTCGAGC. The DNA droplets and DNA nanotubes were labeled with ATTO-488 ($\lambda_{ex} = 488\,\text{nm}$) and ATTO-647N ($\lambda_{ex} = 640\,\text{nm}$) respectively. Scale bars: 5 µm.

with RNA droplets, the RNA nanotubes interacted with the droplet surface, forming an exoskeleton-like shell (Fig. 5.37). This exoskeleton prevented fusion between droplets. Even though unspecific, this interaction demonstrates how RNA-origami structural elements can modulate the material properties of RNA condensates. Interestingly, RNA droplets are shown to be capable of encapsulating DNA templates [180], suggesting a route toward integrating compartmentalization, structural organization, and genetic control. The ability of the RNA cytoskeleton to interact and stabilize droplet morphologies could, in principle, be extended to regulate droplet

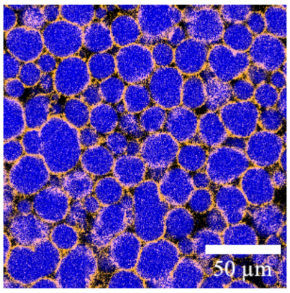

Figure 5.37: Co-transcribed RNA droplet with RNA-origami cytoskeleton. Confocal images showing RNA droplet (blue) coated with RNA-origami cytoskeleton (orange) after overnight co-transcription in RNA droplet transcription condition [178]. Both RNA was transcribed using the same T7 promoter as the RNA-origami cytoskeleton and at a DNA template concentration of $1.5\,\text{ng}\,\mu\text{L}^{-1}$ each. RNA droplet design was adapted from droplet A design in [178]. Fluorescence visualization was achieved by including an iSpinach aptamer and DFHBI-1T dye for RNA-origami cytoskeleton and Malachite Green aptamer and Malachite Green ($\lambda_{ex} = 488\,\text{nm}$, $\lambda_{ex} = 640\,\text{nm}$, respectively). Scale bar: 50 µm. Experiment was done by William Verstraeten.

fission, akin to a primitive cytoplasmic division scaffold. I envision this integration as a key step in realizing evolvable synthetic cells that coordinate the spatial arrangement, mechanical stability, and segregation of their genetic components, all encoded in nucleic acid sequences. This coupling of phase-separated RNA compartments with RNA cytoskeletons exemplifies how the two central components of this thesis: DNA segregation and the expression of functional architectural elements can be combined to support evolvable synthetic cell behavior.

6

Conclusion and Outlook

This thesis set out to explore how genetically encoded architectures made from DNA and RNA can lay the groundwork for evolvable synthetic cells. Guided by the principle that evolution is the defining property for bottom-up construction of life, this work focused on implementing genotype–phenotype coupling in minimal systems where both information and function are encoded in heritable substrates and expressed as selectable behaviors. To that end, this thesis demonstrated two complementary systems: a DNA segregation module enabling spatial partitioning of genetic material within confined compartments, and a genetically encoded RNA origami cytoskeleton that is produced *in situ* and co-transcriptionally assembles into membrane-interacting nanotubes. These systems use nucleic acid nanostructures to produce microscale behaviors from sequence-level design, bridging the molecular and cellular scales. Together, they move us toward synthetic cells where structure and function are coupled to genetically mutable templates, opening the door to evolution.

The DNA droplet system addressed a long-standing gap in synthetic cell division—namely, the controlled segregation of informational content. Using liquid-liquid phase separation of sequence-programmable DNA nanostars, we implemented enzymatic and photo-induced fission mechanisms to induce full spatial segregation of DNA condensates. Importantly, we showed that the behavior of these condensates, including segregation speed and spatial organization, depends on confinement, ionic environment, and sequence-encoded flexibility. Our lattice-based model further underscored the role of local interactions and boundaries, laying groundwork for predictive design of segregation phenotypes. This work lays the groundwork for using nucleic acid condensates and their biophysical properties as phenotypically visible, selectable architectures for cellular inheritance such as spatial segregation.

The second part of this thesis focused on expressing RNA-based cytoskeletal architectures directly from DNA templates inside synthetic cells. RNA origami tiles were rationally designed to fold co-transcriptionally and self-assemble into micrometer-scale nanotubes, forming genetically encoded cytoskeletal networks under isothermal conditions. The physical properties of these structures—such as stiffness and bundling capacity—were tunable via sequence design. By appending aptamers, membrane binding and cortex formation were achieved, and in some cases, high expression levels induced visible deformation of the lipid vesicle itself—demonstrating a direct, genetically encoded microscale phenotype. Notably, minor sequence variations produced stark phenotypic differences, such as nanorings instead of nanotubes, highlighting the system's potential for evolvability. Coarse-grained molecular dynamics simulations of the RNA-origami cytoskeleton at microscale reinforced the genotype–structure–function link, while highlighting the role of sequence-dependent flexibility in guiding cytoskeletal phenotype.

Taken together, these two studies converge on a central message: functional behavior in synthetic cells—whether it be inheritance or internal structuring—can be achieved using only DNA and RNA. More than that, these behaviors can be encoded genetically and regulated externally, making them amenable to mutation, selection, and ultimately, evolution.

Outlook

Looking ahead, several exciting directions emerge:

First, integration: Preliminary data has shown the potential of using DNA and RNA-based nanotubes in conjunction with nucleic acid droplets, but their full integration remains unexplored. A compelling future direction is to investigate whether droplets can serve as organizing centers for the cytoskeletons—analogous to centrosomes in natural cells—or whether RNA-based cytoskeletons can aid or regulate DNA segregation. DGiven that RNA droplets can sequester DNA templates, they might also be repurposed as scaffolds for DNA segregation. Additionally, the RNA cytoskeleton, acting as an exocytoskeletal element around RNA droplets, may help promote division of RNA-based protocells. However, to enable such functionalities, catalytic activity embedded within the RNA cytoskeleton would likely be essential, highlighting the next direction: introducing out-of-equilibrium processes.

Second, out-of-equilibrium: Although the synthesis of the RNA origami cytoskeleton is inherently out-of-equilibrium by consuming rNTPs during transcription, the systems in this thesis are otherwise passive once assembled. Moving forward, integrating RNA/DNA catalysis using ribozymes or DNAzymes into condensates or cytoskeletal scaffolds could enable internal reaction cycles, active remodeling, and energy dissipation. This opens a path toward metabolic coupling and non-equilibrium behaviors. For example, the RNA origami cytoskeleton described here polymerizes bi-directionally and at equilibrium. Directionality in polymerization could be programmed by introducing conformational asymmetries in the monomer subunits. Ribozymes could also be incorporated to trigger conformational changes of the monomer upon assembly, and thereby promoting their depolymerization and return to solution. Together, these mechanisms could enable a dynamic, out-of-equilibrium cycle of directional assembly and turnover, analogous to the dynamics of natural cytoskeletons. In parallel, ribozyme-powered RNA walkers could be developed to transport molecular cargo along cytoskeletal filaments. While these functions can be designed rationally, the inherent evolvability of the system means that new and unforeseen behaviors could also emerge through selection.

Third, evolution: With phenotypic diversity now demonstrated to be sequence-dependent, a logical next step is to experimentally implement variation–selection cycles within synthetic cells. Directed evolution within vesicles, guided by external stimuli or by morphology-based selection, could uncover novel, emergent architectures.

Importantly, the RNA cytoskeleton's ability to modulate compartment shape and stability suggests a potential route to evolve not just internal structure but also compartment division. When coupled with programmable droplet segregation, this could enable coordinated inheritance of both structural and genetic material. As individual synthetic cells become more complex, so too does the possibility of collective behaviors. DNA or RNA motifs could be used to encode not just internal structures, but also cell–cell interactions: via droplet fusion, strand exchange, or chemical signaling. These modes of interaction could support population-level selection, opening the door to multicellular synthetic systems.

Fourth, autonomy: While this work focused on expression and organization, replication of the genetic material itself remains outsourced. Introducing autonomous replication mechanisms—such as ligase cycles, polymerase ribozymes, or minimal enzymatic systems—would enable synthetic cells to regenerate their genetic content. Achieving this would complete the feedback loop required for autonomous evolution.

Finally, the results in this thesis open a broader philosophical and technological conversation. In showing that cellular functions can emerge from nucleic acid structures, we progress closer to creating systems that are not merely engineered but evolvable. Synthetic cells built on the principles explored here may not just model life but also become substrates for new forms of life.

Appendices

Abbreviations

2D two-dimensonal
3D three-dimensonal

AFM atomic force microscopy

CLSM confocal laser scanning microscopy

DNA deoxyribonucleic acid
DNAzyme deoxyribozyme
DOPG 1,2-dioleoyl-sn-glycero-3-phosphoglycerol
DOPC 1,2-dioleoyl-sn-glycero-3-phosphocholin

GUV giant unilamellar vesicle

HFE hydrofluorether

LLPS liquid–liquid phase separation

MCS monte carlo step

NASA national aeronautics and space administration

PCR polymerase chain reaction
PEG polyethylene glycol
PFPE perfluorpolyether
POPC 1-palmitoyl-2-oleoyl-sn-glycero-3-phosphocholin
POPG 1-Palmitoyl-2-oleoyl-sn-glycero-3-phosphatidylglycerol

RNA ribonucleic acid
rNTP ribonucleotide tri-phosphate

SUV small unilamellar vesicle

WOD water-in-oil droplet

"Your knowledge can never be taken away from you."
Julius Fichtler

A

List of Publications

Publications

(* equal contribution)

1. **Mai P Tran**, Rakesh Chatterjee, Yannik Dreher, Julius Fichtler, Kevin Jahnke, Lennart Hilbert, Vasily Zaburdaev, Kerstin Göpfrich; 'A DNA segregation module for synthetic cells', *Small* (2022) `https://doi.org/10.1002/smll.202202711`

2. Xenia Tschurikow*, Aaron Gadzekpo*, **Mai P Tran**, Rakesh Chatterjee, Marcel Sobucki, Vasily Zaburdaev, Kerstin Gopfrich, Lennart Hilbert; 'Amphiphiles formed from synthetic DNA-nanomotifs mimic the stepwise dispersal of transcriptional clusters in the cell nucleus', *Nano Lett.* (2023), `https://doi.org/10.1021/acs.nanolett.3c01301`

3. Kevin Jahnke*, Maja Illig*, Marlene Scheffold, **Mai P Tran**, Ulrike Mersdorf, Kerstin Göpfrich; 'DNA origami signaling units transduce chemical and mechanical signals in synthetic cells', *Adv. Funct. Mater.* (2023), `https://doi.org/10.1002/adfm.202301176`

4. Christine ME Kriebisch, Olga Bantysh, Lorena Baranda Pellejero, Andrea Belluati, Eva Bertosin, Kun Dai, Maria de Roy, Hailin Fu, Nicola Galvanetto, Julianne M Gibbs, Samuel Santhosh Gomez, Gaetano Granatelli, Alessandra Griffo, Maria Guix, Cenk Onur Gurdap, Johannes Harth-Kitzerow, Ivar S Haugerud, Gregor Häfner, Pranay Jaiswal, Sadaf Javed, Ashkan Karimi, Shuzo Kato, Brigitte AK Kriebisch, Sudarshana Laha, Pao-Wan Lee, Wojciech P Lipinski, Thomas Matreux, Thomas CT Michaels, Erik Poppleton, Alexander Ruf, Annemiek D Slootbeek, Iris BA Smokers, Héctor Soria-Carrera, Alessandro Sorrenti, Michele Stasi, Alisdair Stevenson, Ad-

vait Thatte, **Mai Tran**, Merlijn HI van Haren, Hidde D Vuijk, Shelley FJ Wickham, Pablo Zambrano, Katarzyna P Adamala, Karen Alim, Ebbe Sloth Andersen, Claudia Bonfio, Dieter Braun, Erwin Frey, Ulrich Gerland, Wilhelm TS Huck, Frank Jülicher, Nadanai Laohakunakorn, L Mahadavan, Sijbren Otto, James Saenz, Petra Schwille, Kerstin Göpfrich, Christoph A Weber, Job Boekhoven; ‘A roadmap toward the synthesis of life’, *Chem* (2025), `https://doi.org/10.1016/j.chempr.2024.102399`

5. **Mai P Tran***, Taniya Chakraborty*, Erik Poppleton, Luca Monari, Maja Illig, Franziska Giessler, Kerstin Göpfrich; ‘Genetic encoding and expression of RNA origami cytoskeletons in synthetic cells’, *Nat. Nanotechnol.* (2025), `https://doi.org/10.1038/s41565-025-01879-3`

   Mai P Tran, cover image, ‘Synthetic cells get RNA origami hardware’, *Nat. Nanotechnol.* (2025), *20*(5) `https://www.nature.com/nnano/volumes/20/issues/5`

Submitted manuscript

1. William Verstraeten, **Mai P Tran**, Alena Taskina, Moritz Hamberger, Edward W Green, Michael Platten, Claudia Helbig, Kerstin Göpfrich; ‘Genetic encoding and mutagenesis of RNA droplet phenotypes’
   I contributed to the conceptual development of the project and the design of the experimental strategy. I conducted the analysis of droplet movement data and contributed extensively to the editing and refinement of the manuscript.
2. Cody Geary, **Mai P Tran**, Erik Poppleton, Kerstin Göpfrich; ‘Rational Design of an Edge-to-Edge RNA Connector for Programmable Self-Assembly’
   I contributed to the conceptual development of the project and the design of the experimental strategy. I contributed to the acquisition of the AFM images and to the writing of the manuscript.
3. Linus S. Frey, William Verstraeten, **Mai P Tran**, Cody Geary, Luca Monari, and Kerstin Göpfrich; ‘SecAntiGami: Secondary antibody-like RNA origami for aptamer validation’
   I co-supervised the conceptual development of the project and the design of the experimental strategy.

Patents

2025 *‘SecAntiGami: Secondary antibody-like RNA origami for aptamer validation’*, pending
Linus Frey, William Verstraeten, **Mai P. Tran**, Kerstin Göpfrich

Conferences

2022 MINDS – Molecular Mechanisms in Health and Disease Symposium, Niedernhausen, Germany
Poster: *'Engineering cells with DNA nanotechnology'*

2022 International Conference on Engineering Synthetic Cells and Organelles: SynCell2022, The Hague, Netherlands
Talk: *'Mimicking DNA segregation inside cell-sized confinement'*

2023 Engineering Life: Unifying concepts from system chemistry, biophysics and theoretical physics, Munich, Germany
Talk: *'A DNA segregation module for synthetic cells'*

2023 Swiss-UK Synthetic Biology Conference 2023, Lausanne, Switzerland
Poster, Studentship awardee: *'RNA origami-based hardware for synthetic cells'*

2023 Alliance Science Day – ScienceSplash, Heidelberg, Germany
Flash talk: *'RNA origami-based hardware for synthetic cells'*

2023 Hector Fellow Academy Symposium, Berlin, Germany
Poster: *'RNA origami-based hardware for synthetic cells'*

2023 Young Scientist Retreat of Flagship Initiative Engineering Molecular Systems (FI EMS), Trifels, Germany
Talk: *'Overriding the central dogma: Expression of RNA origami based hardware in synthetic cells'*

2023 Spotlight Project "Synthetic Immunology" Annual Meeting, Heidelberg, Germany
Poster: *'DNA origami for studying B cell activation'*

2024 FDN2024: 6th Functional DNA Nanotechnology Workshop, Munich, Germany
Poster prize and Talk: *'Expression of an RNA origami cytoskeleton in synthetic cells'*

2025 Bionanotech in Action webinar of The University of Edinburgh, UK
Talk: *'RNA origami-based hardware for synthetic cells'*

2025 Advances in bioinspiration, Paris, France
Invited talk: *'RNA origami-based hardware for synthetic cells'*

2025 Mechanobiology Conference III: From Fundamental Research to Applications, Quy Nhon, Vietnam
Talk and poster: *'Genetic encoding and expression of RNA origami cytoskeletons in synthetic cells'*

B

Permissions

This appendix contains the permission for the reuse and adaptation of individual figures that were not published under Creative Commons licenses.

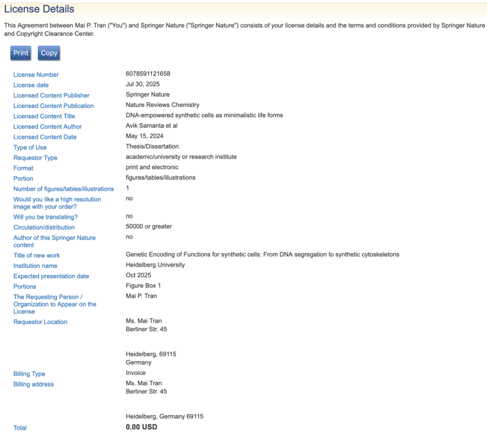

License Details

This Agreement between Mai P. Tran ("You") and Springer Nature ("Springer Nature") consists of your license details and the terms and conditions provided by Springer Nature and Copyright Clearance Center.

License Number	6078591121658
License date	Jul 30, 2025
Licensed Content Publisher	Springer Nature
Licensed Content Publication	Nature Reviews Chemistry
Licensed Content Title	DNA-empowered synthetic cells as minimalistic life forms
Licensed Content Author	Avik Samanta et al
Licensed Content Date	May 15, 2024
Type of Use	Thesis/Dissertation
Requestor Type	academic/university or research institute
Format	print and electronic
Portion	figures/tables/illustrations
Number of figures/tables/illustrations	1
Would you like a high resolution image with your order?	no
Will you be translating?	no
Circulation/distribution	50000 or greater
Author of this Springer Nature content	no
Title of new work	Genetic Encoding of Functions for synthetic cells: From DNA segregation to synthetic cytoskeletons
Institution name	Heidelberg University
Expected presentation date	Oct 2025
Portions	Figure Box 1
The Requesting Person / Organization to Appear on the License	Mai P. Tran
Requestor Location	Ms. Mai Tran Berliner Str. 45 Heidelberg, 69115 Germany
Billing Type	Invoice
Billing address	Ms. Mai Tran Berliner Str. 45 Heidelberg, Germany 69115
Total	**0.00 USD**

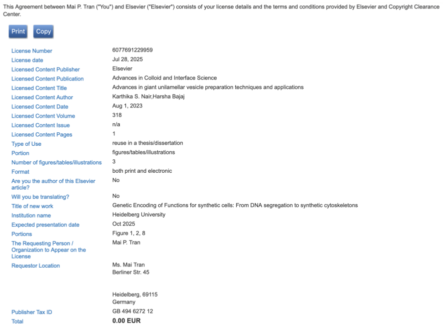

This Agreement between Mai P. Tran ("You") and Elsevier ("Elsevier") consists of your license details and the terms and conditions provided by Elsevier and Copyright Clearance Center.

License Number	6077691229959
License date	Jul 28, 2025
Licensed Content Publisher	Elsevier
Licensed Content Publication	Advances in Colloid and Interface Science
Licensed Content Title	Advances in giant unilamellar vesicle preparation techniques and applications
Licensed Content Author	Karthika S. Nair,Harsha Bajaj
Licensed Content Date	Aug 1, 2023
Licensed Content Volume	318
Licensed Content Issue	n/a
Licensed Content Pages	1
Type of Use	reuse in a thesis/dissertation
Portion	figures/tables/illustrations
Number of figures/tables/illustrations	3
Format	both print and electronic
Are you the author of this Elsevier article?	No
Will you be translating?	No
Title of new work	Genetic Encoding of Functions for synthetic cells: From DNA segregation to synthetic cytoskeletons
Institution name	Heidelberg University
Expected presentation date	Oct 2025
Portions	Figure 1, 2, 8
The Requesting Person / Organization to Appear on the License	Mai P. Tran
Requestor Location	Ms. Mai Tran Berliner Str. 45 Heidelberg, 69115 Germany
Publisher Tax ID	GB 494 6272 12
Total	**0.00 EUR**

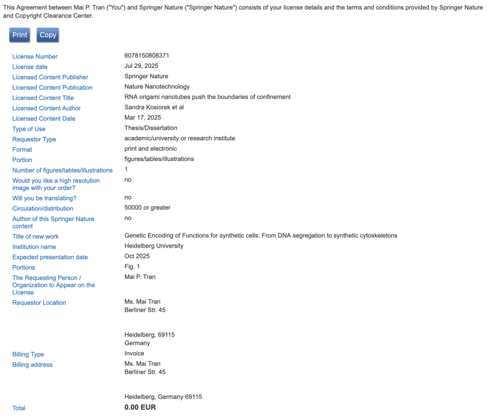

This Agreement between Mai P. Tran ("You") and Springer Nature ("Springer Nature") consists of your license details and the terms and conditions provided by Springer Nature and Copyright Clearance Center.

License Number	6078150808371
License date	Jul 29, 2025
Licensed Content Publisher	Springer Nature
Licensed Content Publication	Nature Nanotechnology
Licensed Content Title	RNA origami nanotubes push the boundaries of confinement
Licensed Content Author	Sandra Kosiorek et al
Licensed Content Date	Mar 17, 2025
Type of Use	Thesis/Dissertation
Requestor Type	academic/university or research institute
Format	print and electronic
Portion	figures/tables/illustrations
Number of figures/tables/illustrations	1
Would you like a high resolution image with your order?	no
Will you be translating?	no
Circulation/distribution	50000 or greater
Author of this Springer Nature content	no
Title of new work	Genetic Encoding of Functions for synthetic cells: From DNA segregation to synthetic cytoskeletons
Institution name	Heidelberg University
Expected presentation date	Oct 2025
Portions	Fig. 1
The Requesting Person / Organization to Appear on the License	Mai P. Tran
Requestor Location	Ms. Mai Tran Berliner Str. 45 Heidelberg, 69115 Germany
Billing Type	Invoice
Billing address	Ms. Mai Tran Berliner Str. 45 Heidelberg, Germany 69115
Total	**0.00 EUR**

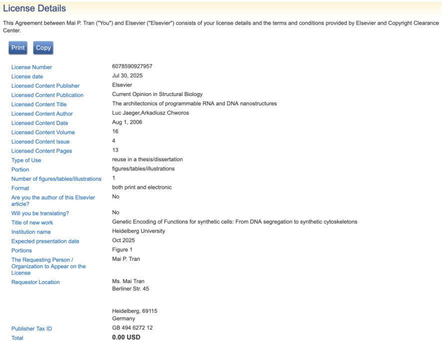

License Details

This Agreement between Mai P. Tran ("You") and Elsevier ("Elsevier") consists of your license details and the terms and conditions provided by Elsevier and Copyright Clearance Center.

License Number	6078590927957
License date	Jul 30, 2025
Licensed Content Publisher	Elsevier
Licensed Content Publication	Current Opinion in Structural Biology
Licensed Content Title	The architectonics of programmable RNA and DNA nanostructures
Licensed Content Author	Luc Jaeger,Arkadiusz Chworos
Licensed Content Date	Aug 1, 2006
Licensed Content Volume	16
Licensed Content Issue	4
Licensed Content Pages	13
Type of Use	reuse in a thesis/dissertation
Portion	figures/tables/illustrations
Number of figures/tables/illustrations	1
Format	both print and electronic
Are you the author of this Elsevier article?	No
Will you be translating?	No
Title of new work	Genetic Encoding of Functions for synthetic cells: From DNA segregation to synthetic cytoskeletons
Institution name	Heidelberg University
Expected presentation date	Oct 2025
Portions	Figure 1
The Requesting Person / Organization to Appear on the License	Mai P. Tran
Requestor Location	Ms. Mai Tran Berliner Str. 45 Heidelberg, 69115 Germany
Publisher Tax ID	GB 494 6272 12
Total	**0.00 USD**

Bibliography

1. Szostak, J. W., Bartel, D. P. & Luisi, P. L. Synthesizing life. *Nature* **409,** 387–390 (2001).
2. Bich, L. & Green, S. Is defining life pointless? Operational definitions at the frontiers of biology. *Synthese* **195,** 3919–3946 (2018).
3. Hanson, A. D. & Lorenzo, V. d. Synthetic Biology High time to deliver? *ACS synthetic biology* **12,** 1579–1582 (2023).
4. Harold, F. M. in *In Search of Cell History* (University of Chicago Press, 2014).
5. Mariscal, C. in *The Stanford Encyclopedia of Philosophy* (ed Zalta, E. N.) Winter 2021 (Metaphysics Research Lab, Stanford University, 2021).
6. Kriebisch, C. M. *et al.* A roadmap toward the synthesis of life. *Chem* **11** (2025).
7. Rothschild, L. J. *et al.* Building synthetic cells from the technology infrastructure to cellular entities. *ACS Synthetic Biology* **13,** 974–997 (2024).
8. Vibhute, M. A. & Mutschler, H. A Primer on Building Life-Like Systems. *ChemSystemsChem* **5,** e202200033 (2023).
9. Morowitz, H. J. Biological self-replicating systems. *Progress in theoretical biology* **1,** 35–58 (1967).
10. Dyson, F. J. A model for the origin of life. *Journal of Molecular Evolution* **18,** 344–350 (1982).
11. Luisi, P. L. *The emergence of life: from chemical origins to synthetic biology* (Cambridge University Press, 2016).
12. Benner, S. A. Defining life. *Astrobiology* **10,** 1021–1030 (2010).
13. Xiao, F., Shen, X., Tang, W. & Yang, D. Emerging Trends in DNA Nanotechnology-Enabled Cell Surface Engineering. *JACS Au* **5,** 550–570 (2025).
14. Schoenit, A., Cavalcanti-Adam, E. A. & Göpfrich, K. Functionalization of cellular membranes with DNA nanotechnology. *Trends in Biotechnology* **39,** 1208–1220 (2021).
15. Schwille, P. & Frohn, B. P. Hidden protein functions and what they may teach us. *Trends in Cell Biology* **32,** 102–109 (2022).
16. Posfai, G. *et al.* Emergent properties of reduced-genome Escherichia coli. *science* **312,** 1044–1046 (2006).
17. Moger-Reischer, R. Z. *et al.* Evolution of a minimal cell. *Nature* **620,** 122–127 (2023).
18. Voigt, C. A. Synthetic biology 2020–2030: six commercially-available products that are changing our world. *Nature Communications* **11,** 6379 (2020).

19. Chang, T. Hemoglobin corpuscles. *Report of a research project for Honours Physiology, Medical Library, McGill University,* 1–9 (1957).
20. Thornburg, Z. R. *et al.* Fundamental behaviors emerge from simulations of a living minimal cell. *Cell* **185,** 345–360 (2022).
21. Sato, W., Zajkowski, T., Moser, F. & Adamala, K. P. Synthetic cells in biomedical applications. *Wiley Interdisciplinary Reviews: Nanomedicine and Nanobiotechnology* **14,** e1761 (2022).
22. Liu, A. P. *et al.* The living interface between synthetic biology and biomaterial design. *Nature materials* **21,** 390–397 (2022).
23. Göpfrich, K., Platten, M., Frischknecht, F. & Fackler, O. T. Bottom-up synthetic immunology. *Nature nanotechnology* **19,** 1587–1596 (2024).
24. Luisi, P. L. Toward the engineering of minimal living cells. *The Anatomical Record: An Official Publication of the American Association of Anatomists* **268,** 208–214 (2002).
25. Gibson, D. G. *et al.* Creation of a bacterial cell controlled by a chemically synthesized genome. *science* **329,** 52–56 (2010).
26. Hutchison III, C. A. *et al.* Design and synthesis of a minimal bacterial genome. *Science* **351,** aad6253 (2016).
27. McFarland, G. The benefits of bottom-up design. *ACM SIGSOFT Software Engineering Notes* **11,** 43–51 (1986).
28. Gayon, J. Defining life: synthesis and conclusions. *Origins of Life and Evolution of Biospheres* **40,** 231–244 (2010).
29. Buddingh', B. C. & van Hest, J. C. Artificial cells: synthetic compartments with life-like functionality and adaptivity. *Accounts of chemical research* **50,** 769–777 (2017).
30. Yewdall, N. A., Mason, A. F. & Van Hest, J. C. The hallmarks of living systems: towards creating artificial cells. *Interface Focus* **8,** 20180023 (2018).
31. Nicholson, D. J. Is the cell really a machine? *Journal of theoretical biology* **477,** 108–126 (2019).
32. Wikipedia contributors. *Blind men and an elephant — Wikipedia, The Free Encyclopedia* [Online; accessed 29-July-2025]. 2025. `https://en.wikipedia.org/w/index.php?title=Blind_men_and_an_elephant&oldid=1302303899`.
33. Abil, Z. & Danelon, C. Roadmap to building a cell: an evolutionary approach. *Frontiers in Bioengineering and Biotechnology* **8,** 927 (2020).
34. Frohn, B. P., Kohyama, S. & Schwille, P. Protein design and optimization for synthetic cells. *Nature Reviews Bioengineering,* 1–15 (2025).
35. Stock, M. & Gorochowski, T. E. Open-endedness in synthetic biology: A route to continual innovation for biological design. *Science Advances* **10,** eadi3621 (2024).
36. Castle, S. D., Stock, M. & Gorochowski, T. E. Engineering is evolution: a perspective on design processes to engineer biology. *Nature Communications* **15,** 3640 (2024).
37. Beaudry, A. A. & Joyce, G. F. Directed evolution of an RNA enzyme. *Science* **257,** 635–641 (1992).

38. Stemmer, W. P. Rapid evolution of a protein in vitro by DNA shuffling. *Nature* **370,** 389–391 (1994).
39. Smith, G. P. Filamentous fusion phage: novel expression vectors that display cloned antigens on the virion surface. *Science* **228,** 1315–1317 (1985).
40. Esvelt, K. M., Carlson, J. C. & Liu, D. R. A system for the continuous directed evolution of biomolecules. *Nature* **472,** 499–503 (2011).
41. Chen, K. & Arnold, F. H. Tuning the activity of an enzyme for unusual environments: sequential random mutagenesis of subtilisin E for catalysis in dimethylformamide. *Proceedings of the National Academy of Sciences* **90,** 5618–5622 (1993).
42. Yang, J. *et al.* Active learning-assisted directed evolution. *Nature Communications* **16,** 714 (2025).
43. McLure, R. J., Radford, S. E. & Brockwell, D. J. High-throughput directed evolution: a golden era for protein science. *Trends in Chemistry* **4,** 378–391 (2022).
44. Arnold, F. H. *et al.* Innovation by evolution: bringing new chemistry to life (Nobel Lecture). *Angew. Chem. Int. Ed* **58,** 14420–14426 (2019).
45. Vidal, L. S., Isalan, M., Heap, J. T. & Ledesma-Amaro, R. A primer to directed evolution: current methodologies and future directions. *RSC Chemical Biology* **4,** 271–291 (2023).
46. Darwin, C. *On the Origin of Species by Means of Natural Selection* or the Preservation of Favored Races in the Struggle for Life (Murray, London, 1859).
47. Li, J., Browning, S., Mahal, S. P., Oelschlegel, A. M. & Weissmann, C. Darwinian evolution of prions in cell culture. *Science* **327,** 869–872 (2010).
48. Eleveld, M. J. *et al.* Departure from randomness: Evolution of self-replicators that can self-sort through steric zipper formation. *Chem* **11** (2025).
49. Pinheiro, V. B. *et al.* Synthetic genetic polymers capable of heredity and evolution. *Science* **336,** 341–344 (2012).
50. Soria-Carrera, H., Kauling, L. & Boekhoven, J. Genotype-Phenotype Coupling in Fuel-Dependent Synthetic Cells with an Autocatalyst. *Available at SSRN 5191734*.
51. Duim, H. & Otto, S. Towards open-ended evolution in self-replicating molecular systems. *Beilstein journal of organic chemistry* **13,** 1189–1203 (2017).
52. Wikipedia contributors. *Nucleoside triphosphate — Wikipedia, The Free Encyclopedia* [Online; accessed 30-July-2025]. 2025. `https://en.wikipedia.org/w/index.php?title=Nucleoside_triphosphate&oldid=1300578955`.
53. Vogele, K. *et al.* Towards synthetic cells using peptide-based reaction compartments. *Nature Communications* **9,** 3862 (2018).
54. Xu, C., Martin, N., Li, M. & Mann, S. Living material assembly of bacteriogenic protocells. *Nature* **609,** 1029–1037 (2022).
55. Berhanu, S., Ueda, T. & Kuruma, Y. Artificial photosynthetic cell producing energy for protein synthesis. *Nature communications* **10,** 1325 (2019).
56. Lavickova, B., Laohakunakorn, N. & Maerkl, S. J. A partially self-regenerating synthetic cell. *Nature Communications* **11,** 6340 (2020).
57. Abil, Z. *et al.* Darwinian evolution of self-replicating DNA in a synthetic protocell. *Nature Communications* **15,** 9091 (2024).

58. Forster, A. C. & Church, G. M. Towards synthesis of a minimal cell. *Molecular systems biology* **2,** 45 (2006).
59. De Capitani, J. & Mutschler, H. The Long Road to a Synthetic Self-Replicating Central Dogma. *Biochemistry* **62,** 1221–1232 (2023).
60. Garenne, D. *et al.* Cell-free gene expression. *Nature Reviews Methods Primers* **1,** 49 (2021).
61. Robertson, M. P. & Joyce, G. F. The origins of the RNA world. *Cold Spring Harbor perspectives in biology* **4,** a003608 (2012).
62. Flores, R., Navarro, B., Serra, P. & Di Serio, F. A scenario for the emergence of protoviroids in the RNA world and for their further evolution into viroids and viroid-like RNAs by modular recombinations and mutations. *Virus Evolution* **8,** veab107 (2022).
63. Seeman, N. C. Nucleic acid junctions and lattices. *Journal of theoretical biology* **99,** 237–247 (1982).
64. Rothemund, P. W. Folding DNA to create nanoscale shapes and patterns. *Nature* **440,** 297–302 (2006).
65. Luo, L. *et al.* DNA nanopores as artificial membrane channels for bioprotonics. *Nature Communications* **14,** 5364 (2023).
66. Jahnke, K. *et al.* DNA origami signaling units transduce chemical and mechanical signals in synthetic cells. *Advanced Functional Materials* **34,** 2301176 (2024).
67. Tran, M. P. *et al.* A DNA segregation module for synthetic cells. *Small* **19,** 2202711 (2023).
68. Jahnke, K., Huth, V., Mersdorf, U., Liu, N. & Göpfrich, K. Bottom-up assembly of synthetic cells with a DNA cytoskeleton. *ACS nano* **16,** 7233–7241 (2022).
69. Göpfrich, K., Platzman, I. & Spatz, J. P. Mastering Complexity: Towards Bottom-up Construction of Multifunctional Eukaryotic Synthetic Cells. *Trends in Biotechnology* **36,** 938–951. ISSN: 18793096 (2018).
70. Göpfrich, K. & Keyser, U. F. DNA nanotechnology for building sensors, nanopores and ion-channels. *Biological and Bio-inspired Nanomaterials: Properties and Assembly Mechanisms,* 331–370 (2019).
71. Seeman, N. C. & Sleiman, H. F. DNA nanotechnology. *Nature Reviews Materials* **3,** 1–23 (2017).
72. Geary, C. in *Visions of DNA Nanotechnology at 40 for the Next 40: A Tribute to Nadrian C. Seeman* 207–227 (Springer, 2023).
73. Jaeger, L. & Chworos, A. The architectonics of programmable RNA and DNA nanostructures. *Current opinion in structural biology* **16,** 531–543 (2006).
74. Lund, K. *et al.* Molecular robots guided by prescriptive landscapes. *Nature* **465,** 206–210 (2010).
75. Ketterer, P., Willner, E. M. & Dietz, H. Nanoscale rotary apparatus formed from tight-fitting 3D DNA components. *Science advances* **2,** e1501209 (2016).
76. Kopperger, E. *et al.* A self-assembled nanoscale robotic arm controlled by electric fields. *Science* **359,** 296–301 (2018).
77. Douglas, S. M., Bachelet, I. & Church, G. M. A logic-gated nanorobot for targeted transport of molecular payloads. *Science* **335,** 831–834 (2012).

78. Simmel, F. C. in *Visions of DNA Nanotechnology at 40 for the Next 40: A Tribute to Nadrian C. Seeman* 17–29 (Springer, 2023).
79. Vallina, N. S., McRae, E. K., Geary, C. & Andersen, E. S. An RNA origami robot that traps and releases a fluorescent aptamer. *Science Advances* **10,** eadk1250 (2024).
80. Afonin, K. A., Cieply, D. J. & Leontis, N. B. Specific RNA self-assembly with minimal paranemic motifs. en. *J. Am. Chem. Soc.* **130,** 93–102 (Jan. 2008).
81. Qi, X. *et al.* Programming molecular topologies from single-stranded nucleic acids. *Nature communications* **9,** 4579 (2018).
82. Sampedro Vallina, N., McRae, E. K., Geary, C. & Andersen, E. S. An RNA paranemic crossover triangle as a 3D module for cotranscriptional nanoassembly. *Small* **19,** 2204651 (2023).
83. Geary, C., Rothemund, P. W. & Andersen, E. S. A single-stranded architecture for cotranscriptional folding of RNA nanostructures. *Science* **345,** 799–804 (2014).
84. Geary, C., Chworos, A., Verzemnieks, E., Voss, N. R. & Jaeger, L. Composing RNA nanostructures from a syntax of RNA structural modules. *Nano letters* **17,** 7095–7101 (2017).
85. Zhou, Y., Dong, J. & Wang, Q. Fabricating higher-order functional DNA origami structures to reveal biological processes at multiple scales. *NPG Asia Materials* **15,** 25 (2023).
86. Tikhomirov, G., Petersen, P. & Qian, L. Fractal assembly of micrometre-scale DNA origami arrays with arbitrary patterns. *Nature* **552,** 67–71 (2017).
87. Yan, H. & Seeman, N. C. Edge-sharing motifs in structural DNA nanotechnology. *Journal of Supramolecular Chemistry* **1,** 229–237 (2001).
88. Zhang, X., Yan, H., Shen, Z. & Seeman, N. C. Paranemic cohesion of topologically-closed DNA molecules. *Journal of the American Chemical Society* **124,** 12940–12941 (2002).
89. Geary, C., Grossi, G., McRae, E. K., Rothemund, P. W. & Andersen, E. S. RNA origami design tools enable cotranscriptional folding of kilobase-sized nanoscaffolds. *Nature chemistry* **13,** 549–558 (2021).
90. Jaeger, L., Westhof, E. & Leontis, N. B. TectoRNA: modular assembly units for the construction of RNA nano-objects. *Nucleic acids research* **29,** 455–463 (2001).
91. Woo, S. & Rothemund, P. W. Programmable molecular recognition based on the geometry of DNA nanostructures. *Nature chemistry* **3,** 620–627 (2011).
92. Tikhomirov, G., Petersen, P. & Qian, L. Programmable disorder in random DNA tilings. *Nature nanotechnology* **12,** 251–259 (2017).
93. Dreher, Y. *et al.* Genotype-phenotype mapping with polyominos made from DNA origami tiles. *Biophysical Journal* **121,** 4840–4848 (2022).
94. Rajendran, A., Endo, M., Katsuda, Y., Hidaka, K. & Sugiyama, H. Programmed two-dimensional self-assembly of multiple DNA origami jigsaw pieces. *ACS nano* **5,** 665–671 (2011).
95. Gerling, T., Wagenbauer, K. F., Neuner, A. M. & Dietz, H. Dynamic DNA devices and assemblies formed by shape-complementary, non–base pairing 3D components. *Science* **347,** 1446–1452 (2015).

96. Arulkumaran, N., Singer, M., Howorka, S. & Burns, J. R. Creating complex protocells and prototissues using simple DNA building blocks. *Nature Communications* **14,** 1314 (2023).
97. Tran, M. P. *et al.* Genetic encoding and expression of RNA origami cytoskeletons in synthetic cells. *Nature Nanotechnology,* 1–8 (2025).
98. Narayanan, R. P. *et al.* High-Affinity Host–Guest Recognition for Efficient Assembly and Enzymatic Responsiveness of DNA Nanostructures. *Small* **20,** 2307585 (2024).
99. Chidchob, P., Edwardson, T. G., Serpell, C. J. & Sleiman, H. F. Synergy of two assembly languages in DNA nanostructures: self-assembly of sequence-defined polymers on DNA cages. *Journal of the American Chemical Society* **138,** 4416–4425 (2016).
100. Daly, M. L. *et al.* Designer peptide–DNA cytoskeletons regulate the function of synthetic cells. *Nature Chemistry* **16,** 1229–1239 (2024).
101. Jiang, T. *et al.* Structurally ordered nanowire formation from co-assembly of DNA origami and collagen-mimetic peptides. *Journal of the American Chemical Society* **139,** 14025–14028 (2017).
102. Younas, T., Liu, C., Struwe, W. B., Kukura, P. & He, L. Engineer RNA-Protein Nanowires as Light-Responsive Biomaterials. *Small* **19,** 2206513 (2023).
103. Praetorius, F. *et al.* Biotechnological mass production of DNA origami. *Nature* **552,** 84–87 (2017).
104. Li, M. *et al.* In vivo production of RNA nanostructures via programmed folding of single-stranded RNAs. *Nature communications* **9,** 2196 (2018).
105. Pothoulakis, G., Nguyen, M. T. & Andersen, E. S. Utilizing RNA origami scaffolds in Saccharomyces cerevisiae for dCas9-mediated transcriptional control. *Nucleic Acids Research* **50,** 7176–7187 (2022).
106. Ng, B. *et al.* Expression of nano-engineered RNA organelles in bacteria. *bioRxiv,* 2025–07 (2025).
107. Um, S. H. *et al.* Enzyme-catalysed assembly of DNA hydrogel. *Nature materials* **5,** 797–801 (2006).
108. Dill, K. A. & MacCallum, J. L. The protein-folding problem, 50 years on. *science* **338,** 1042–1046 (2012).
109. Winfree, E., Liu, F., Wenzler, L. A. & Seeman, N. C. Design and self-assembly of two-dimensional DNA crystals. *Nature* **394,** 539–544 (1998).
110. Rothemund, P. W. *et al.* Design and characterization of programmable DNA nanotubes. *Journal of the American Chemical Society* **126,** 16344–16352 (2004).
111. Wagenbauer, K. F., Sigl, C. & Dietz, H. Gigadalton-scale shape-programmable DNA assemblies. *Nature* **552,** 78–83 (2017).
112. Chworos, A. *et al.* Building programmable jigsaw puzzles with RNA. *Science* **306,** 2068–2072 (2004).
113. Rothemund, P. W. K., Papadakis, N. & Winfree, E. Algorithmic self-assembly of DNA Sierpinski triangles. *PLoS biology* **2,** e424 (2004).
114. Xu, J. in *Biological Computing* 255–284 (Springer, 2025).

115. Wintersinger, C. M. *et al.* Multi-micron crisscross structures grown from DNA-origami slats. *Nature nanotechnology* **18,** 281–289 (2023).
116. Al-Hashimi, H. M. & Walter, N. G. RNA dynamics: it is about time. *Current opinion in structural biology* **18,** 321–329 (2008).
117. Poppleton, E. *et al.* RNA origami: design, simulation and application. *RNA biology* **20,** 510–524 (2023).
118. Tran, M. P. & Göpfrich, K. in *The Art of Molecular Programming* (eds Scalise, D. & Sarraf, N.) ().
119. Samanta, A., Baranda Pellejero, L., Masukawa, M. & Walther, A. DNA-empowered synthetic cells as minimalistic life forms. *Nature Reviews Chemistry* **8,** 454–470 (2024).
120. Sato, Y. Artificial Molecular Systems for Complex Functions Based on DNA Nanotechnology and Cell-Sized Lipid Vesicles. *ChemSystemsChem* **6,** e202400021 (2024).
121. Felgner, P. L. *et al.* Lipofection: a highly efficient, lipid-mediated DNA-transfection procedure. *Proceedings of the National Academy of Sciences* **84,** 7413–7417 (1987).
122. Hoekstra Sandrine Audouy, D. Cationic lipid-mediated transfection in vitro and in vivo. *Molecular membrane biology* **18,** 129–143 (2001).
123. Shen, Q., Grome, M. W., Yang, Y. & Lin, C. Engineering lipid membranes with programmable DNA nanostructures. *Advanced biosystems* **4,** 1900215 (2020).
124. Rubio-Sánchez, R., Fabrini, G., Cicuta, P. & Di Michele, L. Amphiphilic DNA nanostructures for bottom-up synthetic biology. *Chemical Communications* **57,** 12725–12740 (2021).
125. Hadorn, M. & Eggenberger Hotz, P. DNA-mediated self-assembly of artificial vesicles. *PLoS One* **5,** e9886 (2010).
126. Fu, Y.-H. *et al.* Constructing artificial gap junctions to mediate intercellular signal and mass transport. *Nature Chemistry,* 1–9 (2024).
127. Huang, X., Skowicki, M., Dinu, I. A., Schoenenberger, C.-A. & Palivan, C. G. Stimuli-Responsive Prototissues via DNA-Mediated Self-Assembly of Polymer Giant Unilamellar Vesicles. *Advanced Functional Materials* **34,** 2408373 (2024).
128. Chakraborty, T. & Wegner, S. V. Cell to cell signaling through light in artificial cell communities: glowing predator lures prey. *Acs Nano* **15,** 9434–9444 (2021).
129. Luo, R., Göpfrich, K., Platzman, I. & Spatz, J. P. DNA-based assembly of multi-compartment polymersome networks. *Advanced Functional Materials* **30,** 2003480 (2020).
130. Chan, Y.-H. M., van Lengerich, B. & Boxer, S. G. Effects of linker sequences on vesicle fusion mediated by lipid-anchored DNA oligonucleotides. *Proceedings of the National Academy of Sciences* **106,** 979–984 (2009).
131. Marsden, H. R., Korobko, A. V., Zheng, T., Voskuhl, J. & Kros, A. Controlled liposome fusion mediated by SNARE protein mimics. *Biomaterials science* **1,** 1046–1054 (2013).

132. Kanwa, N., Gavrilovic, S., Brüggenthies, G. A., Qutbuddin, Y. & Schwille, P. Inducing Lipid Domains in Membranes by Self-Assembly of DNA Origami. *Advanced Materials Interfaces* **10,** 2202500 (2023).
133. Pinner, M. T. & Dietz, H. Programmable DNA shell scaffolds for directional membrane budding. *bioRxiv,* 2024–01 (2024).
134. Zhan, P. *et al.* 3D DNA origami pincers that multitask on giant unilamellar vesicles. *Science Advances* **10,** eadn8903 (2024).
135. Grome, M. W., Zhang, Z., Pincet, F. & Lin, C. Vesicle tubulation with self-assembling DNA nanosprings. *Angewandte Chemie International Edition* **57,** 5330–5334 (2018).
136. Franquelim, H. G., Dietz, H. & Schwille, P. Reversible membrane deformations by straight DNA origami filaments. *Soft Matter* **17,** 276–287 (2021).
137. Franquelim, H. G., Khmelinskaia, A., Sobczak, J.-P., Dietz, H. & Schwille, P. Membrane sculpting by curved DNA origami scaffolds. *Nature communications* **9,** 811 (2018).
138. De Franceschi, N. *et al.* Synthetic membrane shaper for controlled liposome deformation. *ACS nano* **17,** 966–978 (2022).
139. Czogalla, A. *et al.* Amphipathic DNA origami nanoparticles to scaffold and deform lipid membrane vesicles. *Angewandte Chemie International Edition* **54,** 6501–6505 (2015).
140. Journot, C. M., Ramakrishna, V., Wallace, M. I. & Turberfield, A. J. Modifying membrane morphology and interactions with DNA origami clathrin-mimic networks. *ACS nano* **13,** 9973–9979 (2019).
141. Fan, S. *et al.* Morphology remodelling and membrane channel formation in synthetic cells via reconfigurable DNA nanorafts. *Nature Materials,* 1–9 (2025).
142. Langecker, M. *et al.* Synthetic Lipid Membrane Channels Formed by Designed DNA Nanostructures. *Science* **338,** 932–936. ISSN: 0036-8075. `http://www.sciencemag.org/cgi/doi/10.1126/science.1225624` (Nov. 2012).
143. Burns, J. R. *et al.* Lipid-bilayer-spanning DNA nanopores with a bifunctional porphyrin anchor. *Angewandte Chemie (International ed. in English)* **52,** 12069 (2013).
144. Krishnan, S. *et al.* Molecular transport through large-diameter DNA nanopores. *Nature communications* **7,** 12787 (2016).
145. Göpfrich, K. *et al.* Ion channels made from a single membrane-spanning DNA duplex. *Nano letters* **16,** 4665–4669 (2016).
146. Fragasso, A. *et al.* Reconstitution of ultrawide DNA origami pores in liposomes for transmembrane transport of macromolecules. *ACS nano* **15,** 12768–12779 (2021).
147. Li, H. *et al.* Construction of RNA nanotubes. *Nano research* **12,** 1952–1958 (2019).
148. Dey, S. *et al.* A reversibly gated protein-transporting membrane channel made of DNA. *Nature communications* **13,** 2271 (2022).
149. Iwabuchi, S., Kawamata, I., Murata, S. & Nomura, S.-i. M. A large, square-shaped, DNA origami nanopore with sealing function on a giant vesicle membrane. *Chemical Communications* **57,** 2990–2993 (2021).

150. Peng, R. *et al.* DNA-based artificial molecular signaling system that mimics basic elements of reception and response. *Nature Communications* **11,** 978 (2020).
151. Lanphere, C., Arnott, P. M., Jones, S. F., Korlova, K. & Howorka, S. A biomimetic DNA-based membrane gate for protein-controlled transport of cytotoxic drugs. *Angewandte Chemie International Edition* **60,** 1903–1908 (2021).
152. Chen, H. *et al.* Oriented triplex DNA as a synthetic receptor for transmembrane signal transduction. *Nature Communications* **15,** 9789 (2024).
153. Ohmann, A. *et al.* A synthetic enzyme built from DNA flips 107lipids per second in biological membranes. *Nature Communications* **9,** 2426. ISSN: 20411723. `http://dx.doi.org/10.1038/s41467-018-04821-5` (2018).
154. Chen, H. *et al.* Controlled dimerization of artificial membrane receptors for transmembrane signal transduction. *Chemical Science* **12,** 8224–8230 (2021).
155. Liu, G. *et al.* DNA-based artificial signaling system mimicking the dimerization of receptors for signal transduction and amplification. *Analytical Chemistry* **93,** 13807–13814 (2021).
156. Chen, H. *et al.* DNA-Based Artificial Receptors as Transmembrane Signal Transduction Systems for Protocellular Communication. *Angewandte Chemie* **135,** e202301559 (2023).
157. De Franceschi, N., Hoogenberg, B., Katan, A. & Dekker, C. Engineering ssRNA tile filaments for (dis) assembly and membrane binding. *Nanoscale* (2024).
158. Stewart, J. M., Geary, C. & Franco, E. Design and characterization of RNA nanotubes. *ACS nano* **13,** 5214–5221 (2019).
159. Illig, M. *et al.* Triggered contraction of self-assembled micron-scale DNA nanotube rings. *Nature Communications* **15,** 2307 (2024).
160. Agarwal, S., Klocke, M. A., Pungchai, P. E. & Franco, E. Dynamic self-assembly of compartmentalized DNA nanotubes. *Nature communications* **12,** 3557 (2021).
161. Zhan, P., Jahnke, K., Liu, N. & Göpfrich, K. Functional DNA-based cytoskeletons for synthetic cells. *Nature Chemistry* **14,** 958–963 (2022).
162. Agarwal, S. & Franco, E. Enzyme-driven assembly and disassembly of hybrid DNA–RNA nanotubes. *Journal of the American Chemical Society* **141,** 7831–7841 (2019).
163. Green, L. N., Amodio, A., Subramanian, H. K., Ricci, F. & Franco, E. pH-driven reversible self-assembly of micron-scale DNA scaffolds. *Nano letters* **17,** 7283–7288 (2017).
164. Del Grosso, E., Prins, L. J. & Ricci, F. Transient DNA-based nanostructures controlled by redox inputs. *Angewandte Chemie International Edition* **59,** 13238–13245 (2020).
165. Dizani, M., Agarwal, S., Osmanovic, D. & Franco, E. Light-modulated self-assembly of synthetic nanotubes. *Nano Letters* **25,** 3122–3129 (2025).
166. Leathers, A. *et al.* Reaction–diffusion patterning of DNA-based artificial cells. *Journal of the American Chemical Society* **144,** 17468–17476 (2022).

167. Samanta, A., Hörner, M., Liu, W., Weber, W. & Walther, A. Signal-processing and adaptive prototissue formation in metabolic DNA protocells. *Nature Communications* **13,** 3968 (2022).
168. Jahnke, K. & Göpfrich, K. Engineering DNA-based cytoskeletons for synthetic cells. *Interface Focus* **13,** 20230028 (2023).
169. Zeng, Y. *et al.* Biomimetic and Biological Applications of DNA Coacervates. *Chinese Journal of Chemistry* **43,** 1442–1462 (2025).
170. Udono, H., Gong, J., Sato, Y. & Takinoue, M. DNA droplets: intelligent, dynamic fluid. *Advanced Biology* **7,** 2200180 (2023).
171. Majumder, S., Coupe, S., Fakhri, N. & Jain, A. Sequence-encoded intermolecular base pairing modulates fluidity in DNA and RNA condensates. *Nature Communications* **16,** 1–12 (2025).
172. Sato, Y. & Takinoue, M. Sequence-dependent fusion dynamics and physical properties of DNA droplets. *Nanoscale Advances* **5,** 1919–1925 (2023).
173. Sato, Y., Sakamoto, T. & Takinoue, M. Sequence-based engineering of dynamic functions of micrometer-sized DNA droplets. *Science advances* **6,** eaba3471 (2020).
174. Merindol, R., Loescher, S., Samanta, A. & Walther, A. Pathway-controlled formation of mesostructured all-DNA colloids and superstructures. *Nature nanotechnology* **13,** 730–738 (2018).
175. Zhao, Q.-H., Cao, F.-H., Luo, Z.-H., Huck, W. T. & Deng, N.-N. Photoswitchable Molecular Communication between Programmable DNA-Based Artificial Membraneless Organelles. *Angewandte Chemie* **134,** e202117500 (2022).
176. Sato, Y. & Takinoue, M. Capsule-like DNA hydrogels with patterns formed by lateral phase separation of DNA nanostructures. *JACS Au* **2,** 159–168 (2021).
177. Yoneyama, R. *et al.* Controlled Formation of DNA Condensates as Model Nuclei in Monodisperse Giant Vesicles. *JACS Au* (2025).
178. Fabrini, G. *et al.* Co-transcriptional production of programmable RNA condensates and synthetic organelles. *Nature Nanotechnology* **19,** 1665–1673 (2024).
179. Stewart, J. M. *et al.* Modular RNA motifs for orthogonal phase separated compartments. *Nature Communications* **15,** 6244 (2024).
180. Verstraeten, W. *et al.* Genetic encoding and mutagenesis of RNA droplet phenotypes (2025).
181. Groaz, A. *et al.* Engineering spatiotemporal organization and dynamics in synthetic cells. *Wiley Interdisciplinary Reviews: Nanomedicine and Nanobiotechnology* **13,** e1685 (2021).
182. Maffeis, V., Heuberger, L., Nikoletić, A., Schoenenberger, C.-A. & Palivan, C. G. Synthetic cells revisited: Artificial cell construction using polymeric building blocks. *Advanced Science* **11,** 2305837 (2024).
183. Smokers, I. B., Visser, B. S., Slootbeek, A. D., Huck, W. T. & Spruijt, E. How droplets can accelerate reactions coacervate protocells as catalytic microcompartments. *Accounts of chemical research* **57,** 1885–1895 (2024).
184. Mashaghi, S., Abbaspourrad, A., Weitz, D. A. & van Oijen, A. M. Droplet microfluidics: A tool for biology, chemistry and nanotechnology. *TrAC Trends in Analytical Chemistry* **82,** 118–125 (2016).

185. Van de Cauter, L., Van Buren, L., Koenderink, G. H. & Ganzinger, K. A. Exploring giant unilamellar vesicle production for artificial cells—current challenges and future directions. *Small Methods* **7,** 2300416 (2023).
186. Göpfrich, K. *et al.* One-Pot Assembly of Complex Giant Unilamellar Vesicle-Based Synthetic Cells. *ACS Synthetic Biology* **8,** 937–947 (2019).
187. Nair, K. S. & Bajaj, H. Advances in giant unilamellar vesicle preparation techniques and applications. *Advances in colloid and interface science* **318,** 102935 (2023).
188. Olivi, L. *et al.* Towards a synthetic cell cycle. *Nature communications* **12,** 1–11 (2021).
189. Schwille, P. Division in synthetic cells. *Emerging Topics in Life Sciences* **3,** 551–558 (2019).
190. Caspi, Y. & Dekker, C. Divided we stand: splitting synthetic cells for their proliferation. *Systems and synthetic biology* **8,** 249–269 (2014).
191. Chang, M.-Y., Ariyama, H., Huck, W. T. & Deng, N.-N. Division in synthetic cells. *Chemical Society Reviews* **52,** 3307–3325 (2023).
192. Dreher, Y., Jahnke, K., Schröter, M. & Göpfrich, K. Light-Triggered Cargo Loading and Division of DNA-Containing Giant Unilamellar Lipid Vesicles. *Nano Letters* **21,** 5952–5957 (2021).
193. Castro, J. M., Sugiyama, H. & Toyota, T. Budding and division of giant vesicles linked to phospholipid production. *Scientific reports* **9,** 1–9 (2019).
194. Dreher, Y., Jahnke, K., Bobkova, E., Spatz, J. P. & Göpfrich, K. Division and regrowth of phase-separated giant unilamellar vesicles. *Angewandte Chemie* **133,** 10756–10764 (2021).
195. Andes-Koback, M. & Keating, C. D. Complete budding and asymmetric division of primitive model cells to produce daughter vesicles with different interior and membrane compositions. *Journal of the American Chemical Society* **133,** 9545–9555 (2011).
196. Osawa, M. & Erickson, H. P. Liposome division by a simple bacterial division machinery. *Proceedings of the National Academy of Sciences* **110,** 11000–11004 (2013).
197. Steinkühler, J. *et al.* Controlled division of cell-sized vesicles by low densities of membrane-bound proteins. *Nature Communications* **11,** 905. ISSN: 20411723 (2020).
198. Kurihara, K. *et al.* Self-reproduction of supramolecular giant vesicles combined with the amplification of encapsulated DNA. *Nature chemistry* **3,** 775 (2011).
199. Zhu, T. F. & Szostak, J. W. Coupled growth and division of model protocell membranes. *Journal of the American Chemical Society* **131,** 5705–5713 (2009).
200. Szathmáry, E. & Demeter, L. Group selection of early replicators and the origin of life. *Journal of theoretical biology* **128,** 463–486 (1987).
201. Hürtgen, D., Murray, S. M., Mascarenhas, J. & Sourjik, V. DNA segregation in natural and synthetic minimal systems. *Advanced Biosystems* **3,** 1800316 (2019).

202. Jun, S. & Mulder, B. Entropy-driven spatial organization of highly confined polymers: lessons for the bacterial chromosome. *Proceedings of the National Academy of Sciences* **103,** 12388–12393 (2006).

203. Jun, S. & Wright, A. Entropy as the driver of chromosome segregation. *Nature Reviews Microbiology* **8,** 600–607 (2010).

204. Shih, W. M., Quispe, J. D. & Joyce, G. F. A 1.7-kilobase single-stranded DNA that folds into a nanoscale octahedron. *Nature* **427,** 618–621 (2004).

205. Akter, N., Alladin-Mustan, B. S., Liu, Y., An, J. & Gibbs, J. M. Self-Replicating DNA-Based Nanoassemblies. *Journal of the American Chemical Society* **146,** 18205–18209 (2024).

206. Lichtman, J. W. & Conchello, J.-A. Fluorescence microscopy. *Nature methods* **2,** 910–919 (2005).

207. Elliott, A. D. Confocal microscopy: principles and modern practices. *Current protocols in cytometry* **92,** e68 (2020).

208. Hu, J. & Zhang, C.-y. Simple and accurate quantification of quantum yield at the single-molecule/particle level. *Analytical Chemistry* **85,** 2000–2004 (2013).

209. Bouhedda, F., Autour, A. & Ryckelynck, M. Light-up RNA aptamers and their cognate fluorogens: from their development to their applications. *International journal of molecular sciences* **19,** 44 (2017).

210. Lei, X. *et al.* Illuminating RNA through fluorescent light-up RNA aptamers. *Biosensors and Bioelectronics* **271,** 116969 (2025).

211. Wikipedia contributors. *Franck–Condon principle — Wikipedia, The Free Encyclopedia* [Online; accessed 29-July-2025]. 2025. `https://en.wikipedia.org/w/index.php?title=Franck%E2%80%93Condon_principle&oldid=1291792483`.

212. Wikipedia contributors. *Stokes shift — Wikipedia, The Free Encyclopedia* [Online; accessed 29-July-2025]. 2025. `https://en.wikipedia.org/w/index.php?title=Stokes_shift&oldid=1272491996`.

213. Wikipedia contributors. *Jablonski diagram — Wikipedia, The Free Encyclopedia* [Online; accessed 29-July-2025]. 2025. `https://en.wikipedia.org/w/index.php?title=Jablonski_diagram&oldid=1292962118`.

214. Park, J. S. & Kihm, K. D. Use of confocal laser scanning microscopy (CLSM) for depthwise resolved microscale-particle image velocimetry (μ-PIV). *Optics and Lasers in Engineering* **44,** 208–223 (2006).

215. Kim, J. Y. & Weon, B. M. Confocal microscopy of colloidal suspensions. *Applied Microscopy* **44,** 30–33 (2014).

216. Chen, X. *et al.* Principles and Applications of Liquid-Environment Atomic Force Microscopy. *Advanced Materials Interfaces* **9,** 2201864. eprint: `https://advanced.onlinelibrary.wiley.com/doi/pdf/10.1002/admi.202201864`. `https://advanced.onlinelibrary.wiley.com/doi/abs/10.1002/admi.202201864` (2022).

217. Dos Santos Natividade, R., Danzer, B., Somoza, V. & Koehler, M. Atomic force microscopy at the forefront: unveiling foodborne viruses with biophysical tools. en. *Npj Viruses* **3,** 25 (Apr. 2025).

218. Wikipedia contributors. *Atomic force microscopy — Wikipedia, The Free Encyclopedia* [Online; accessed 29-July-2025]. 2025. `https://en.wikipedia.org/w/index.php?title=Atomic_force_microscopy&oldid=1291707733`.
219. Maghsoudy-Louyeh, S., Kropf, M. & Tittmann, B. Review of progress in atomic force microscopy. *The Open Neuroimaging Journal* **12** (2018).
220. Liebig, A., Hapala, P., Weymouth, A. J. & Giessibl, F. J. Quantifying the evolution of atomic interaction of a complex surface with a functionalized atomic force microscopy tip. *Scientific reports* **10,** 14104 (2020).
221. Tang, Y. *et al.* DNA origami tessellations. *Journal of the American Chemical Society* **145,** 13858–13868 (2023).
222. Marko, J. F. & Siggia, E. D. Stretching dna. *Macromolecules* **28,** 8759–8770 (1995).
223. Abels, J., Moreno-Herrero, F., Van der Heijden, T., Dekker, C. & Dekker, N. H. Single-molecule measurements of the persistence length of double-stranded RNA. *Biophysical journal* **88,** 2737–2744 (2005).
224. Mücke, N. *et al.* Assessing the flexibility of intermediate filaments by atomic force microscopy. *Journal of molecular biology* **335,** 1241–1250 (2004).
225. Gittes, F., Mickey, B., Nettleton, J. & Howard, J. Flexural rigidity of microtubules and actin filaments measured from thermal fluctuations in shape. *The Journal of cell biology* **120,** 923–934 (1993).
226. Murugesapillai, D. *et al.* Accurate nanoscale flexibility measurement of DNA and DNA–protein complexes by atomic force microscopy in liquid. *Nanoscale* **9,** 11327–11337 (2017).
227. Geary, C. W. & Andersen, E. S. *Design principles for single-stranded RNA origami structures* in *DNA Computing and Molecular Programming: 20th International Conference* **20** (2014), 1–19.
228. Pettersen, E. F. *et al.* UCSF ChimeraX: Structure visualization for researchers, educators, and developers. *Protein science* **30,** 70–82 (2021).
229. McRae, E. K. *et al.* Structure, folding and flexibility of co-transcriptional RNA origami. *Nature Nanotechnology,* 1–10 (2023).
230. Gruber, A. R., Lorenz, R., Bernhart, S. H., Neuböck, R. & Hofacker, I. L. The vienna RNA websuite. *Nucleic acids research* **36,** W70–W74 (2008).
231. Chakraborty, T., Bartelt, S. M., Steinkühler, J., Dimova, R. & Wegner, S. V. Light controlled cell-to-cell adhesion and chemical communication in minimal synthetic cells. *Chemical communications* **55,** 9448–9451 (2019).
232. Šulc, P., Romano, F., Ouldridge, T. E., Doye, J. P. & Louis, A. A. A nucleotide-level coarse-grained model of RNA. *The Journal of chemical physics* **140** (2014).
233. Snodin, B. E. *et al.* Introducing improved structural properties and salt dependence into a coarse-grained model of DNA. *The Journal of chemical physics* **142** (2015).
234. Ouldridge, T. E., Louis, A. A. & Doye, J. P. Structural, mechanical, and thermodynamic properties of a coarse-grained DNA model. *The Journal of chemical physics* **134** (2011).

235. Rovigatti, L., Šulc, P., Reguly, I. Z. & Romano, F. A comparison between parallelization approaches in molecular dynamics simulations on GPUs. *Journal of computational chemistry* **36,** 1–8 (2015).
236. Poppleton, E. *et al.* oxDNA: coarse-grained simulations of nucleic acids made simple. *Journal of Open Source Software* **8,** 4693 (2023).
237. Suma, A. *et al.* Tacoxdna: A user-friendly web server for simulations of complex DNA structures, from single strands to origami. *Journal of computational chemistry* **40,** 2586–2595 (2019).
238. Doye, J. P. *et al.* in *DNA and RNA Origami: Methods and Protocols* 93–112 (Springer, 2023).
239. Bohlin, J. *et al.* Design and simulation of DNA, RNA and hybrid protein–nucleic acid nanostructures with oxView. *Nature protocols* **17,** 1762–1788 (2022).
240. Poppleton, E. *et al.* Design, optimization and analysis of large DNA and RNA nanostructures through interactive visualization, editing and molecular simulation. *Nucleic acids research* **48,** e72–e72 (2020).
241. Snodin, B. E. *et al.* Direct simulation of the self-assembly of a small DNA origami. *ACS nano* **10,** 1724–1737 (2016).
242. Russo, J., Tartaglia, P. & Sciortino, F. Reversible gels of patchy particles: role of the valence. *The Journal of chemical physics* **131** (2009).
243. Rueden, C. T. *et al.* ImageJ2: ImageJ for the next generation of scientific image data. *BMC bioinformatics* **18,** 1–26 (2017).
244. Nečas, D. & Klapetek, P. Gwyddion: an open-source software for SPM data analysis. *Central European Journal of Physics* **10,** 181–188. ISSN: 1895-1082 (1 2012).
245. Schomburg, D. & Salzmann, M. in *Enzyme Handbook 3* 909–915 (Springer, 1991).
246. Saleh, O. A., Jeon, B.-j. & Liedl, T. Enzymatic degradation of liquid droplets of DNA is modulated near the phase boundary. *Proceedings of the National Academy of Sciences* **117,** 16160–16166 (2020).
247. Eisenberg, E. & Baram, A. Random closest packing in a 2D lattice model. *J. Phys. A: Math. Gen.* **33** (2000).
248. Rotman, Z. & Eisenberg, E. Direct Measurements of the Dynamical Correlation Length Indicate its Divergence at an Athermal Glass Transition. *Phys. Rev. Lett.* **105** (2010).
249. Chatterjee, R. *et al.* Motion of active tracer in a lattice gas with cross-shaped particles. *J. Chem. Phys.* **150** (2019).
250. Merrigan, C. *et al.* Arrested states in persistent active matter: Gelation without attraction. *Phys. Rev. Research.* **2** (2020).
251. Rotman, Z. & Eisenberg, E. Ideal glass transition in a simple two-dimensional lattice model. *Phys. Rev. E* **80** (2009).
252. Haller, B. *et al.* Charge-controlled microfluidic formation of lipid-based single- and multicompartment systems. *Lab on a Chip* **18,** 2665–2674. ISSN: 1473-0189. `http://pubs.rsc.org/en/content/articlepdf/2018/lc/c8lc00582f` (2018).

253. Zadeh, J. N. *et al.* NUPACK: Analysis and design of nucleic acid systems. *Journal of computational chemistry* **32,** 170–173 (2011).
254. Jeon, B.-j. *et al.* Salt-dependent properties of a coacervate-like, self-assembled DNA liquid. *Soft Matter* **14,** 7009–7015 (2018).
255. Bomboi, F. *et al.* Equilibrium gels of trivalent DNA-nanostars: Effect of the ionic strength on the dynamics. *The European Physical Journal E* **38,** 1–8 (2015).
256. Lee, T., Do, S., Lee, J. G., Kim, D.-N. & Shin, Y. The flexibility-based modulation of DNA nanostar phase separation. *Nanoscale* **13,** 17638–17647 (2021).
257. Jahnke, K., Grubmüller, H., Igaev, M. & Göpfrich, K. Choice of fluorophore affects dynamic DNA nanostructures. *Nucleic Acids Research* **49,** 4186–4195 (Mar. 2021).
258. Gomes, E. & Shorter, J. The molecular language of membraneless organelles. *Journal of Biological Chemistry* **294,** 7115–7127 (2019).
259. Plaskon, D. *et al.* Step-by-Step Regulation of Productive and Abortive Transcription Initiation by Pyrophosphorolysis. *Journal of molecular biology* **434,** 167621 (2022).
260. Lanter, F., Erne, D., Ammann, D. & Simon, W. Neutral carrier based ion-selective electrode for intracellular magnesium activity studies. *Analytical Chemistry* **52,** 2400–2402 (1980).
261. Autour, A., Westhof, E. & Ryckelynck, M. iSpinach: a fluorogenic RNA aptamer optimized for in vitro applications. *Nucleic acids research* **44,** 2491–2500 (2016).
262. Dolder, N., Müller, P. & von Ballmoos, C. Experimental platform for the functional investigation of membrane proteins in giant unilamellar vesicles. *Soft matter* **18,** 5877–5893 (2022).
263. Nasalean, L., Baudrey, S., Leontis, N. B. & Jaeger, L. Controlling RNA self-assembly to form filaments. *Nucleic acids research* **34,** 1381–1392 (2006).
264. Liu, D. *et al.* Branched kissing loops for the construction of diverse RNA homooligomeric nanostructures. *Nature Chemistry* **12,** 249–259 (2020).
265. O'Neill, P., Rothemund, P. W., Kumar, A. & Fygenson, D. K. Sturdier DNA nanotubes via ligation. *Nano letters* **6,** 1379–1383 (2006).
266. Emamyari, S., Mirzaei, M., Mohammadinejad, S., Fazli, D. & Fazli, H. Impact of flexibility on the aggregation of polymeric macromolecules. *The European Physical Journal E* **46,** 66 (2023).
267. Rivetti, C., Guthold, M. & Bustamante, C. Scanning force microscopy of DNA deposited onto mica: EquilibrationversusKinetic trapping studied by statistical polymer chain analysis. *Journal of molecular biology* **264,** 919–932 (1996).
268. Bezanilla, M., Gladfelter, A. S., Kovar, D. R. & Lee, W.-L. Cytoskeletal dynamics: a view from the membrane. *Journal of Cell Biology* **209,** 329–337 (2015).
269. Deamer, D. W. & Fleischaker, G. R. *(Foreword by Joyce Gerald) Origins of life: the central concepts* (Jones and Bartlett, Boston, 1994).
270. Saha, R., Verbanic, S. & Chen, I. A. Lipid vesicles chaperone an encapsulated RNA aptamer. *Nature communications* **9,** 2313 (2018).

271. Peter, B., Levrier, A. & Schwille, P. Spatiotemporal Propagation of a Minimal Catalytic RNA Network in GUV Protocells by Temperature Cycling and Phase Separation. *Angewandte Chemie International Edition* **62,** e202218507 (2023).
272. Nilsson, M., Antson, D.-O., Barbany, G. & Landegren, U. RNA-templated DNA ligation for transcript analysis. *Nucleic Acids Research* **29,** 578–581 (2001).
273. Horning, D. P. & Joyce, G. F. Amplification of RNA by an RNA polymerase ribozyme. *Proceedings of the National Academy of Sciences* **113,** 9786–9791 (2016).

“Enjoy your cooking and the food will behave; moreover it will pass your pleasure on to those who eat it.”

Fergus Henderson

To all the cooks who made this journey enjoyable — may the spirit and dedication they inspired resonate throughout this thesis, and may the readers feel the joy that went into its creation.

Acknowledgment

First of all, I would like to thank my PhD committee: Dr. Ebbe Sloth Andersen, Prof. Dr. Kerstin Göpfrich, Prof. Dr. Dirk Grimm, and Prof. Dr. Dominik Niopek for the time and insight they offered while reviewing this thesis and participating on my committee.

I would like to sincerely thank my PhD supervisor, Prof. Dr. Kerstin Göpfrich, for her extraordinary support, guidance, and belief in me over the past years. She has been more than a mentor, at times a friend, a role model, and even a fairy godmother who made it possible for me to pursue and live out a dream I once thought was beyond reach. Her enthusiasm and dedication gave me the motivation I needed to persevere through the most challenging times. She went above and beyond in her role. Her mentorship has profoundly shaped not only my growth as a researcher but also as a person. I am grateful to have the privilege of being her student.

This thesis would not be what it is without the support of Cody Geary and Erik Poppleton. I am profoundly grateful for the scientific and philosophical discussions we had throughout the writing process. Your wisdom, encouragement, and the unique perspectives you both offered helped shape not only this work but also my intellectual growth. Thank you for always being there to challenge, inspire, and guide me through the most complex and uncertain moments of my work.

The work presented here would not have been possible without the contributions of all my co-authors. I feel incredibly fortunate to have had the opportunity of working alongside such remarkable scientists. I am deeply thankful to Taniya Chakraborty, Rakesh Chatterjee, Erik Poppleton, Yannik Dreher, Vasily Zaburdaev, Luca Monari, and Julius Fichtler whose input was pivotal to this work. The insights and inspiration you have provided will stay with me throughout my career and beyond.

When I joined the group, it was just a small team: Yannik Dreher, Kevin Jahnke, Tobias Walther, Tobias Abele, and Andreas Schoenit, during the challenging COVID period. However, I felt incredibly welcomed and supported by all of you from the very start. Toto and Tobi, thank you for being my long-lasting companions throughout this PhD journey. Being your peer has truly been one of the most exciting and rewarding experience. Kevin, thank you for paving the way in academia, setting an example I could learn from, and always being so generous with your advice and guidance. A special thank you to Yannik for your mentorship during the start of my time in the group. You have been not just a supervisor but a mentor, a big

brother, and a great friend. You have guided me with patience and care. I will always be grateful for your constant support and I hope I have made you proud.

I would also like to extend my heartfelt thanks to the junior scientists I have had the privilege to supervise. Witnessing your growth and supporting your development as independent scientists has been one of the most rewarding and fulfilling aspects of my academic journey. Thank you, Linus Frey and Manuel Bibrowski. Your curiosity, your tireless dedication, and unwavering commitment to excellence are nothing short of inspiring. You remind me, every day, why I am so passionate about science and mentorship. I eagerly look forward to seeing the great accomplishments that lie ahead for you.

This journey would not have been nearly as enjoyable without my amazing office mates from the Moffice: Maja Illig, Stefan Maurer, Michelle Emmert, Luca Monari, Erik Poppleton, and the extended member, William Verstraeten. The countless conversations we have had about work and life over the past four years, and the safe space you have all provided me, have been absolutely invaluable. Thanks to each of you, I have learned, grown, and become not only a better scientist but also a happier, more fulfilled person. I'm deeply grateful for your friendship and the joy you brought into my life every day.

I feel incredibly fortunate to be a part of the Biophysical Engineering Group. Vanessa Huth, Tim Karrasch, Julieth Bravo, Cody Geary, Fenja Murken, Claudia Helbig, Kornelia Mack, Franziska Giessler, Alena Taskina, and so many others have created such a positive and motivating work environment that I've genuinely looked forward to each day. You have made work both enjoyable and inspiring. Thank you for tolerating my quirky habits and humor, and for accepting me just as I am.

A significant portion of my PhD was carried out at the Max Planck Institute for Medical Research, and I would like to extend my gratitude to everyone there for fostering such a supportive atmosphere. A special thank you to the Spatz, Johnsson, and Hell groups for your unwavering generosity. Your expertise, time, and provision of essential equipment have been invaluable to this work.

I feel incredibly lucky to have made such wonderful friends along the way, especially Ana Yagüe, Andreas Fink, Anna Obraztsova, and Ngoc Anh Nguyen Ha. Your scientific work is inspiring, but it is your emotional support and kindness that have truly carried me through the most difficult moments. Having you by my side has been a gift, and I am deeply grateful for your friendship.

I would also like to thank all the sports crews and friend groups, both in and outside of Heidelberg. Being an international can be challenging, but your friendship, no matter our distance, has kept me company and supported throughout these years abroad. A special thanks to my friends in Heidelberg, who have made this place truly feel like a second home.

Speaking of home, I am so grateful to my family, my parents and my sister, for believing in me and supporting my decision to live 12-hour flight away to pursue my academic goals. You have given me the foundation to get here, and no matter where I am, you have always made sure I had a place to return to. Your constant encouragement and love inspire me every day to strive for excellence and do good in this world. All of this is as much your achievement as it is mine.

This acknowledgment is far from exhaustive. This work would not have been possible without the countless individuals I have met along the way during my studies. It is as much my result as it is the product of the collaborative efforts, generosity, and support of everyone who has been part of my journey. I also want to express my gratitude to the social systems of France and Germany, as well as the funding bodies that have provided the financial and institutional support crucial to my studies.

Lastly, thank you, my Julius. Meeting you and having you as my partner has truly been one of the best thing to come out of my PhD journey. You and your family have truly become my second family here. Thank you for being my partner, my co-author, my therapist, my friend, and for taking on so many roles to keep me grounded. Thank you for constantly reminding me how proud you are of me and how well I am doing. Your encouragement made all of this possible.